The effects of edge magnetic structure on particle fueling and exhaust in the HSX and W7-X stellarators

by

Laurie A. Stephey

A dissertation submitted in partial fulfillment of

the requirements for the degree of

Doctor of Philosophy

(Electrical Engineering)

at the

University of Wisconsin–Madison

2017

Date of final oral examination: October 17 2017

The dissertation is approved by the following members of the Final Oral Committee:
    David T. Anderson, Professor, Electrical Engineering
    Oliver Schmitz, Professor, Engineering Physics
    Simon Anderson, Scientist, Electrical Engineering
    Amy E. Wendt, Professor, Electrical Engineering
    Chris C. Hegna, Professor, Engineering Physics

ProQuest Number: 10639478

![ProQuest](ProQuest logo)

ProQuest 10639478

Abstract

In this study, both experimental and numerical techniques have been used to study particle behavior in response to changes in the edge magnetic field (i.e. inserting and removing edge islands) at the Helically Symmetric eXperiment (HSX) and Wendelstein-7X (W7-X) stellarators.

At HSX, the two magnetic configurations studied were the Edge-Islands and the No-Edge-Islands configurations. Measurements of the effective hydrogen particle confinement time, $\tau_{p,H}^*$, and the effective helium particle confinement time, $\tau_{p,He-II}^*$, were a factor of 1.5 and 1.6 longer, respectively, in the Edge-Islands configuration. A complete hydrogen particle balance yielded particle confinement times $\tau_{p,H}$ a factor of 1.3 longer in the Edge-Islands configuration. EMC3-EIRENE fueling efficiency calculations yielded values of 0.70 in the Edge-Islands configuration and 0.87 in the No-Edge-Islands configuration, a factor of 1.2 difference.

At W7-X, the two magnetic configurations studied were the Increased Iota and the Standard configurations. Measurements of $\tau_{p,He-I}^*$ and $\tau_{p,He-II}^*$ were a factor of 1.5 and 1.2 longer, respectively, in the Increased Iota configuration. A complete hydrogen particle balance yielded values of $\tau_{p,H}$ that were approximately the same in both configurations. Similarly, EMC3-EIRENE fueling efficiency calculations yielded values approximately the same in both configurations.

These results indicate that the edge magnetic structure can have a significant impact on the particle fueling and exhaust, but only if the change in edge structure is made in the ionization source region. In HSX, when the 8/7 island chain was inserted in the peak ionization source region in the Edge-Islands configuration, the 8/7 islands were able to decouple the plasma source from the confinement region through locally peaked temperatures at the island X-point (creating a private flux region in the same way that a divertor does). This led to reduced fueling efficiencies and increased global particle confinement times. For this same reason, moving the islands in W7-X did not result in major changes in particle fueling and exhaust, because the islands were not located in the ionization source region.

For my family

Acknowledgments

This thesis would never have been possible without the help and guidance of so many people. I am indebted and immensely grateful for all of their help.

Thank you to all members of my committee for your time, advice, and valuable feedback on the direction of this work.

I would like to thank my advisor David Anderson for his kindness, support, and incisive questions through the last few years. I would also like to thank him for agreeing to hire me, despite my knowing nothing about plasmas. Thank you so much for giving me the opportunity to work at HSX and learn as I went.

I would also like to thank Oliver Schmitz for taking a chance and sending me to Greifswald. Thank you for the opportunity to travel to a new place and participate in some truly exciting science. Thank you for your patience and your extremely helpful scientific guidance.

Thank you to all of my collaborators, who have provided helpful discussions, important simulations, hours in the lab for calibrations, and time to read and re-read all my papers and presentations and proposals. I am grateful for all your expertise and for sharing your valuable time to help me.

Thank you to all of the HSX scientists for their encouragement, fruitful discussions, and help in providing data and plots. I would like to thank Simon Anderson in particular for all of his help and patience in the HSX lab despite melting several screwdrivers and other mishaps.

Thank you to Aaron Bader for your frank feedback, your smart ideas, and your generosity with your time and your insight. Thank you for always being the first person to give me comments on anything I send to you, even with a broken wrist.

Thank you to all the HSX graduate students, past and present, with whom I have shared so many good memories. Sitting next to you all for these years has been a pleasure and an honor. I would also like to thank the HSX alumni for their help and insight, particularly Jeremy Lore.

me believe that I could be whatever I wanted to me, and working so hard to give me the ability to get here. Thank you also to my sister for your unending positivity and encouragement and for putting up with all the times you called me and got sent straight to voicemail because I was in the basement.

And thank you Brandon, for supporting me throughout our time together and letting me go halfway around the world for this project. Your patience, kindness, generosity, and deadpan wit are unmatched and I am immensely grateful for you.

Finally, I would like to thank the University of Wisconsin, the United States Department of Energy, and all other agencies who have helped to fund and support this work.

TABLE OF CONTENTS

Appendix

LIST OF FIGURES

Appendix
Figure   Page

Appendix
Figure

Appendix
Figure   Page

Appendix
Figure
Page

Appendix
Figure   Page

Chapter 1

Introduction

1.1 Motivation

As the population of earth continues to increase, so does our collective need for energy. Most of our current energy production relies heavily on fossil fuels, which though they are relatively plentiful and inexpensive, release large quantities of carbon dioxide into the atmosphere when they are burned. As of this writing, we have already surpassed the critical level of 350 ppm of CO_2 in our atmosphere [1]. At 400 ppm and rising, we must work quickly to reduce our carbon emissions or face unprecedented and possibly catastrophic changes in our climate.

Though many believe the solution lies completely in renewable, carbon-neutral energy technogolies like solar and wind, renewable energy unfortunately cannot provide all the energy we require (11% today, projected to be 15% in 2040 in the United States) [2]. Therefore, we need several energy technologies to combine their respective strengths to combat this dangerous rise in carbon emissions.

Traditional nuclear power (fission) is currently a good energy option since it can safely produce hundreds of megawatts with zero carbon emissions. Reactor design has come a long way and newer, safer, and more efficient reactor types are possible today [3]. Fission power does however generate worries about nuclear proliferation, has resulted in serious accidents like Chernobyl and Fukushima, and raises difficult issues in the long-term disposal of spent fuel. Despite these

potential risks, reducing atmospheric carbon is of the utmost importance at this time. Until other carbon-free energy sources can substantially increase their generating capacity, fission is currently the best option for large-scale energy generation.

Once developed, fusion energy will offer several advantages over traditional fission power. With no prospects of "meltdown", reduced issues of proliferation and long-term waste complications, fusion power can provide clean, safe, carbon-free energy. In addition to power generation, fusion may also offer important capabilities for space travel and planetary defense [4]. In the quest for fusion, pushing the boundaries of current science, engineering, and material limits will most certainly provide valuable innovations, much like those developed as a result of the space program [5].

Before commercial fusion power can become a reality, however, several key issues must be solved. One of these issues is how to maintain desirable core plasma parameters (n_e, T_e, and T_i) while also staying within acceptable heat and particle load limits to prevent melting and erosion, respectively. In the infancy of fusion research, it was hoped the plasma edge would "take care of itself" [6], which has unfortunately not been the case. Since that time, there has been a considerable research effort into techniques that can both maintain desirable core plasma parameters, and also permit heat and impurities to be safely removed from the plasma. This removal is necessary to permit steady-state operation, an essential requirement for a fusion power plant.

Currently, the most promising implementation of a fusion reactor is through magnetic confinement of the hot plasma, and one such type of configuration is a stellarator (described in more detail in Sections 1.3 and 1.4). In this work, we seek to contribute to the understanding of how the edge magnetic structure of stellarators can be used to influence particle fueling and exhaust physics. The intention of this work is to provide insight into how magnetic islands can improve main ion particle confinement and reduce edge recycling contributions. This work has implications for the

Wendelstein 7-X (W7-X) island divertor in particular, which is as of this writing, just beginning its first divertor test phase (OP 1.2(a)).

1.2 Main physics questions in this work

The primary physics questions (and results) in this work pertain to stellarator magnetic islands and their relationship with the main plasma ionization region (or ionization domain) in the edge. Therefore some background and explanation of these concepts is required. This information will be provided in the subsections that follow.

1.2.1 A brief overview of edge physics and terminology

We must first outline some important edge physics concepts, as well as define some terminology. We will define the scrape off layer (SOL) as the region of open field lines that intersect the wall or a target. The connection length is typically defined as the target-to-target distance along a field line; where $2L_c$ is the distance along the field line between two points of contact with a surface, as described by Section 1.4.1 in [6].

We will define the edge as the region between the LCFS (last closed flux surface) and the wall. The edge therefore contains the SOL and can have both open and closed field lines (i.e. islands). For closed field lines, transport is diffusive (as described by Fick's law $\vec{J} = -D\nabla\phi$, where J is the diffusive flux, D is the diffusion coefficient, and $\nabla\phi$ is the gradient of the concentration of some substance [7]). For long field lines, transport is some combination of both parallel and diffusive transport. For short field lines, transport is expected to be predominantly parallel.

In a diverted tokamak, the edge and the SOL are the same since all edge field lines connect to the target. In a stellarator, however, the SOL falls within the edge, but does not necessarily comprise the whole edge. Stellarators naturally have islands, which are closed field line flux bundles, which result from a rational number in the rotational transform. For the quasi-helical symmetry
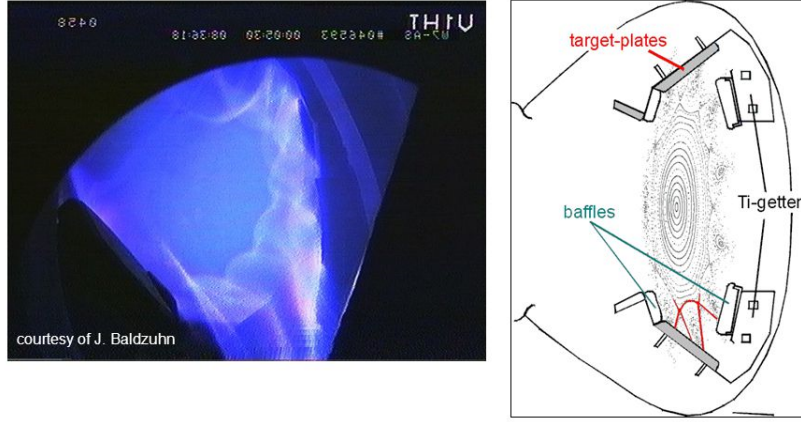
Figure 1.1 Figure showing the W7-AS island divertor, the predecessor experiment to W7-X. On the left, visible emission in the plasma cross section is shown. On the right, the ideal edge magnetic topology of the island divertor is shown. By comparision, it can be seen that the divertor structure results increased line-emission outside the LCFS, indicating that the divertor may have reduced the ability of particles to penetrate into the confinement region. Figure reproduced from [8] presentation slide.

(QHS) configuration in the Helically Symmetric eXperiment (HSX), the natural 8/7 island chain outside the LCFS results in a region of closed field lines, a region of open field lines, and a transition region of long to short connection lengths. These varied connection lengths result in regions where both parallel and perpendicular transport must be considered.

1.2.2 The relationship between the ionization domain and the density profile

The ionization domain is the region in which the neutral particles sourced from the limiter, the wall, the divertor, or the gas injection system, are ionized. For regions in which the diffusive transport dominates (notably within the LCFS), it is useful to use the ionization length as a metric. We define the ionization length, λ_{iz}, as:

$$\lambda_{iz} = \frac{v_n}{n_e \langle \sigma_I v_e \rangle} \tag{1.1}$$
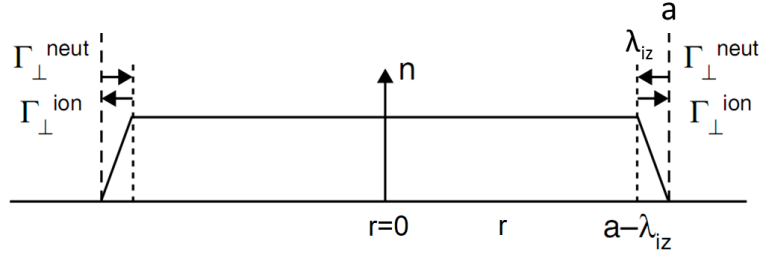
Figure 1.2 A representation of the density profile and how it is directly affected by the plasma source. Reproduced with some additions from [6].

where v_n is the thermal velocity of the neutral, n_e is the electron density, and $\langle \sigma_I v_e \rangle$ is the rate coefficient for electron impact ionization, the dominant ionization process in the plasmas considered in this work (Equation 4.55 in [6]).

In general, it is preferable that these (main ion) neutral particles are ionized outside, rather than inside, the confinement region, and diffuse inward to fuel the plasma. Inside the confinement region, neutrals can provide a momentum sink that can slow the plasma rotation [9]. Additionally, there is a direct relationship between the plasma density profile and the ionization domain. Fig. 1.2 demonstrates that in the ionization region (the region bounded by dotted lines), the density profile decreases as the ionization source rate increases. This phenomena will be explained in greater detail below.

We will now use a 1-D example to illustrate the relationships shown in Fig. 1.2. We assume that the plasma is quasineutral (i.e. the density of positive and negative particles is approximately equal over the plasma volume [10]), that all quantities are in steady-state, and that $Z = 1$ (i.e. this example applies only to hydrogenic species). At $r \ll a - \lambda_{iz}$, all particles have been ionized and there is no significant source or sink in this region [6]. (The inner edge of the ionization region is at $r = a - \lambda_{iz}$.) In the source region, $a - \lambda_{iz} < r < a$, where a is the radial location of the LCFS, we find that:

$$\Gamma_\perp^{ion} = -\Gamma_\perp^{neutral} = -D_\perp \nabla n_e \tag{1.2}$$

where $\Gamma_\perp^{ion}$ is the radial ion flux in particles/m^2/s, $\Gamma_\perp^{neutral}$ is the radial neutral particle flux in the same units, $D_\perp$ is the particle diffusivity in m^2/s, and ∇n_e is the radial density gradient (Equation 4.46 in [6]).

We define the radial density gradient in the ionization domain in terms of the core density, $n(0)$, and the ionization length:

$$\nabla n_e = \frac{n(0)}{\lambda_{iz}} \tag{1.3}$$

If we substitute this expression for the density gradient into Equation 1.2, we find that the density in the core is given by:

$$n(r < a - \lambda_{iz}) = n(0) = -\frac{\lambda_{ion}\Gamma_\perp^{neutral}}{D_\perp} \tag{1.4}$$

The density in the core is constant as expected since there are no sources or sinks in this region. In the plasma source region, the density profile depends on the ionization length:

$$n(a - \lambda_{iz} < r < a) = \frac{n(0)a(1 - r/a)}{\lambda_{iz}} \tag{1.5}$$

and decreases linearly from $n(0)$ at $r = a - \lambda_{iz}$ to 0 at $r = a$ (the so-called hard boundary condition [6]), as pictured in Fig. 1.2 (Equation 4.50 in [6]). Thus, the plasma source and the edge density profile are directly related as a consequence of $n(a) = 0, n(a - \lambda_{iz} = n(0))$.

1.2.3   Controlling the ionization domain through limiters and divertors

The ionization domain can have a direct effect on the plasma density profile and other global confinement properties. Therefore a careful way to manage the neutral population is required. In both stellarators and tokamaks, one of two structures is typically used to attempt to control neutral and impurity influx to the plasma: the limiter and the divertor [6].

Limiters, shown in Fig. 1.3, are structures which are inserted into the edge of the plasma to intercept field lines and reduce the plasma-wetted area to a controlled size and location. However, since limiters define the LCFS, it is difficult to prevent recycling neutrals and sputtered impurities
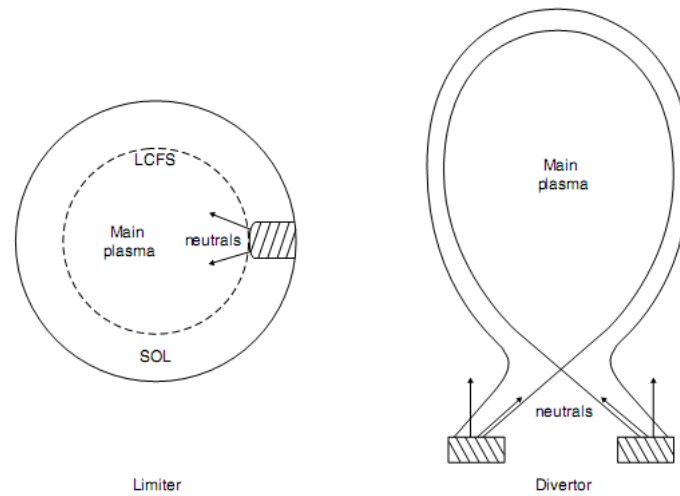
Figure 1.3 A depiction of a limiter (L) and a divertor (R) reproduced directly from [6]. Note that the divertor configuration allows the recycling neutrals to be isolated from the confined plasma.

from directly entering the plasma [6]. Limiter pumping can be used to reduce, but not eliminate, this particle influx [11]. Furthermore, in high performance plasmas, heat loads can exceed material limits and may result in erosion, melting, or both.

Divertors, shown in Fig. 1.3, attempt to move the neutral and impurity source away from the confinement region. In a diverted tokamak, a null in the magnetic field (an X-point) is created, with additional coils, that separates the core plasma from the edge. Divertor plates intercept the field lines between LCFS and the wall, thereby providing a controlled plasma sink [6]. The magnetic geometry can be such that the flux is expanded before hitting the divertor plates, helping to spread the heat and particle loads to acceptable levels. Divertor operation has been key to achieving high-performance plasmas in the major tokamak experiments, notably ASDEX, the first tokamak to access the H-mode regime [12].

In stellarators, the concept of a divertor is still a topic of active research. Stellarators can have a topology change between the confined flux surfaces and open flux surfaces. The open surfaces can include well-formed magnetic islands at low order resonances, or can contain multiple resonances that combine to produce a stochastic region. Several approaches have been developed to exploit
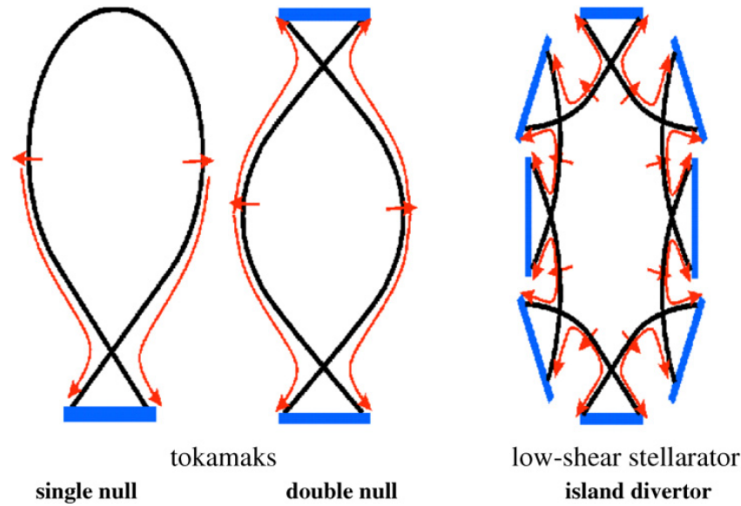
Figure 1.4 Cartoon demonstrating the similarities and differences between (left) a single-null tokamak divertor, (center) a double-null tokamak divertor, and (right) a stellarator island divertor. Figure reproduced from [14].

these properties, including the island divertor [13] which makes use of the X-points created by the careful placement of edge islands through tuning both the iota profile and the magnetic shear. In Fig. 1.4, three types of divertors are pictured. On the left a single null tokamak divertor is shown. In the middle, a double null tokamak divertor is shown. On the right, a stellarator island divertor is shown. In this figure, the similarities between the tokamak divertor and the island divertor are clear. Rather than using external coils to create nulls in the poloidal field, the rotational transform profile is manipulated so that an edge island chain exists between the LCFS and divertor targets designed to intercept the islands. The control of magnetic islands will be discussed in the next section.

1.2.4 Controlling the ionization domain through edge magnetic topology

The edge magnetic structure affects particle fueling and exhaust and has an important impact on the impurity handling in both tokamaks as well as stellarators[15, 16]. Stellarators (and tokamaks) have magnetic islands when the iota profile, $\iota(r)$, crosses rational values. At these rational values,

the plasma field lines form magnetic island structures because of a harmonic perturbation of the field lines by resonant components in the confining magnetic field [17]. The radial position of these islands can be adjusted by raising or lowering the iota profile, through variations in the magnetic shear, or by introduction of resonant magnetic perturbations (RMPs). In the stellarator edge, however, these islands can be embedded into a chaotic magnetic field structure consisting of regions of long, short, and infinite connection length.

Magnetic islands have been shown to impact the plasma temperature, density, local plasma flow and radial electric field at LHD [18, 19, 20]. LHD measured a flattening of the temperature profile, density peaking within the island, and sheared poloidal flows and radial electric fields at the island boundary. Measurements at HSX have also indicated density and plasma potential peaking in the 8/7 edge island [21]. Additionally, the magnetic island position relative to the ionization region (in which the neutral density profile decays) and the recycling region (in which the neutral profile increases) has been shown to affect helium exhaust and confinement in TEXTOR and LHD [22, 23, 24]. These experiments showed that magnetic islands in the plasma edge led to reduced helium fueling efficiency and also a reduction in the effective helium confinement time in TEXTOR and LHD. It is important to note, however, that these islands were located radially inside the boundary of plasma source region (i.e. not in the $S_p(r)$ region), or in terms of Fig. 1.2, in the $r < a - \lambda_{iz}$ region. In these experiments, the impact of the islands on the radial transport and parallel transport balance for impurities, specifically the balance between the friction and thermal force, affects the inward fueling and outward transport ratio [22, 23].

1.3   The HSX Stellarator

Half of this work was performed at the Helically Symmetric eXperiment (HSX) [25], which is the world's first stellarator optimized to reduce neoclassical transport [26]. HSX has 48 modular coils that are used to magnetically confine plasma without an internal plasma current. These highly
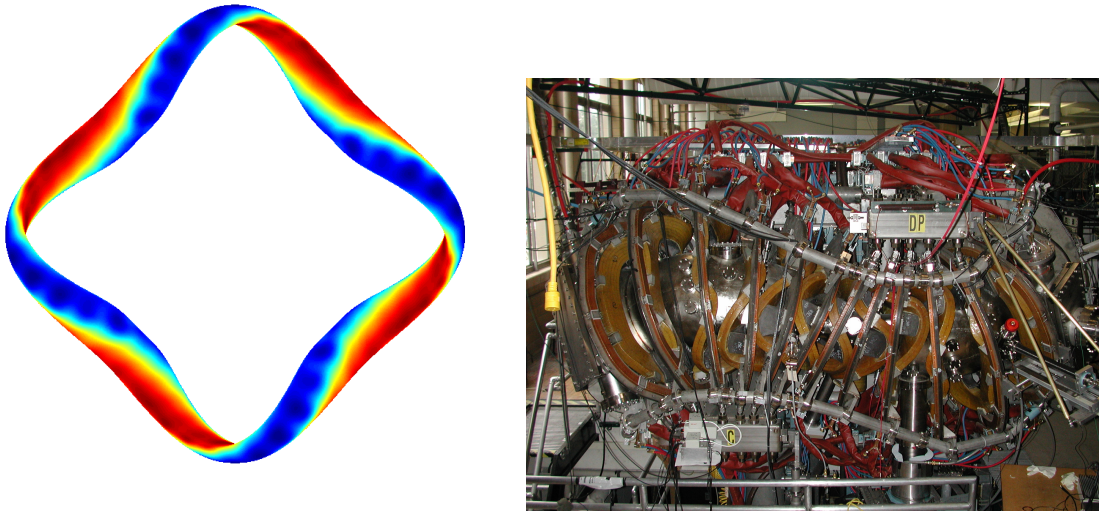
Figure 1.5 (L) The mod-B contours on a flux surface of the QHS magnetic field configuration of HSX and (R) a photo of one field period of the HSX experiment.

shaped coils can be clearly seen in Fig. 1.5. Typical HSX parameters are summarized in Table 1.1. Measurements that provided these results were the HSX interferometer and Thomson scattering systems, edge Langmuir probe measurements [27], and ion doppler spectroscopy [28, 29].

HSX has substantial flexibility in magnetic configurations. In its optimized configuration known as QHS (quasi-helical symmetry), there is a symmetry in the direction of mod-B and in the particle frame of reference, the HSX field appears similar to a tokamak with an increased effective transform. The increased effective transform keeps the particles more closely confined to field lines and therefore reduces drift orbit losses [26].

Table 1.1 HSX Parameters

Parameter	Core	Edge
n_e	4E12 cm^{-3}	1E11 cm^{-3}
T_e	2.5 keV	70 eV
T_i	60 eV	25 eV

1.4 The W7-X Stellarator

The other half of this work was performed at the Wendelstein 7-X (W7-X) stellarator in Greifswald, Germany [30]. It is the world's largest optimized stellarator and will help explore whether optimized stellarators are good candidates for a commercial reactor, as well as study the viability of the island divertor concept. W7-X is a superconducting experiment designed for long-pulse, high power, high density operation.

These experiments were performed during the first operation phase at W7-X called OP 1.1 (2015-2016). In this phase, one stellarator symmetric graphite limiter was mounted on the inboard side of each of the five field periods. Using up to 4 MW of ECRH launched power, plasmas with up to 10 keV core T_e could be obtained with energy confinement times $\sim$ 150 ms [31]. At 1 MW of launched power, steady plasmas of up to 6 s were obtained. The general experimental parameters of this first operational phase are summarized in Table 1.2.

Table 1.2 W7-X Parameters

Parameter	Core	Edge
n_e	4E13 cm^{-3}	1E12 cm^{-3}
T_e	10 keV	40 eV
T_i	1 keV	no data

1.5 Overview of this work

In this work, we assess the impact of the position of magnetic islands at the plasma boundary on plasma fueling and exhaust. The experiments at HSX serve as a foundation for the link between island position and size and the subsequent impact on the particle balance. This is because at
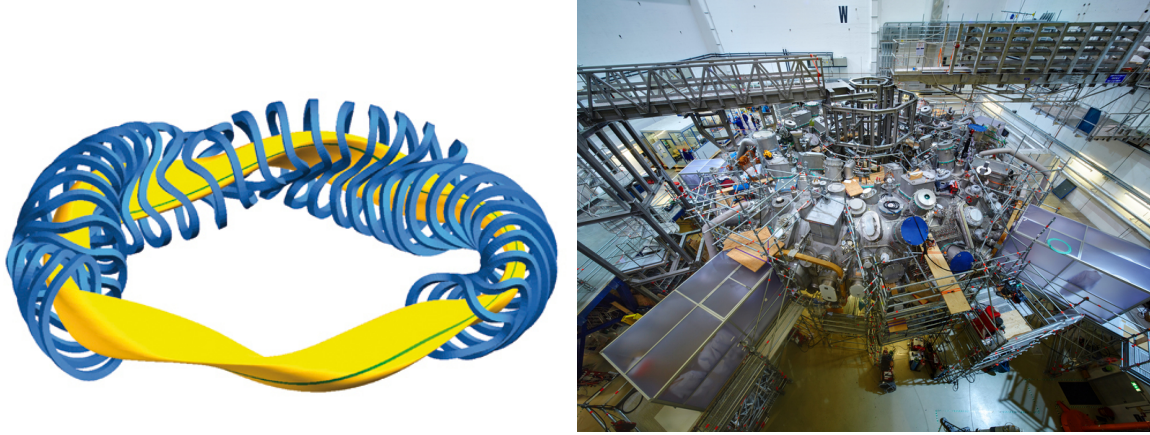
Figure 1.6 (L) A CAD representation of the five-field period W7-X stellarator. (R) An image of W7-X in Greifswald, Germany [32].

HSX, experiments were possible in which island position relative to the plasma source region was changed.

To categorize the magnetic configurations explored at both HSX and W7-X, we use the location of the magnetic island relative to the main plasma source location. Here, we consider the plasma particle source profile $S_p(r)$ which typically peaks near the LCFS. Typical edge and core plasma parameters for HSX and W7-X are summarized in Tables 1.1 and 1.2, respectively. Due to lower plasma densities, HSX has a more gradual falloff of the neutral source towards the plasma center as compared to W7-X (i.e. a larger value of λ_{iz}). Despite this, the dominant plasma particle source is located near the LCFS. (This qualitative discussion about $S_p(r)$ is based on modeling results with the fully 3-D plasma edge fluid transport and kinetic neutral gas transport code EMC3-EIRENE, which will be discussed in Chapter 3.) Hence, the location of the island with respect to the peaked region of $S_p(r)$ is used as a means to categorize the magnetic configurations examined in this work.

It should be noted that the shape and location of $S_p(r)$ in the stellarator edge is **not** static with respect to the magnetic configuration. The experiments performed in this work were not simply a matter of inserting islands into and removing islands from this source region. Rather, as will
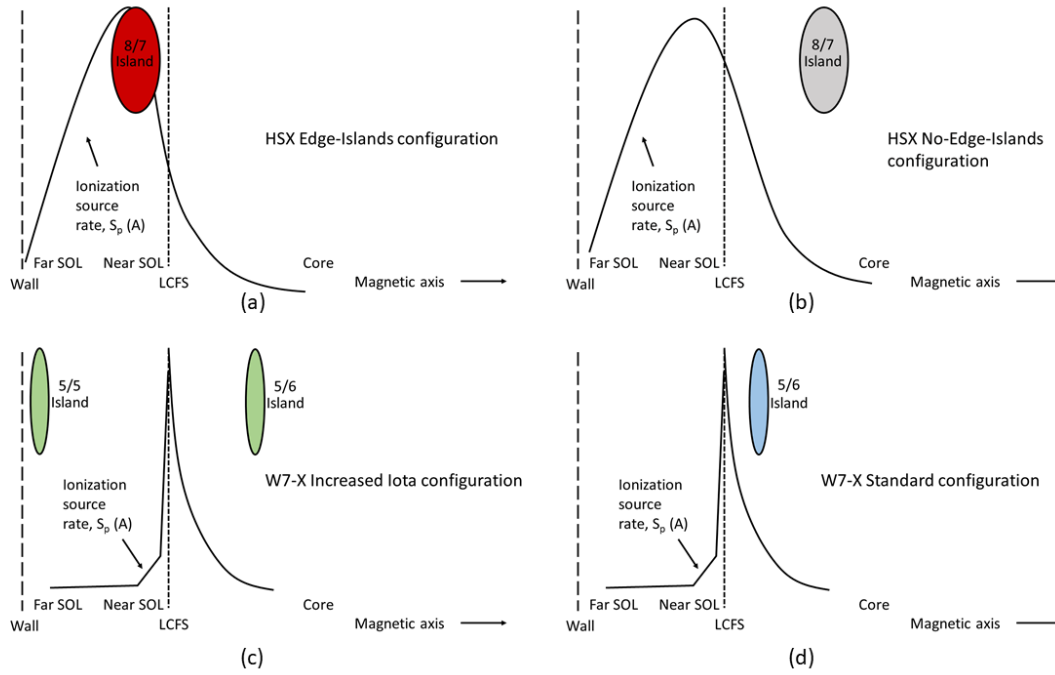
Figure 1.7 Cartoon illustrating four possible scenarios of the island position relative to the ionization domain. Scenario (a) illustrates the HSX Edge-Islands configuration, scenario (b) illustrates the HSX No-Edge-Islands configuration, scenario (c) illustrates the W7-X Increased Iota configuration, and scenario (d) illustrates the W7-X Standard configuration.

be discussed in Chapters 4 and 6, the presence of the island can alter the $S_p(r)$ distribution in a self-consistent manner, and therefore must be treated in a self-consistent manner.

Fig. 1.7 illustrates cartoons of four possible scenarios of the island position relative to the ioniz-ation domain that were investigated in this work at either HSX or W7-X. In this figure, scenario (a) illustrates the HSX Edge-Islands configuration, scenario (b) illustrates the HSX No-Edge-Islands configuration, scenario (c) illustrates the W7-X Increased Iota configuration, and scenario (d) il-lustrates the W7-X Standard configuration. The particular details of each configuration will be described in more detail below, and additionally in Chapters 4 and 5. It should again be stressed that these are only cartoons and should not suggest that the ionization domain is static.

Two different magnetic configurations were examined in each device: one in which the magnetic island was located in the increasing section of $S_p(r)$ (outside the LCFS), and one in which the island was moved inward to be located in the decreasing section of $S_p(r)$ (inside the LCFS). At HSX, this manipulation of the island position inwards did change the $S_p(r)$ profile itself, but the resulting changes were small enough that the 8/7 island chain was able to be shifted from one side of the source profile to the other.

At W7-X, however, the change of $\iota(r)$ was only able to move the $m/n = 5/5$ island chain from outside the vessel into the scrape-off layer, while at the same time moving the $m/n = 5/6$ island chain from 1-2 cm inside the LCFS to 10 cm inside the LCFS. This restriction was due to commissioning and engineering constraints. Thus in neither configuration could the island be placed in the peak $S_p(r)$ region, and therefore a less pronounced effect might be expected. It should also be noted, that in each of these configuration pairs, an effort was made to preserve the general and core transport properties by keeping the plasma volume, density, temperature (and neoclassical transport, through the effective ripple, ϵ_{eff}, as close as possible). As a result we expect that any changes we observe in the particle penetration and confinement properties should stem primarily from the edge magnetic topology changes.

The rest of this thesis will be structured as follows. In Chapter 2, the experimental diagnostics and methods used at both HSX and W7-X will be described. In Chapter 3, the numerical tools used in this work, the EMC3-EIRENE coupled codes and the DEGAS code, will be described and their applications to this work will be outlined. In Chapter 4, the experimental and numerical results for HSX will be discussed. In Chapter 5, the experimental and numerical results for W7-X will be discussed in a similar structure to Chapter 4. Finally in Chapter 6, the results from both HSX and W7-X will be discussed and the important physics results will be highlighted and summarized. Ideas for future work are listed at the end of Chapter 6.

References

1. Hansen, J., Mki. Sato, P., Kharecha, D. *et al.* NASA Science Briefs, Target Atmospheric CO2: Where should humanity aim? [Online]. `http://www.giss.nasa.gov/research/briefs/hansen_13/` (May 2015).

2. U.S. Energy Information Administration. FAQ: How much of world energy consumption and electricity generation is from renewable energy? [Online]. `http://www.eia.gov/tools/faqs/faq.cfm?id=527&t=1` (May 2015).

3. Butler, D. Energy: Nuclear power's new dawn. *Nature* **429,** 238–240. ISSN: 0028-0836 (2004).

4. Wurden, G., Weber, T., Turchi, P., Parks, P., Evans, T., Cohen, S., Cassibry, J. & Campbell, E. A new vision for fusion energy research: fusion rocket engines for planetary defense. *Journal of Fusion Energy* **35,** 123–133. ISSN: 0164-0313 (2016).

5. Thumm, T. L., Robinson, J. A., Buckley, N., Johnson-Green, P., Kamigaichi, S., Karabadzhak, G., Nakamura, T., Sabbagh, J., Sorokin, I. & Zell, M. International Space Station Benefits for Humanity (2012).

6. Stangeby, P. C. *The plasma boundary of magnetic fusion devices* 717 pp. ISBN: 978-0-7503-0559-4 (Institute of Physics Pub, Bristol ; Philadelphia, 2000).

7. Crank, J. *The mathematics of diffusion* ISBN: 0-19-853411-6 (Oxford university press, 1979).

8. Wolf, R. *Wendelstein 7-X: Scientific Objectives* 2015. `http://images.slideplayer.com/15/4765326/slides/slide_29.jpg` (2017).

9. Winter, J. Wall conditioning in fusion devices and its influence on plasma performance. *Plasma Physics and Controlled Fusion* **38,** 1503. ISSN: 0741-3335 (1996).

10. Chen, F. F. *Introduction to plasma physics* ISBN: 1-4757-0459-3 (Springer Science & Business Media, 2012).

11. Mioduszewski, P. Experimental studies on pump limiters. *Journal of Nuclear Materials* **111,** 253–267. ISSN: 0022-3115 (1982).

12. Wagner, F., Becker, G., Behringer, K., Campbell, D., Eberhagen, A., Engelhardt, W., Fussmann, G., Gehre, O., Gernhardt, J., Gierke, G. v. *et al.* Regime of improved confinement and high beta in neutral-beam-heated divertor discharges of the ASDEX tokamak. *Physical Review Letters* **49,** 1408 (1982).

13. Grigull, P., McCormick, K., Baldzuhn, J., Burhenn, R., Brakel, R., Ehmler, H., Feng, Y., Gadelmeier, F., Giannone, L., Hartmann, D. *et al.* First island divertor experiments on the W7-AS stellarator. *Plasma physics and controlled fusion* **43,** A175 (2001).

14. Feng, Y., Kobayashi, M., Lunt, T. & Reiter, D. Comparison between stellarator and tokamak divertor transport. *Plasma physics and controlled fusion* **53,** 024009. ISSN: 0741-3335 (2011).

15. Feng, Y., Sardei, F., Grigull, P., McCormick, K., Kisslinger, J. & Reiter, D. Physics of island divertors as highlighted by the example of W7-AS. *Nuclear Fusion* **46,** 807–819. ISSN: 0029-5515, 1741-4326 (2006).

16. Sardei, F., Feng, Y., Grigull, P., Herre, G., Hildebrandt, D., Hofmann, J., Kisslinger, J., Brakel, R., Das, J. & Geiger, J. Island divertor studies on W7-AS. *Journal of nuclear materials* **241,** 135–148. ISSN: 0022-3115 (1997).

17. Hudson, S., Monticello, D. & Reiman, A. Reduction of islands in full-pressure stellarator equilibria. *Physics of Plasmas* **8,** 3377–3381. ISSN: 1070-664X (2001).

18. Ida, K., Ohyabu, N., Morisaki, T., Nagayama, Y., Inagaki, S., Itoh, K., Liang, Y., Narihara, K., Kostrioukov, A. Y. & Peterson, B. Observation of Plasma Flow at the Magnetic Island in the Large Helical Device. *Physical review letters* **88,** 015002 (2001).

19. Ida, K., Inagaki, S., Tamura, N., Morisaki, T., Ohyabu, N., Khlopenkov, K., Sudo, S., Watanabe, K., Yokoyama, M. & Shimozuma, T. Radial electric field and transport near the rational surface and the magnetic island in LHD. *Nuclear fusion* **44,** 290. ISSN: 0029-5515 (2004).

20. Ida, K., Inagaki, S., Yoshinuma, M., Tamura, N., Morisaki, T. & LHD Experiment Group. Potential Structure and Transport in the Magnetic Island in LHD. *Fusion Science and Technology* **58,** 113–121 (2010).

21. Akerson, A. R., Bader, A., Hegna, C. C., Schmitz, O., Stephey, L. A., Anderson, D. T., Anderson, F. S. B. & Likin, K. M. Three-dimensional scrape off layer transport in the helically symmetric experiment HSX. *Plasma Physics and Controlled Fusion* **58,** 084002. ISSN: 0741-3335, 1361-6587 (1st Aug. 2016).

22. Schmitz, O., Ida, K., Kobayashi, M., Bader, A., Brezinsek, S., Evans, T., Funaba, H., Goto, M., Mitarai, O. & Morisaki, T. Enhancement of helium exhaust by resonant magnetic perturbation fields at LHD and TEXTOR. *Nuclear Fusion* **56,** 106011. ISSN: 0029-5515 (2016).

23. Bader, A., Kobayashi, M., Schmitz, O., Akerson, A., Effenberg, F., Frerichs, H., Feng, Y., Hegna, C., Ida, K. & LHD Experimental Group. Modeling of helium transport and exhaust in the LHD edge. *Plasma Physics and Controlled Fusion* **58,** 124006. ISSN: 0741-3335 (2016).

24. Ida, K., Yoshinuma, M., Goto, M., Schmitz, O., Dai, S., Bader, A., Kobayashi, M., Kawamura, G., Moon, C. & Nakamura, Y. Helium transport in the core and stochastic edge layer in LHD. *Plasma Physics and Controlled Fusion* **58,** 74010–74016. ISSN: 0741-3335 (2016).

25. Anderson, D., Almagri, A., Anderson, F., Matthews, P., Shohet, J. & Talmadge, J. HSX: A Project Overview and Current Status. *Bull. Am. Phys. Soc* **39,** 1601 (1994).

26. Canik, J. M., Anderson, D. T., Anderson, F. S. B., Clark, C., Likin, K. M., Talmadge, J. N. & Zhai, K. Reduced particle and heat transport with quasisymmetry in the Helically Symmetric Experiment. *Physics of Plasmas* **14,** 056107. ISSN: 1070664X (2007).

27. Akerson, A. R. *Identification of the helical scrape-off layer structure and transport properties in the edge of HSX* ISBN: 1-369-05191-3 (The University of Wisconsin-Madison, 2016).

28. Gerhardt, S. P. *Measurements and modeling of the plasma response to electrode biasing in the hsx stellarator* PhD thesis (Univeristy of Wisconsin - Madison, 2004).

29. Briesemeister, A. R. *Measurement and modeling of the flows and radial electric field in the HSX stellarator* bibtex: Briesemeister. PhD thesis (University of Wisconsin-Madison, 2013).

30. Grieger, G. & Milch, I. Das Fusionsexperiment WENDELSTEIN 7-X. *Physikalische Blätter* **49,** 1001–1005. ISSN: 1521-3722 (1993).

31. Wolf, R. C., Beidler, C., Beurskens, M., Biedermann, C., Bosch, H.-S., Bozhenkov, S., Brakel, R., Dinklage, A., Feng, Y. & Fuchert, G. Major results from the first plasma campaign of the Wendelstein 7-X stellarator. *Nuclear Fusion.* ISSN: 1741-4326 (2017).

32. Max-Planck-Institut fur Plasmaphysik. W7-X: Concept planning [Online]. `https://www.ipp.mpg.de/2815232/konzeptentwicklung` (May 2015).

Chapter 2

Measurement and analysis approach on both devices

2.1 Introduction

In this chapter we provide a brief overview of the analysis methods of measurements used to assess changes in particle fueling and confinement at HSX and W7-X as a result of changing the edge magnetic structure. We will first describe the two main types of measurements used: the effective particle confinement time τ_p^* and the actual global particle confinement time τ_p, based on a single reservoir particle balance. We will then provide a more detailed overview of the principal diagnostics and measurements used in this work at both HSX and W7-X.

2.2 Effective particle confinement time

The effective particle confinement time τ_p^* is the decay time of some particle-confinement related quantity, usually plasma density or spectroscopic emission. For the situation where the majority of the plasma source comes from recycling (i.e. wall or limiter recycling), the effective particle confinement time is connected to the global confinement time τ_p of a reservoir by the recycling coefficient R:

$$\tau_p^* = \frac{\tau_p}{1 - R} \tag{2.1}$$

τ_p^* is usually determined by fitting the decay of the plasma density following a perturbative gas injection. This gas injection provides a transient particle source to the plasma and after it ceases, the decay of the density spike from this gas injection can be measured. For the case of perturbative
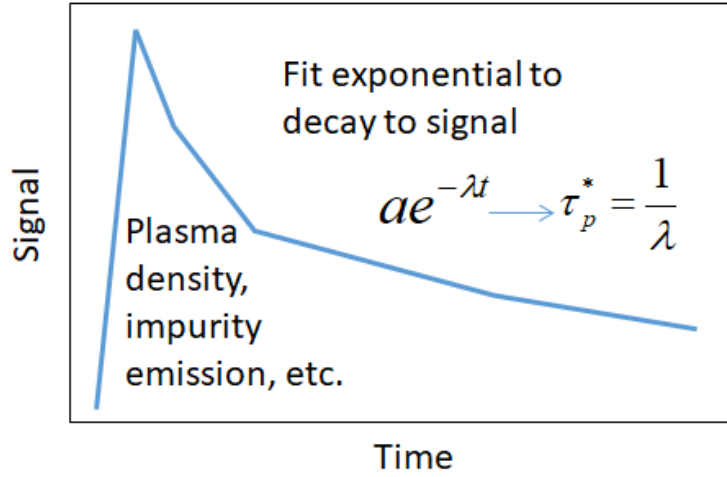
Figure 2.1 Cartoon illustrating the process used to determine the effective particle confinement time from measurement data. Usually following some type of perturbative gas injection, the decaying plasma density or the line-integrated emission as a function of time are fit to an exponential function. The coefficient of the fit is used to determine τ_p^*.

gas injection experiments with He, it is assumed that the emission of the He-II line at λ=468.6 nm is representative, to first order, of the singly ionized helium density and He-I emission at λ_1=667.8 nm or λ_2=587.4 nm are representative, again to first order, for the helium neutral density. Measuring τ_p^* by such perturbative gas injections is a commonly used technique [33, 34, 22] to infer effective confinement properties of the measured species.

2.3 Global particle confinement time

In order to establish a balance between the total number of particles N_{tot} and its time rate of change, dN_{tot}/dt, in the plasma reservoir due to particle fueling rates and particle exhaust quantities, a single reservoir particle balance method is used. To construct this balance, the plasma is treated as the reservoir, and all particles inside, entering, and exiting the reservoir must be quantified. Such 0-D single reservoir models are commonly used [35, 36, 37]. Below is the
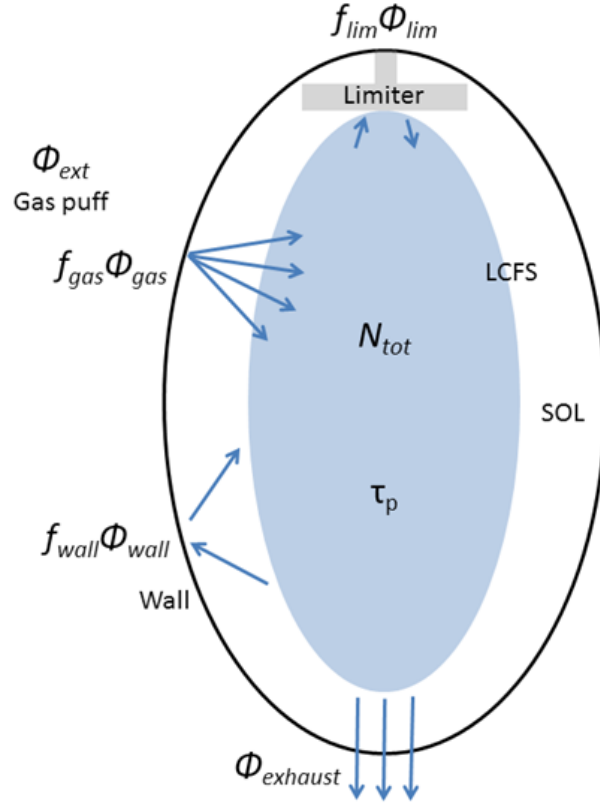
Figure 2.2 Cartoon illustrating the single reservoir particle balance analysis method. To perform this balance, all particles inside, entering, and exiting the reservoir must be accounted for. This allows the system dwell time, or the particle confinement time, to be determined.

formulation of this 0-D balance employed in this study:

$$\frac{dN_{\text{tot}}}{dt} =$$

$$-\frac{N_{\text{tot}}}{\tau_p} + f_{\text{gas}}\Phi_{\text{gas}} + f_{\text{wall}}\Phi_{\text{wall}} + f_{\text{lim}}\Phi_{\text{lim}} = \tag{2.2}$$

$$\Phi_{\text{ext}} - \Phi_{\text{exhaust}}$$

where N_{tot} is the total number of plasma particles, τ_p is the particle confinement time, f_{gas}, f_{wall}, and f_{lim} are fueling efficiency coefficients, and Φ_{gas}, Φ_{wall}, Φ_{lim} are particle fluxes from the gas valve, recycling from the main wall, recycling from the limiter and Φ_{ext} is the total external fueling, and Φ_{exhaust} is the exhaust rate. This will yield τ_p as a characteristic global dwell time as the solution to

this 1st order differential equation in the time domain. This characteristic time scale is treated as the global particle confinement time τ_p inside of the reservoir.

This balance includes information about fueling efficiencies (the f coefficients) for a given particle source/sink condition and plasma regime. The fueling efficiency is defined as the fraction of total ionizations that occur within the confinement region:

$$f_{\text{eff}} = \frac{S_{\text{p,conf}}}{S_{\text{p,conf}} + S_{\text{p,SOL}}} \tag{2.3}$$

where f_{eff} is the fueling efficiency coefficient, $S_{\text{p,conf}}$ is the ionization source rate inside the confinement region, and $S_{\text{p,conf}}$ is the ionization source rate outside the confinement region (i.e. in the SOL). In particular, the fueling efficiency depends on the ionization scale length λ_{iz} (see Equation 1.1), which is a function of the background plasma temperature and density. These fueling efficiencies are obtained from EMC3-EIRENE modeling and will be discussed in more detail in Chapter 3.

Additionally, the particle balance relies on the accurate measurement of the recycling flux terms from wall and limiter surfaces. However, due to the 3-D shape of the vessel wall and the fact that the entire surface area of the wall could not be observed with suitable cameras or other diagnostics, extrapolations of local measurements are required to obtain these major source terms in the particle balance. This is an issue for the absolute accuracy of the extracted values of τ_p. However, if the general wall and limiter flux structure does not change substantially between configurations, this uncertainty can instead be treated as a systematic uncertainty which will in turn cancel out when performing relative comparisons between two configurations. Thus the uncertainty in relative changes $\Delta\tau_p$ between configurations will have a lower value, defined only by the individual uncertainty in the measurements, which will be discussed in more detail in Chapters 4 and 5.

Clearly this analysis requires a great deal more information than the τ_p^* measurement. A particle balance will yield τ_p which is the true confinement time and does not suffer from the recycling coefficient-related ambiguity inherent in the τ_p^* measurements. In this way the particle balance is an extremely powerful method to study plasma particle confinement.

In the subsections that follow, an overview of how each of the terms in the particle balance was determined at HSX and W7-X will be given. More detailed information pertaining to the specific methods used at each experiment can be found in Chapters 4 and 5 for HSX and W7-X, respectively.

2.4   Plasma density measurements

Plasma density is typically measured by interferometry, Thomson scattering, and in the edge when conditions permit, Langmuir probes. In this work we will use primarily interferometer measurements due to their extremely good time resolution which, as we will discuss, is key to several types of analyses in this work. However, Thomson scattering profiles were still valuable as they provided density and temperature information which were used to assess general changes (or lack of changes) in overall density and temperature profiles.

At HSX, the 9-channel microwave interferometer [38, 39] provides both chord-averaged measurements and also a density profile using an inversion technique [39, 40]. The channels are located in one of the HSX boxports with 1.5 cm spacing. It has a time resolution of 200 kHz which provides substantially more information than the Thomson scattering system (2 time points per 50 ms discharge) [41]. For this reason the HSX interferometer was used as the main diagnostic for plasma density analysis. In general reasonable agreement has been shown between the densities measured by these two diagnostics.

At W7-X, a single channel interferometer was available in OP 1.1 [42, 43]. The interferometer shared a line of sight with the Thomson scattering and had a sample frequency of 50 kHz.

As a result, no density profile could be provided by means of an inversion. However, Thomson scattering produced density and temperature profiles at a rate of 10 Hz [44, 45]. Since the W7-X interferometer produced data at a much higher time resolution, it was therefore used as the main diagnostic for density measurements.

2.4.1 Total number of plasma particles

Measurements of the line-averaged density were necessary to determine the following quantities that will later be used: total number of plasma particles, N_{tot}, which is a product of the line-averaged density $\bar{n}_e$ and the confinement volume, $V_{\text{confinement}}$, and the time-derivative of the change in total number of particles, $\frac{dN_{tot}}{dt}$. Under steady-state conditions , $\frac{dN_{tot}}{dt} = 0$. If conditions are not steady-state, $\frac{dN_{tot}}{dt}$ can be included as necessary. This is the general form of each of the terms we will use in the particle balance analysis (Equation 2.2):

$$N_{tot} = \bar{n}_e V_{\text{confinement}} \tag{2.4}$$

and

$$\frac{dN_{tot}}{dt} = \frac{d\bar{n}_e}{dt} V_{\text{confinement}} \tag{2.5}$$

It is important to note that the line-averaged density $\bar{n}_e$ is averaged over the 1-D interferometer path length, and is **not** a true volume-averaged density. Therefore it may overestimate the total number of particles since $\bar{n}_e$ will over-emphasize the contribution of the high-density but small volume core. In general this overestimation will be systematic between magnetic configurations. This same procedure is used at both HSX and W7-X since this is the only density measurement available for every plasma discharge analyzed in this work.
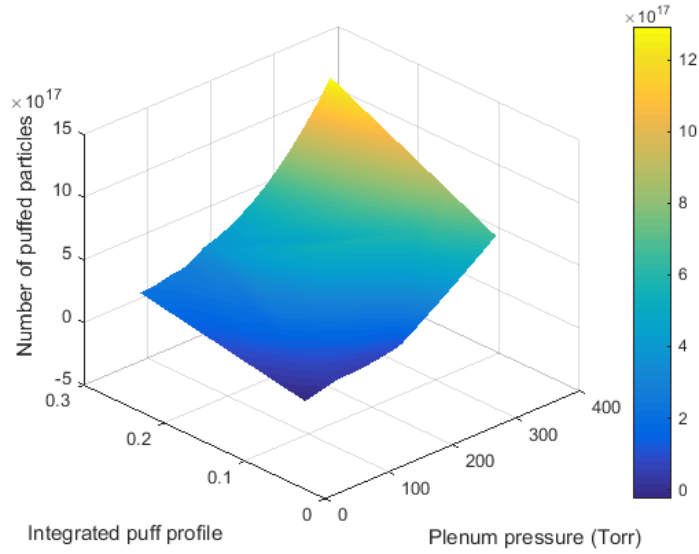
Figure 2.3 Interpolation of gas puff calibration data for hydrogen. The number of puffed particles are both a function of plenum pressure and the integrated pulse train sent to the gas puff.

2.5   Gas puff flux

At HSX, given the integrated puff profile and the known pressure of the gas plenum, the total number of puffed particles can be calculated after a plasma shot. This 2-D lookup table is illustrated in Fig. 2.3 for hydrogen and a similar table was created for helium. Codes to calculate total number of particles for both the HSX standard C puffer and SGI perturbative puffer are located at `Y: /Puff_calibration/c_puff_particles` and `Y:/Puff_calibration/sgi_puff_particles` and require the date, shot, and plenum pressure of the system.

At W7-X, the main gas fueling occurred before ECRH start and there was no additional fueling required after this time as the density usually increased monotonically during these shots (most likely due to poor wall/limiter conditioning, as will be discussed in Chapter 5). For this reason it was not necessary to know the throughput of the main gas fueling system since it was not active during our analysis window, i.e. there is no Φ_{gas} term in the W7-X particle balance.

While also not required for the W7-X particle balance, the particle throughput of the perturbative injection system was calibrated. This perturbative helium injection was used to calculate τ_p^*. This system was calibrated by M. Krychowiak before the beginning of OP 1.1 [46]. Each pertubative helium gas injection was identical and consisted of a 20 ms pulse. Using the calibration data, this pulse was known to provide 1×10^{19} particles per 20 ms injection, or a total particle flux of 5×10^{20} particles/s (roughly factor of 10 below the wall and limiter particle source rates, as will be shown in Chapter 5).

2.6   Filter-based spectroscopy

Spectroscopic measurements are a non-perturbative means of measuring plasma line-integrated emission intensity, and through that, plasma particle flux. A brief summary of this technique, drawing heavily from [47] will now be presented.

The emission coefficient for a spectral line from a species that has been excited to a level above the ground state is:

$$\epsilon = \frac{\Gamma}{4\pi} n_A n_e < \sigma_{Ex} v_e > \tag{2.6}$$

where ϵ is the emission coefficient with units [s^{-1} sr^{-1} m^{-3}], Γ is the branching ratio between excitation and de-excitation (radiation), n_A is the species density, n_e is the plasma density, and $< \sigma_{Ex} v_e >$ is the excitation rate coefficient (Equation 3 in [47]).

The line-integrated intensity of this emission can be expressed as:

$$I_{tot} = h\nu \int_{r_1}^{r_2} \epsilon(r) dr = \Gamma \frac{h\nu}{4\pi} \int_{r_1}^{r_2} n_A(r) n_e(r) < \sigma_{Ex} v_e > dr \tag{2.7}$$

where I_{tot} is the line-integrated intensity with units [W sr^{-1} m^{-2}], $n_A(r)$ is the species profile and $n_e(r)$ is the electron density profile (Equation 4 in [47]).

If we assume the number of particles entering the plasma, Φ_A, with velocity v_A is equal to the number of ionization events (i.e. every neutral particle is ionized and therefore becomes a plasma

particle), we can write:

$$\frac{d\Phi_A(r)}{dr} = -\frac{d(n_A v_A)}{dr} = n_A(r)n_e(r) < \sigma_I v_e > \tag{2.8}$$

where $< \sigma_I v_e >$ is the collisional ionization rate coefficient. This is Equation 5 in [47].

If we integrate Equation 2.8 over the whole attenuation length of the emission, we can write:

$$\Phi_A = \int_{r_1}^{r_2} n_A(r)n_e(r) < \sigma_I v_e > dr \tag{2.9}$$

which is Equation 6 in [47].

If we now take the ratios of Equations 2.9 and 2.7 and solve for Φ_A, we can relate the particle flux to the plasma density:

$$\Phi_A = 4\pi \frac{I_{tot}}{\Gamma h\nu} \frac{\int_{r_1}^{r_2} n_A(r)n_e(r) < \sigma_I v_e > (r)dr}{\int_{r_1}^{r_2} n_A(r)n_e(r) < \sigma_{Ex} v_e > (r)dr} \tag{2.10}$$

which is Equation 7 in [47]. This therefore allows the particle flux to be calculated provided that the intensity of the excited emission I_{tot} is known, along with the background plasma density and rate coefficients for ionization and excitation.

However, since typically the ratio between $< \sigma_I v_e > / < \sigma_{Ex} v_e >$ is only weakly dependent on the background plasma temperature and density, Equation 2.10 can be simplified to the following:

$$\Phi_A = \frac{4\pi}{\Gamma} \frac{I_{tot}}{h\nu} \frac{< \sigma_I v_e >}{< \sigma_{Exg} v_e >} = 4\pi \frac{I_{tot}}{h\nu} \frac{S}{XB} \tag{2.11}$$

where S is defined as $< \sigma_I v_e >$, X is defined as $< \sigma_{Exg} v_e >$, and B is defined as Γ. These quantities are known as the collisional ionization rate coefficient, the excitation rate coefficient, and the branching ratio, respectively. It is through this ratio, commonly referred to as the S/XB ratio, that the measured line-integrated intensity can be converted into a particle flux. An example of this ratio for hydrogen is shown in Fig. 2.4. Thus using the known S/XB ratio for the species of interest, the measured line-integrated intensity of that particular emission line can be used to
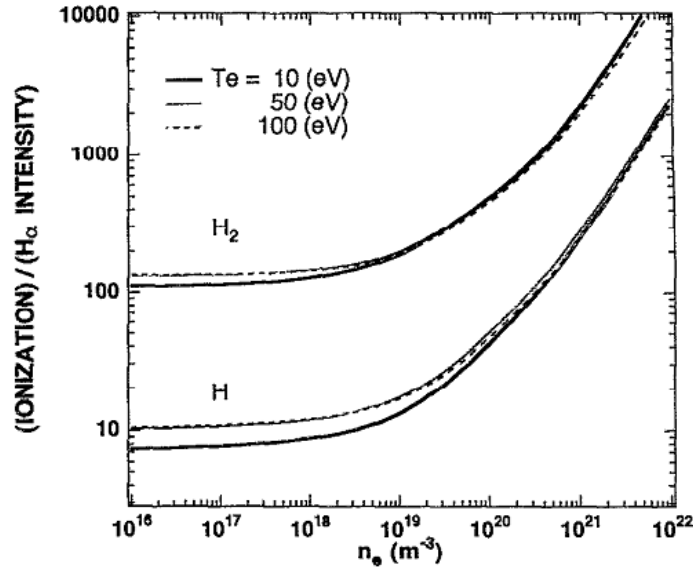
Figure 2.4 The relationship between ionization events and H-alpha photons emitted, the so-called S/XB coefficient (ionization to excitation ratio). This is the ratio of the ionization rate to the product of the branching ratio and the excitation rate. Figure reproduced from [48].

determine the particle flux, Φ_A. In this work, this technique was specifically used to convert measured H$_\alpha$ emission into the number of hydrogen particles entering the plasma at both HSX and W7-X.

2.6.1 Thin film bandpass filters: powerful but delicate tools

Filters are means by which a particular emission line or lines can be allowed to pass and the undesirable background can be attenuated. Typically these type of filters are called narrowband or bandpass filters. This ability to selectively pass a narrow wavelength is usually a result of a thin layer periodic stack that produces an interference filter (also known as an etalon) [49].

While filters can be powerful, they are not without their limitations. They often have a full-width-half-max (FWHM) of 1-5 nm, which is often large enough to pass one or more emission lines in addition to the emission line of interest. This means there can be some uncertainty in the final measured quantity due to the contribution of undesirable impurity contributions. There will also

be some contribution from the continuous background emission known as visible Bremsstrahlung (VB).

Due to their fragile thin layer stack construction, filters also degrade over time. When this occurs, typically the filter passband shifts to longer wavelengths (i.e. it is red-shifted). This is especially problematic in narrower filters which have less tolerance for such a shift.

The W7-X filterscope and the HSX filtered photodiode array rely on the integrity of their narrowband filters to pass the desired emission lines through to the photomultiplier tube or the photodiode, respectively. However, it was discovered that several of the filters installed in the filterscope diagnostic for OP 1.1 were old, damaged, or perhaps initially red-shifted. Since the transmission curves of the filters were not measured before the experimental campaign, it is hard to determine the cause of the problem.

Once the transmission spectra of the filters were measured, it was clear that several of the channels collected unusable data. The filters were so substantially red-shifted that the desired wavelength of light, either H_α or H_β, were essentially not able to pass through the filter, rendering the signals they collected useless. As an example, four filter traces are shown in Fig. 2.5.

As a result, the data collected using filters shown in Fig. 2.5(a) and (b) were not usable. Filters (c) and (d) in this figure, though they were also somewhat red-shifted, still provided usable data because the H_α line passed through a portion of the filter in a reasonable transmission range (between 20-30 percent). Filter (c) corresponded to a wall-viewing filterscope channel in module 5 from port L51. Filter (d) corresponded to the limiter-viewing channel on limiter 3 from port A30. These two measurements were therefore used to infer the wall particle flux and limiter particle flux, respectively.
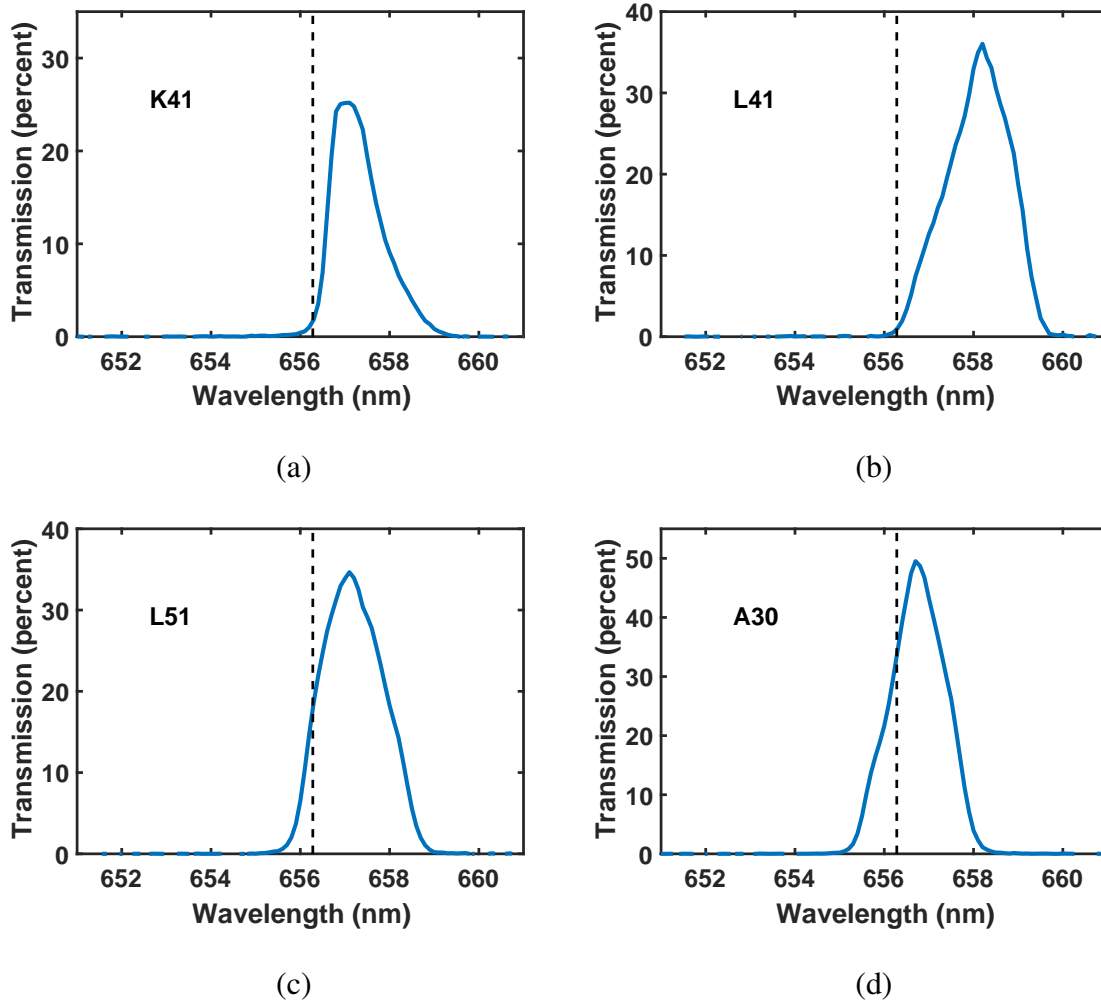
Figure 2.5 Transmission curves of the four H$_\alpha$ filters used in the filterscope diagnostic during OP 1.1. These curves indicate that all four filters were red-shifted to some degree, with some filters more dramatically shifted than others. (a) Filter used for measurement in port K41. (b) Filter used for measurement in port L41. (c) Filter used for measurement in port L51. (d) Filter used for measurement in port A30 (viewing limiter 3). Data collected from the L41 and K41 filtered channels were unusable as a result of these substantial red-shifted curves. Measurements courtesy of P. Kornejew.
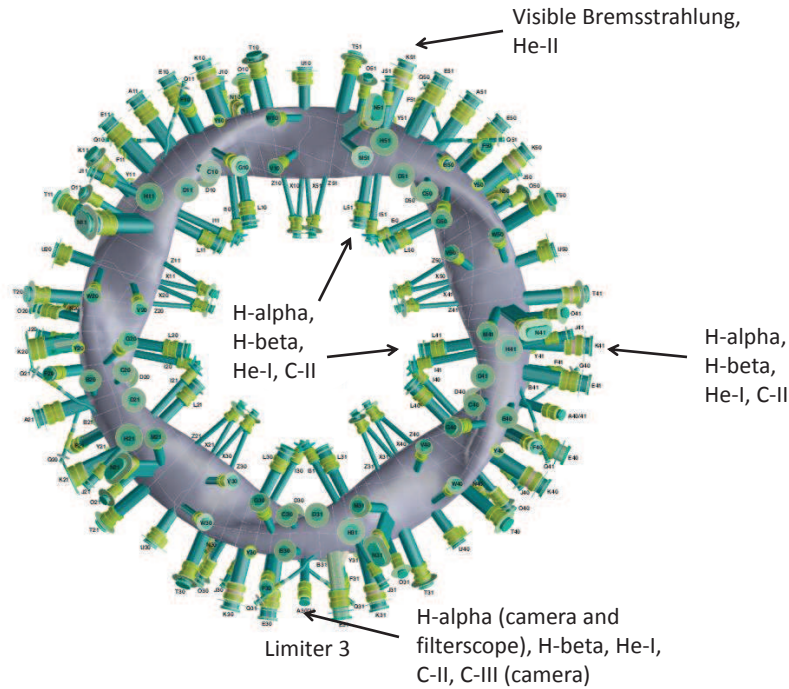
Figure 2.6 Location of camera system and filterscope views on W7-X during OP 1.1. Both systems were used to make measurements of limiter 3 (bottom). The types of spectral data obtained at each location are noted. The perturbative gas injection system was located in module 5 near the He-II/visible Bremsstrahlung (VB) measurement location.

2.6.2 W7-X Filterscope

The filterscope system, developed and provided by Oak Ridge National Laboratory, is a well-established diagnostic system and has been previously described in detail, so it will not be repeated here [50, 51, 52]. Rather, the application of the filterscope as part of an edge diagnostic system at W7-X will be discussed.

The ORNL W7-X filterscope system for OP 1.1 was comprised of 24 Hamamatsu photomultiplier tubes with individually adjustable control voltages and a time resolution of up to 10 microseconds. LabView software controlled the data acquisition and populates a local MDSplus tree [53]. An automated Python routine was used to copy the local MDSplus tree to the main W7-X MDSplus tree after each plasma discharge. A more detailed description of the W7-X filterscope

Spectral line	Wavelength (nm)	Information
H-α	656.3	H^0 flux
He-I	667.8	He^0 flux, $\tau^*_{p,\text{He-I}}$
He-II	468.6	He^{+1} flux, $\tau^*_{p,\text{He-II}}$

Table 2.1 Summary of the important spectral lines used at W7-X and the information that they provide. These were measured using a filterscope diagnostic. Note that other lines were measured but are not analyzed as a part of this study.

system can be found in [54]. This system was calibrated and installed at W7-X as a part of this work.

A narrowband interference filter was placed in front of each photomultiplier to provide measurements of the desired emission line (typically 1-3 nm FWHM). A beamsplitter was used to divide the light from a single fiber into four spectral channels. The locations of the filterscope fibers on W7-X and the species they measured is shown in Fig. 2.6. The emission lines and the information they yield are detailed in Table 2.1.

This system was absolutely calibrated following OP 1.1 so that the measured voltages could to converted into line-integrated emission intensity, and using an S/XB coefficient, into hydrogen particle flux. A Labsphere model UK2 integrating sphere with known spectral radiance as a function of wavelength was used to calibrate all channels, end-to-end. The transmission of each filter was measured using a Perkin Elmer Lambda 900 spectrophotometer. The range of PMT control voltages and exposure times were scanned for the filterscopes to develop a matrix to convert the measured voltages or counts to line-integrated photon emission. The line-integrated H_α emission was used to determine limiter and wall particle flux, key components of the W7-X particle balance. This will be discussed in Chapter 5.

Spectral line	Wavelength (nm)	Information
H-α	656.3	H^0 flux
He-II	468.6	He^{+1} flux, $\tau^*_{p,\text{He-II}}$

Table 2.2 Summary of the important spectral lines used at HSX and the information that they provide. These were measured using a filtered photodiode system. Note that other lines were measured but are not analyzed as a part of this study.

2.6.3 HSX filtered photodiode system

The HSX filtered photodiode system was designed and installed by S. Gerhardt [55] and used heavily by J. Canik [56]. The original system was comprised of 16 detectors with an H$_\alpha$ filter of 10 nm FWHM (a relatively wide filter). The red-enhanced photodiodes have a response of 1KHz providing approximately 50 samples per HSX discharge.

Nine of these channels were positioned in field period C near the main gas fueling location in the miniflange poloidal array illustrated in Fig. 2.7. This meant that they collected primarily H$_\alpha$ light from the gas injection sourced particles. The other seven channels were positioned toroidally around HSX in stellarator symmetric views (port 5 in each miniflange array). Each view provided a stellarator symmetric but toroidally shifted line of sight through the magnetic axis and subsequently little edge information. This system was absolutely calibrated using an integrating sphere to provide the conversion matrix from measured voltage to measured line-integrated emission.

In 2015, the system was upgraded as a part of this work. First, an additional 20 detectors were added, bringing the total number to 36 from 16. Second, all the previous H$_\alpha$ filters were replaced with new, custom filters with a 2 nm FWHM to reduce background and possible impurity contributions. Four additional H$_\alpha$ filters were added, resulting in 20 total H$_\alpha$ detectors. Since helium plasma studies were planned, eight 468.6 nm He-II filters were added with a 2.5 nm FWHM
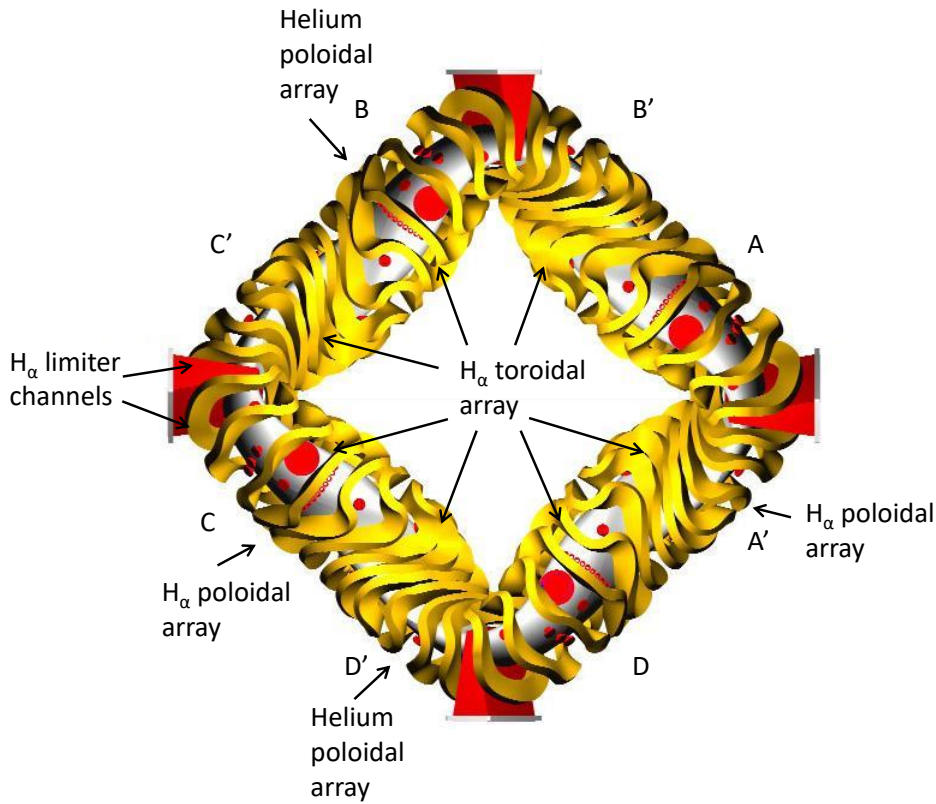
Figure 2.7 Illustration of the upgraded HSX filtered photodiode arrays. Note the toroidal H_α array, the two poloidal H_α arrays, and the two poloidal helium detector arrays. Note also the two limiter-viewing H_α detectors. The HSX main gas fueling is located in field period C and the perturbative puff is located in field period B.

and seven 587.6 nm He-I filters were included with a 2 nm FWHM. The final channel was left unfiltered to obtain general visible light information. This information documenting the capabilities of the upgraded array is shown in Table 2.3. The spectral lines measured in this work are shown in Table 2.2. More detailed information about this system and how to use it can be found in `Y:/FilteredPhotodiodeArray`.

The additional number of detectors allowed them to be distributed more widely around HSX. The original 9-channel poloidal array viewing the gas injection was reduced to 5 channels since the previous measurement density was not necessary. (The smooth exponential falloff of the H_α

emission as a function of channel number could be easily matched with 5 rather than 9 detectors.) The position of the original 7-channel H$_\alpha$ toroidal array was not altered. An additional 7-channel H$_\alpha$ poloidal array was added in field period A-prime. This array is especially valuable because it can provide a profile of H$_\alpha$ emission that is not influenced by the gas injection. Two H$_\alpha$ detectors were added at the top and bottom of boxport C to monitor HSX limiter emission, if limiters are inserted. (The limiters were not inserted for any of the experiments in this work.) Finally, two poloidal arrays comprised of both He-I and He-II detectors are located in D-prime and B. The unfiltered detector is located in port 4 in D-prime. A diagram of the upgraded filtered photodiode system is shown in Fig. 2.7.

2.6.4   Spectroscopically determined wall particle flux

Before the method to determine the wall particle flux is described, a brief background on how particles collide with the wall is necessary. Plasma particles exit the plasma confinement region through either parallel transport (which occurs along field lines), or perpendicular transport. Studies at HSX have confirmed that most edge plasma transport is parallel due to the standard range of edge temperatures and densities [21]. In addition to this plasma transport towards the wall, neutral particles may also exit the confinement region as a result of charge-exchange. In a charge-exchange collision, a neutral particle (in this case, hydrogen) exchanges its electron with a plasma particle, often resulting in a relatively low-energy plasma particle and a high-energy neutral particle, Chapter 1 Section 1.8 in [6]. These neutral particles are not influenced by magnetic geometry, and are thus incident in a more uniform distribution on the wall. Once either a plasma or neutral particle collides with the wall, it is usually re-emitted as neutral hydrogen molecule. This is the process of wall recycling that results in a wall-sourced particle flux.

In general the manner in which Φ_{wall} is determined varies quite a bit between HSX and W7-X. At HSX, where the wall itself functions as a pseudo-divertor (in the Edge-Islands configuration),

the particle flux footprint is distributed in bands that wrap around the machine in a helical manner [57]. This is the result of primarily parallel transport along field lines, most of which intersect the HSX wall in the regions of high curvature, resulting in this helical footprint. At this time, the best way to assess the strength of this wall source is through a collection of local line-integrated H_α measurements that are used to scale DEGAS [58] calculations and extrapolate this scale factor to the remainder of the wall area. This process will be described in more detail in Chapter 3. These scaled DEGAS calculations then provide Φ_{wall} in each HSX configuration.

At W7-X, which had five inboard limiters, only a small fraction of field lines directly intersected the wall. As a result, the wall particle source was substantially more uniform than that at HSX. This is because particles from the wall were primarily sourced by plasma ions neutralized through charge-exchange which then recycled at the wall. Based on images provided by visible cameras, the wall particle source was estimated to be approximately uniform along the inboard half of the wall. Therefore the filterscope measured H_α photon emission was translated to a particle flux via an S/XB coefficient, and this particle flux was used to determine the total wall-source contribution, Φ_{wall}, in each configuration. This will be discussed in detail in Chapter 5.

2.6.5 Spectroscopically determined limiter particle flux

The limiter flux term was only necessary for the W7-X particle balance. (No limiters were used at HSX for this work, although there are two retractable limiters currently installed.) Similar to the manner in which the W7-X wall flux was estimated, the limiter flux measurements were made using the H_α channel of the filterscope diagnostic. The photon emission measured from this channel, which was facing limiter 3, was then multiplied by the appropriate S/XB coefficient to translate the photon emission into a particle flux. This particle flux was then assumed to be representative of all five limiters and was subsequently multiplied by the total surface area of all

the limiters, assuming that all limiters source particles uniformly. This procedure yielded the total Φ_{lim}. This will be discussed in detail in Chapter 5.

2.7   Summary and applications

This chapter has provided a summary of the types of experimental measurements and techniques on which this study will rely. Together these measurements and analysis methods are used to investigate the particle fueling and confinement physics at both W7-X and HSX and will used and referred to extensively in the chapters that follow.

Channel number	Spectral line	Center wavelength	Filter FWHM	Port number
1	H_α	656.44	1.74 nm	C1
2	H_α	656.42	1.75 nm	C2
3	H_α	656.43	1.74 nm	C4
4	H_α	656.46	1.75 nm	C5
5	H_α	656.40	1.75 nm	C6
6	H_α	656.39	1.75 nm	Boxport C bottom
7	H_α	656.44	1.76 nm	C9
8	H_α	656.50	1.75 nm	Boxport C top
9	H_α	656.45	1.74 nm	CP5
10	H_α	656.47	1.75 nm	DP5
11	H_α	656.47	1.74 nm	AP1
12	H_α	656.50	1.74 nm	AP2
13	H_α	656.43	1.75 nm	AP4
14	H_α	656.41	1.74 nm	AP5
15	H_α	656.42	1.74 nm	BP5
16	H_α	656.46	1.75 nm	D5
17	H_α	656.33	1.76 nm	B5
18	H_α	656.51	1.75 nm	AP6
19	H_α	656.39	1.74 nm	AP8
20	H_α	656.49	1.74 nm	AP9
21	He-I	587.73	1.85 nm	B1
22	He-I	587.50	1.82 nm	B2
23	He-I	587.57	1.83 nm	B9
24	He-I	587.50	1.82 nm	DP8
25	He-I	587.69	1.85 nm	DP9
26	He-I	587.64	1.84 nm	DP1
27	He-I	587.630	1.84 nm	DP2
28	He-II	587.58	1.83 nm	B3
29	He-II	468.98	2.39 nm	B4
30	He-II	468.91	2.38 nm	B6
31	He-II	468.95	2.38 nm	B8
32	He-II	468.92	2.38 nm	DP6
33	He-II	468.91	2.36 nm	DP7
34	He-II	468.930	2.38 nm	DP3
35	He-II	468.95	2.38 nm	DP4
36	no filter	n/a	n/a	CP4

Table 2.3 Summary of the upgraded HSX filtered photodiode system.

References

6. Stangeby, P. C. *The plasma boundary of magnetic fusion devices* 717 pp. ISBN: 978-0-7503-0559-4 (Institute of Physics Pub, Bristol ; Philadelphia, 2000).

21. Akerson, A. R., Bader, A., Hegna, C. C., Schmitz, O., Stephey, L. A., Anderson, D. T., Anderson, F. S. B. & Likin, K. M. Three-dimensional scrape off layer transport in the helically symmetric experiment HSX. *Plasma Physics and Controlled Fusion* **58,** 084002. ISSN: 0741-3335, 1361-6587 (1st Aug. 2016).

22. Schmitz, O., Ida, K., Kobayashi, M., Bader, A., Brezinsek, S., Evans, T., Funaba, H., Goto, M., Mitarai, O. & Morisaki, T. Enhancement of helium exhaust by resonant magnetic perturbation fields at LHD and TEXTOR. *Nuclear Fusion* **56,** 106011. ISSN: 0029-5515 (2016).

33. Dylla, H. F., LaMarche, P. H., Ulrickson, M., Goldston, R. J., Heifetz, D. B., Hill, K. W. & Ramsey, A. T. Conditioning of the graphite bumper limiter for enhanced confinement discharges in TFTR. *Nuclear fusion* **27,** 1221 (1987).

34. Hillis, D., Finken, K., Hogan, J., Dippel, K., Moyer, R., Pospieszczyk, A., Rusbüldt, D., Akaishi, K., Conn, R. & Euringer, H. Helium exhaust and transport studies with the ALT-II pump limiter in the TEXTOR tokamak. *Physical review letters* **65,** 2382 (1990).

35. Schmitz, O., Coenen, J., Frerichs, H., Kantor, M., Lehnen, M., Unterberg, B., Brezinsek, S., Clever, M., Evans, T., Finken, K., Jakubowski, M., Kraemer-Flecken, A., Phillips, V., Reiter, D., Samm, U., Spakman, G. & Telesca, G. Particle confinement control with resonant magnetic perturbations at TEXTOR. *Journal of Nuclear Materials* **390-391,** 330–334. ISSN: 00223115 (2009).

36. Soukhanovskii, V., Maingi, R., Raman, R., Kugel, H., LeBlanc, B., Roquemore, A., Skinner, C. & NSTX Research Team. Core fueling and edge particle flux analysis in ohmically and

auxiliary heated NSTX plasmas. *Journal of nuclear materials* **313,** 573–578. ISSN: 0022-3115 (2003).

37. Maingi, R., Jackson, G. L., Wade, M. R., Mahdavi, M. A., Mioduszewski, P. K., Haas, G., Schaffer, M. J., Hogan, J. T. & Klepper, C. C. Control of wall particle inventory with divertor pumping on DIII-D. *Nuclear fusion* **36,** 245 (1996).

38. Brower, D. L., Deng, C., Ding, W. X., Anderson, D. T. & Mason, W. Multichannel interferometer system for the helically symmetric experiment. *Review of Scientific Instruments* **72,** 1081. ISSN: 00346748 (2001).

39. Deng, C., Brower, D. L., Ding, W., Almagri, A. F., Anderson, D. T., Anderson, F. S. B., Gerhardt, S. P., Probert, P. & Talmadge, J. N. First results from the multichannel interferometer system on HSX. *Review of scientific instruments* **74,** 1625–1628. ISSN: 0034-6748 (2003).

40. Park, H. K. A new asymmetric Abel-inversion method for plasma interferometry in tokamaks. *Plasma physics and controlled fusion* **31,** 2035 (1989).

41. Zhai, K., Anderson, F. S. B., Willis, K., Likin, K. & Anderson, D. T. Performance of the Thomson scattering diagnostic on Helical Symmetry Experiment. *Review of Scientific Instruments* **75,** 3900–3902. ISSN: 0034-6748, 1089-7623 (Oct. 2004).

42. Kornejew, P., Hirsch, M., Bindemann, T., Dinklage, A., Dreier, H. & Hartfuß, H.-J. Design of multichannel laser interferometry for W7-X. *Review of scientific instruments* **77,** 10F128. ISSN: 0034-6748 (2006).

43. Knauer, J., Kornejew, P., Mora, H. T., Hirsch, M., Werner, A. & Wolf, R. *A New Dispersion Interferometer for the Stellarator Wendelstein 7-X* in *EPS Conference on Plasma Physics* (European Physical Society, 2016).

44. Pasch, E., Beurskens, M., Bozhenkov, S., Fuchert, G., Knauer, J. & Wolf, R. The Thomson scattering system at Wendelstein 7-X. *Review of Scientific Instruments* **87,** 11E729. ISSN: 0034-6748 (2016).

45. Pasch, E., Beurskens, M., Bozhenkov, S., Fuchert, G., Hirsch, M., Höfel, U., Knauer, J., Kornejew, P., Langenberg, A. & Wolf, R. *First Results from the Thomson Scattering System at the Stellarator Wendelstein 7-X* in. 43rd EPS Conference on Plasma Physics (European Physical Society, 2016).

46. Krychowiak, M. *et al.* Overview of diagnostic performance and results for the first operation phase in Wendelstein 7-X (invited). *Review of Scientific Instruments* **87,** 11D304 (2016).

47. Pospieszczyk, A. Diagnostics of edge plasmas by optical methods. *Atomic and Plasma-Material Interaction Processes in Controlled Thermonuclear Fusion,* 213–242 (1993).

48. Sawada, K., Eriguchi, K. & Fujimoto, T. Hydrogen-atom spectroscopy of the ionizing plasma containing molecular hydrogen: Line intensities and ionization rate. *Journal of Applied Physics* **73,** 8122. ISSN: 00218979 (1993).

49. Hecht, E. & Zajac, A. Optics Addison-Wesley. *Reading, Mass* **19872,** 350–351 (1974).

50. Colchin, R., Hillis, D., Maingi, R., Klepper, C. & Brooks, N. The filterscope. *Review of scientific instruments* **74,** 2068–2070. ISSN: 0034-6748 (2003).

51. Brooks, N. H., Colchin, R. J., Fehling, D. T., Hillis, D. L., Mu, Y. & Unterberg, E. Filterscopes: Spectral line monitors for long-pulse plasma devices. *Review of Scientific Instruments* **79,** 10F330. ISSN: 00346748 (2008).

52. Unterberg, E. A., Schmitz, O., Fehling, D. H., Stoschus, H., Klepper, C. C., Muñoz-Burgos, J. M., Van Wassenhove, G. & Hillis, D. L. HELIOS: A helium line-ratio spectral-monitoring

diagnostic used to generate high resolution profiles near the ion cyclotron resonant heating antenna on TEXTOR. *Review of Scientific Instruments* **83,** 10D722. ISSN: 00346748 (2012).

53. Stillerman, J., Fredian, T., Klare, K. & Manduchi, G. MDSplus data acquisition system. *Review of Scientific Instruments* **68,** 939–942. ISSN: 0034-6748 (1997).

54. Stephey, L., Wurden, G. A., Schmitz, O., Frerichs, H., Effenberg, F., Biedermann, C., Harris, J., König, R., Kornejew, P., Krychowiak, M., Unterberg, E. A. & the W7-X Team. Spectroscopic imaging of limiter heat and particle fluxes and the resulting impurity sources during Wendelstein 7-X startup plasmas. *Review of Scientific Instruments* **87,** 11D606. ISSN: 0034-6748, 1089-7623 (Nov. 2016).

55. Gerhardt, S., Canik, J., Anderson, D. & Owen, L. Ha detector system for the Helically Symmetric Experiment. *Review of scientific instruments* **75,** 2981–2984. ISSN: 0034-6748 (2004).

56. Canik, J. M., Anderson, D. T., Anderson, F. S. B., Likin, K. M., Talmadge, J. N. & Zhai, K. Experimental Demonstration of Improved Neoclassical Transport with Quasihelical Symmetry. *Physical Review Letters* **98.** ISSN: 0031-9007, 1079-7114. http://link.aps.org/doi/10.1103/PhysRevLett.98.085002 (2016) (23rd Feb. 2007).

57. Canik, J. M. *Experimental verification of reduced particle and electron heat transport with Quasisymmetry in the HSX stellarator* PhD thesis (Univeristy of Wisconsin - Madison, 2007).

58. Heifetz, D., Post, D., Petravic, M., Weisheit, J. & Bateman, G. A Monte-Carlo model of neutral-particle transport in diverted plasmas. *Journal of Computational Physics* **46,** 309–327 (1982).

Chapter 3

DEGAS and EMC3-EIRENE numerical modeling

3.1 Introduction to modeling

Experimental measurements are important, but they need to be fit into some physics framework. Given the complex 3-D geometry of both W7-X and HSX and the statistical nature of the atomic physics processes that govern particle ionization, numerical tools are necessary to adequately represent the nature of particle behavior in these experiments.

This work relies heavily on information provided by two numerical models: the DEGAS code (used for HSX) and the EMC3-EIRENE coupled codes (used for both HSX and W7-X). In general each model is used to calculate neutral particle and plasma source behavior and will be described in more detail below.

The most important quantity that DEGAS provides is the HSX wall particle source contribution, Φ_{wall} (as discussed in Chapter 2). The most important quantity that EMC3-EIRENE provides is the fueling efficiency (f_{eff}, see Equation 2.3) for particles in both HSX and W7-X. As will be discussed in Chapters 4 and 5, this quantity is a vital piece of the particle balance. How both of these terms are calculated will be described in detail in what follows.

3.2 The DEGAS code

DEGAS [58] is a Monte-Carlo, neutral particle code. It can simulate the fully three-dimensional geometry of the HSX stellarator. Much about the application of the DEGAS code to the HSX stellarator has been discussed in [56] and [57], so only a brief overview will be given here. The DEGAS background plasma profiles are 1-D radial profiles that have been mapped onto a 3-D geometry. The DEGAS grid was generated using magnetic field line following so that the shape of the grid follows the HSX magnetic flux surfaces. This is the procedure used inside the LCFS. Outside the LCFS, surfaces are extrapolated between the LCFS and the wall. (This is because DEGAS grid generation procedure is not well-suited to capturing the edge island geometry and would need to be completely re-developed to insert edge island regions. This effort does not make sense when EMC3-EIRENE already exists and both includes plasma transport and can also accurately simulate the HSX edge magnetic geometry, as will be discussed below.) Nevertheless, DEGAS does offer several advantages in that it already incorporates the HSX filtered photodiode measurement geometry, and is able to easily provide the predicted H_α emission measured by these detectors.

The DEGAS background plasma is static and based on Thomson scattering data for the electron density and temperature. Ion temperature profiles are based on CHERS (Charge-exchange recombination spectroscopy) measurements and assumed to be parabolic in the core and flat in the edge [29].

The HSX vacuum vessel wall is represented as a mesh of triangles in DEGAS. Each of these triangles can act as a neutral particle source, the magnitude of which is prescribed by the user. Neutral particles are launched into the DEGAS background plasma from these triangles and undergo Monte-Carlo interactions which include electron impact ionization, ion impact ionization, charge-exchange, or molecular dissociation. One a particle is ionized, the ionization location is

Process name	Mechanism
Electron impact ionization, H *	$e + H \rightarrow e + H^+ + e$
Charge exchange, H *	$H^+ + H \rightarrow H + H^+$
Disassociative excitation, H_2 *	$e + H_2 \rightarrow e + H + H$
Electron impact ionization, H_2 *	$e + H_2 \rightarrow e + H_2^+ + e$
Dissociative ionization, H_2 *	$e + H_2 \rightarrow e + H^+ + H + e$
Charge exchange, H_2	$H_2 + H_2^+ \rightarrow H_2^+ + H_2$
Charge exchange, H and H_2	$H_2 + H^+ \rightarrow H + H_2^+$
Proton impact ionization, H	$H + H^+ \rightarrow 2H^+ + e$
Proton impact ionization, H_2	$H_2 + H^+ \rightarrow H_2^+ + H^+ + e$
Recombination*	$e + H_2^+ \rightarrow 2H$
Disassociative excitation, H_2^+ *	$e + H_2^+ \rightarrow H + H^+ + e$
Disassociation ionization, H_2^+ *	$e + H_2^+ \rightarrow 2e + 2H^+$

Table 3.1 A list of the atomic physics reactions included in DEGAS. The reactions marked with an asterisk are included by default in EMC3-EIRENE.

noted and the particle is no longer simulated. Table 3.1 includes a list of the atomic physics reactions included in DEGAS.

3.3 Updates to previous DEGAS results

The DEGAS results used in this work differ somewhat from those published by J. Canik [56, 57]. The first major difference is the number of "test-flights" (DEGAS terminology for number of Monte-Carlo particles) used for the calculation: 50k were used in previous work and 1M were used in this study, which greatly reduces the Monte-Carlo noise in the results. The second major difference is that the puffed and recycled particles have a Maxwellian energy distribution, rather than mono-energetic distribution. This difference is chiefly responsible for the change in neutral density profile shape, most noticeably in the edge. The third major difference is the manner in which the edge recycling source is defined. This will be described in detail in Section 3.3.1. Finally, a different scaling procedure, made possible by the installation of additional filtered photodiode detectors, also accounts for the differences in absolute value of neutral density as compared to previous results. This new scaling procedure will also be described in detail below in Section 3.3.2.

3.3.1 Improved wall recycling source definition

The DEGAS code is very flexible in terms of how fueling sources are defined. Gas puff sources and wall recycling sources can be included at any wall triangle, and a separate source rate can be specified for each triangle. The source rate is the number of particles sourced per second per wall triangle. In DEGAS, all neutral hydrogen particles are sourced as H_2 (molecular hydrogen). In previous work [56], the DEGAS strike-points were assigned based on the results of field line following from points launched 2 mm outside the LCFS. The locations of where these field lines intersected the vessel wall were recorded. If the field line hit inside one of the wall triangles, the triangle was classified as a source. If no field lines hit, the triangle was not classified as a source. In situations where several field lines were incident within the same triangle, the resultant source
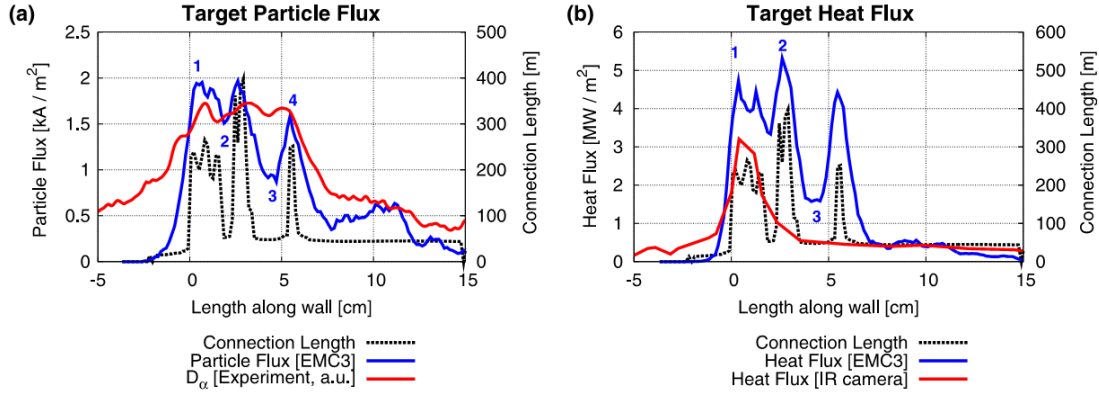
Figure 3.1 Figure reproduced from [59]. (L) Plot showing connection length (black dotted line), EMC3-EIRENE simulated particle flux (blue line), and experimentally measured D_α (red line) at the DIII-D divertor. (R) A similar plot, showing connection length (black dotted line), EMC3-EIRENE simulated heat flux (blue line), and experimentally measured heat flux (red line) at the DIII-D divertor.

rates were added to produce a total source rate. No distinction was made between long or short connection lengths.

In this work a different method of defining the wall triangle source was used. It was meant to be a more physically accurate representation of the source instead of the binary source model employed in the past. Frerichs et al. have shown that the heat and particle flux measured on divertor tiles is related to the connection length of the incident field lines [59]. They demonstrate that the longer connection length field lines are, in general, more deeply penetrating field lines, which in turn carry more heat flux. A figure from this study is reproduced in Fig. 3.1 to demonstrate this relationship. Since this study was conducted in the DIII-D tokamak with 3-D edge magnetic geometry resulting from RMP coils, this gives some credence to the idea that the 3-D stellarator edge may exhibit a similar correlation.

A source rate linearly proportional to the connection length of each field line incident within the wall triangle was assigned based on the results from DIII-D [59]. In situations where several field lines were incident within a single wall triangle, the respective source rates were added to
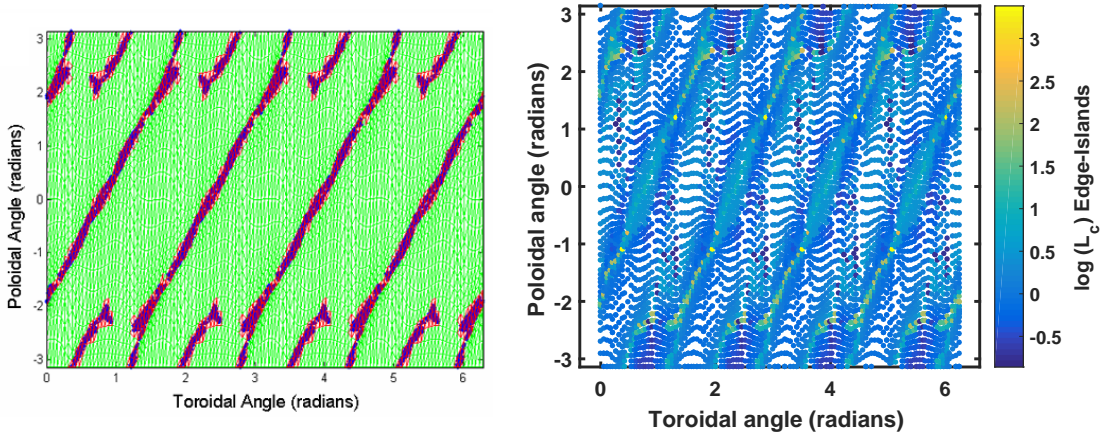
Figure 3.2 (L) J. Canik's strike point input to DEGAS as a plot of toroidal versus poloidal angle [56]. Wall triangles are designated as either sourcing (red) or non-sourcing (green). (R) New strike point input to DEGAS as a function of toroidal versus poloidal angle. Each triangle's source rate is linearly proportional to the wall-to-wall connection length of the field lines borne from the triangle, represented by the color of the point. Points are displayed on a log scale for visual clarity. Connection length calculations used for (R) plot courtesy of A. Bader.

yield a total source rate. A comparison of the old method and the new method is shown in Fig. 3.2. Connection lengths are plotted on a log scale to make the difference clearer to the human eye. In this work, this will be referred to as the new strike-point definition.

3.3.2 Improved scaling of DEGAS calculations

The DEGAS calculation is inherently very flexible. It is currently run for HSX as a linear combination of two calculations. The first calculation includes only particles sourced from a point source, which is meant to simulate the gas fueling produced by the piezo valve. The second calculation includes only particles sourced from wall recycling at strike-point locations as described in

the previous section (i.e. wall triangles which are intersected by edge field lines). These two calculations are then individually scaled and added to produce the final DEGAS results. This scaling is expressed as:

$$H_{\alpha,\text{tot}} = \beta H_{\alpha,\text{point}} + \gamma H_{\alpha,\text{strike}} \qquad (3.1)$$

where β is the factor that matches the point-source measured H_α to the DEGAS predicted H_α and γ is the factor that matches the strike-point measured H_α to the DEGAS predicted H_α. Together, these scale factors are used to determine the absolute wall-particle source strength, or the number of particles released by the HSX wall per second. The synthetic H_α emission is calculated at each point in the computational grid and then, according to the viewing geometry of the filtered photodiode detectors (see Fig. 3.4), integrated along their respective lines of sight. This integration yields a quantity that can be compared to experimentally measured values.

The validity of this scaling procedure requires that the DEGAS predicted H_α emission is as accurate and noise-free as possible. Obtaining good statistics for H_α emission near the point source is not an issue due to the locally high neutral density (both atomic and molecular hydrogen). However, in the strike-point fueling case, the local density of neutral particles is substantially lower and the calculation needs to be run longer (i.e. more test-flights are necessary) to reduce Monte-Carlo noise in the predicted H_α.

In this work, a factor of 20 more test flights were run for the strike-point fueling case in order to produce better synthetic H_α (50k vs. 1M). This improvement is shown in Fig. 3.3. However, running this calculation even longer would be desirable to further reduce Monte-Carlo noise, but the calculation becomes prohibitively expensive.

The procedure to obtain β and the scaled DEGAS calculation for the point source case is effectively the same as that reported in previous work [57]. The six channels in the C-poloidal array (see Fig. 2.7) are used to scale the point-source calculation. These channels are used because
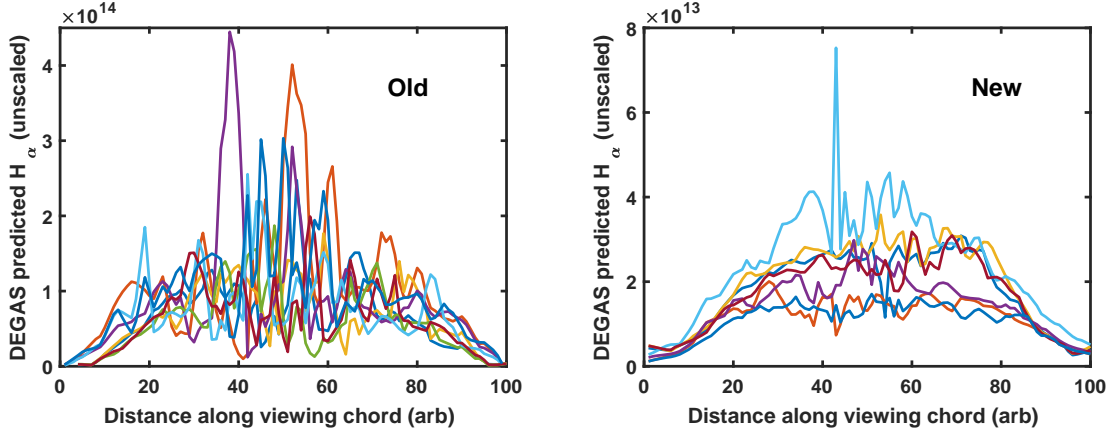
Figure 3.3 Figure demonstrating how increasing the number of particles in DEGAS improves statistics. The different colored lines represent the H_α along each viewing chord corresponding to a measurement location. (L) DEGAS predicted H_α emission along toroidal array line of sight for 50k test-flights. (R) DEGAS predicted H_α emission along toroidal array line of sight for 1M test-flights. The absolute differences in unscaled emission are irrelevant and will be removed when the DEGAS calculation is scaled.

they are in very close proximity to the piezo gas valve in the experiment. In this case, β is defined as:

$$\beta = \frac{\frac{1}{6}\sum_{i=1}^{6} H_{\alpha,\text{C measured},i}}{\frac{1}{9}\sum_{i=1}^{9} H_{\alpha,\text{C DEGAS},i}} \tag{3.2}$$

where $H_{\alpha,\text{C measured}}$ is the line-integrated H_α measurement from the 6 measurement channels in C and $H_{\alpha,\text{C DEGAS}}$ is the DEGAS-predicted integrated H_α emission from the 9 lines of sight (6 of which are identical to the measurement locations).

However, the procedure to obtain the scaled DEGAS calculation for the strike-points has changed as a result of the new H_α detectors installed on HSX during this work. A new poloidal array of seven H_α detectors was installed in field period A-prime (see Fig. 2.7). A CAD sketch of this array is shown in Fig. 3.4. Unlike the poloidal H_α array in field period C, the emission measured by the array in A-prime is not dominated by the gas-puff emission and can therefore be used to provide a line-integrated profile of the strike-point H_α emission. (Both DEGAS and EMC3-EIRENE predict that a strike-point exists near channel 1 in Fig. 3.4.) The mean of the H_α
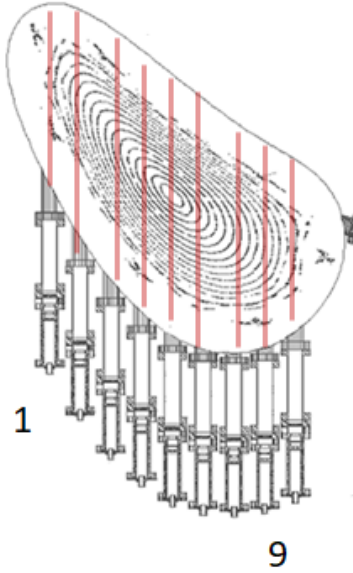
Figure 3.4 Cartoon illustrating the new H_α detector A-prime array. The channel numbers on this array correspond to the numbering on Fig. 3.5. The line-of-sight for each detector is shown with a transparent red line.

line-integrated emission measured by each channel is determined, and the mean of the DEGAS-predicted H_α emission of each line of sight is determined as expressed below. In this case, γ is defined as:

$$\gamma = \frac{\frac{1}{7}\sum_{i=1}^{7} H_{\alpha,\text{A-prime measured},i}}{\frac{1}{9}\sum_{i=1}^{9} H_{\alpha,\text{A-prime DEGAS},i}} \tag{3.3}$$

where $H_{\alpha,\text{A-prime measured}}$ is the line-integrated H_α measurement from the 7 measurement channels in A-prime and $H_{\alpha,\text{A-prime DEGAS}}$ is the DEGAS-predicted integrated H_α emission from the 9 lines of sight (7 of which are identical to the measurement locations). The value that matches the DEGAS calculations to the experimental measurements is the scale factor, γ. It should be noted that this method to determine the scale factor weighs the contribution from all channels equally (i.e. by using the mean). This equal-weighting method was chosen because it was straightforward. However, weighting Channel 1 (the strike-point viewing channel) more heavily could be investigated in future work, along with any other number of weighting schemes.

The differences in the DEGAS-predicted H_α profiles and the experimentally measured H_α profiles, particularly those measured by the A-prime array, should be discussed. DEGAS predicts the highest H_α line-integrated emission near the strike point in the highest curvature region of the poloidal cut (channel 1 on Fig. 3.4). However, the experimentally measured H_α profiles show that channel 5, which traverses the magnetic axis, measured the highest H_α line-integrated emission. This disagreement could stem from a difference in edge temperatures, which would impact the H_α emission rate since it depends strongly on plasma temperature. This disagreement could also stem from the inability of DEGAS to capture the true magnetic geometry of the HSX edge, and also its inability to simulate plasma transport. To further investigate the source of this disagreement, EMC3-EIRENE calculations could be post-processed to yield H_α emission in HSX, which could be compared to experimental measurements as future work.

The ability to match the mean of each profile, rather than a single point, results in a more reliable calculation of scale factor, as is demonstrated in Fig. 3.5. Prior to the installation of the new A-prime array (see Fig. 2.7), only the central channel (channel 5) of this array was present. The best scaling method then was to match the toroidal array, which was comprised of stellarator-symmetric views through the magnetic axis (channel 5 in each field period), to the DEGAS predicted H_α emission. This was the procedure used by J. Canik. However, as shown in Fig. 3.5, matching only the central channel to the DEGAS predicted H_α emission most likely results in an artificially high scale factor, which in turn results in an artificially high neutral density (compare the y-axis in Fig. 3.5). The additional detectors now installed in A-prime allow the DEGAS calculation to be scaled with more information, resulting in a lower neutral density than that which was previously published [56, 57].

All of the changes mentioned above (i.e. substantially more particles and reduced Monte-Carlo noise, an improved scaling procedure using new detectors, and a more physically realistic wall source) result in a more accurate calculation of the HSX neutral density. Compared to previous
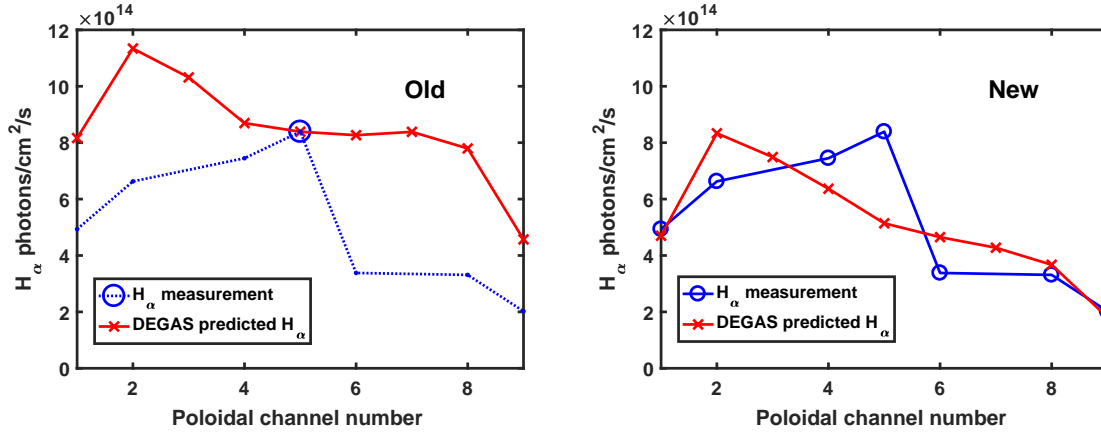
Figure 3.5 Figure demonstrating the old and new strike-point scaling procedures in DEGAS. (L) Plot demonstrating the old scaling procedure. DEGAS calculation run with old strike-point definition (red), scaled to toroidal array measurement (blue circle) Blue dotted line shows data from the new A-prime array to demonstrate that this scaling most likely overestimated the final neutral density. (R) Plot demonstrating the new scaling procedure. DEGAS calculation run with new strike-point definition (red), scaled to mean of A-prime array (blue solid line).

work, using values at the LCFS, the new values of neutral density are approximately a factor of 2 lower for atomic hydrogen and a factor of 13 lower for molecular hydrogen. Note that the long penetration length of atomic hydrogen particles due to both charge-exchange and also to molecular dissociation is consistent between the two calculations. The previous values in J. Canik's thesis are shown for comparison next to the updated values in Fig. 3.6. It should be noted that these updated values of HSX neutral density are in reasonable agreement (within 20 percent) with that predicted by EMC3-EIRENE [60].

3.4 The EMC3-EIRENE coupled codes

EMC3-EIRENE [61] is a more powerful calculation containing more physics than DEGAS. Specifically, it includes full information about the magnetic topology, and self-consistently calculates the edge temperature and density. It is actually a suite of coupled codes: EMC3 solves a simplified version of the Braginskii plasma fluid equations to iteratively advance the plasma to
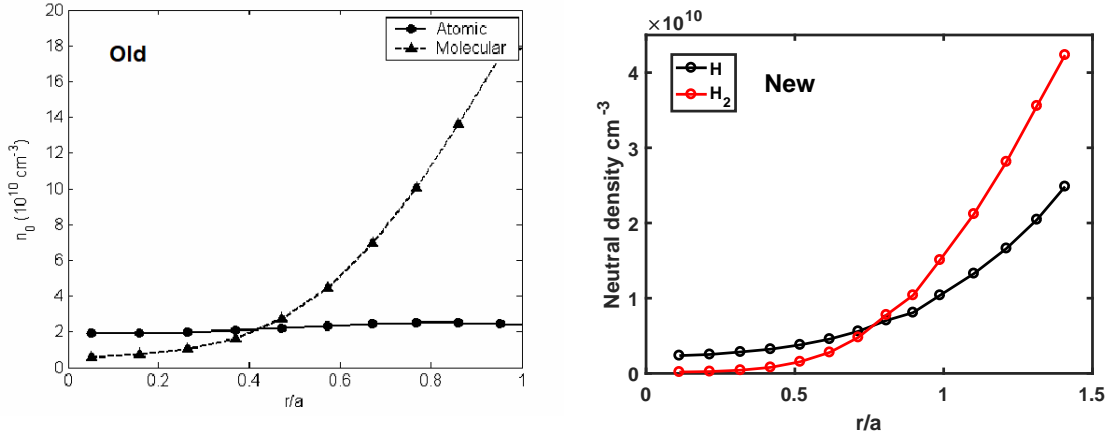
Figure 3.6 (L) Plot reproduced from [56]. (R) New values of neutral density calculated in this study using improved methods detailed above.

reach a converged, steady-state solution. EIRENE is a neutral Monte-Carlo code (similar to DE-GAS) which is used to calculate the reaction rates of various atomic processes at each iteration. Atomic processes included in EIRENE are shown in Table 3.1. EMC3-EIRENE is considered the current state of the art in 3D edge physics and is applied to stellarators, RMP tokamaks, and other devices in which 3-D physics is important.

EMC3-EIRENE is a suite of two coupled codes. EMC3 and EIRENE operate on two different grids; EIRENE has additional cells in the vacuum and core plasma regions, as well as a finer resolution in the toroidal direction. Fig. 3.7 is a reproduction from [62] that demonstrates one example of how these grids are related. The EIRENE grid is typically larger and can extend radially further in than the EMC3 grid. The EMC3 grid is typically smaller and extends in the region in which the plasma fluid approximations (described below) are valid. The inner simulation boundary is shown with a dark blue line. After each iteration, the information is collected and passed to the other code, which allows the plasma transport to be self-consistently calculated.

The Braginskii equations solved by EMC3 are shown below, where Equation 3.4 is the conservation of mass, Equation 3.5 is the conservation of momentum along the field line (in the $\vec{b}$ direction), Equation 3.6 is the conservation of of energy for the electrons, and Equation 3.7 is the
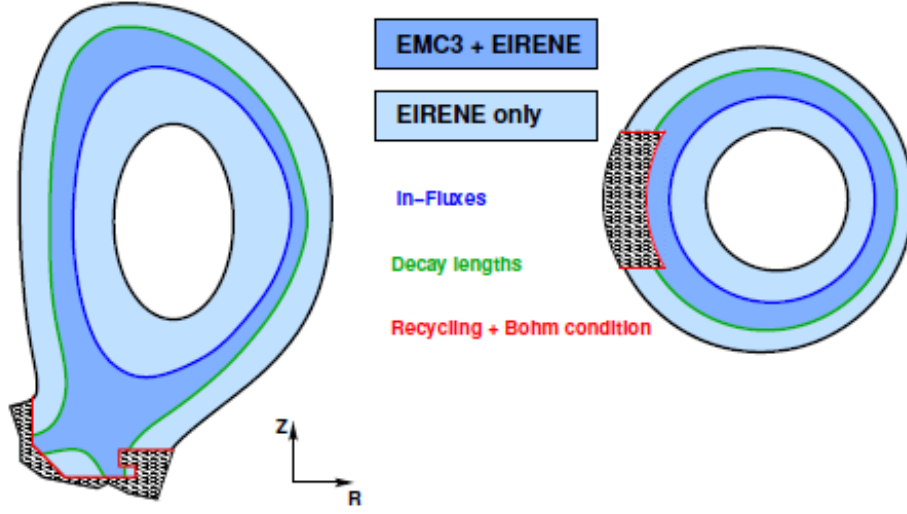
Figure 3.7 Figure demonstrating the differing computational domains for EMC3 and EIRENE in a diverted tokamak (L) and a limited tokamak (right). The EIRENE domain is typially larger and extends radially further in (shown in light blue) than the EMC3 domain. Figure reproduced from [62].

conservation of energy for the ions.

$$\nabla \cdot (n_i v_{i\|}\vec{b} - D_i \vec{b}_\perp \vec{b}_\perp \cdot \nabla n_i) = S_p \tag{3.4}$$

$$\nabla \cdot (m_i n_i V_{i\|}\vec{b} - \eta_\| \vec{b}\vec{b} \cdot \nabla V_{i\|} - \mu_\perp \vec{b}\vec{b} \cdot \nabla m_i n_i V_{i\|}) = -\vec{b} \cdot \nabla p + S_m \tag{3.5}$$

$$\nabla \cdot (\frac{5}{2}n_e T_e V_{i\|}\vec{b} - \kappa_e \vec{b}\vec{b} \cdot \nabla T_e) - \frac{5}{2}T_e D_i \vec{b}_\perp \vec{b}_\perp \cdot \nabla n_e - \chi_e n_e \vec{b}_\perp \vec{b}_\perp \cdot \nabla T_e) = -k(T_e - T_i) + S_{ee} \tag{3.6}$$

$$\nabla \cdot (\frac{5}{2}n_i T_i V_{i\|}\vec{b} - \kappa_i \vec{b}\vec{b} \cdot \nabla T_i - \frac{5}{2}T_i D_i \vec{b}_\perp \vec{b}_\perp \cdot \nabla n_i - \chi_i n_i \vec{b}_\perp \vec{b}_\perp \cdot \nabla T_i) = +k(T_e - T_i) + S_{ei} \tag{3.7}$$

where $\vec{b}_\perp$ is the direction perpendicular to the field line, n_e and n_i are the electron and ion density (and $n_e = n_i$), respectively, $V_{i\|}$ is the parallel ion velocity, D_i is the cross-field ion diffusivity, χ_e

and χ_i are the cross-field thermal diffusivities for the electrons and ions, respectively, T_e and T_i are the electron and ion temperatures, respectively, S_p is the plasma ionization source from neutrals, S_m is the plasma momentum sink from neutrals, S_{ee} is the electron energy from neutrals and any loss from impurity radiation, S_{ei} is the ion energy from neutrals, $\mu_\perp$ is the perpendicular viscosity ($\mu_\perp = mnD_\perp$), $\eta_\parallel$ is the parallel Braginskii viscosity, $k = 3n_e\nu_e m_e/m_i$, and k_e and k_i are taken from classical transport theory by Braginskii [63, 61, 64]. It is through the iterative solution of this simplified Braginskii model that plasma transport physics can be self-consistently simulated.

EMC3-EIRENE is fully three-dimensional with a computational grid that is based upon the magnetic field structure. User defined values of particle diffusivity, $D_\perp$ and thermal diffusivity, $\chi_\perp$, are used as a closure for the fluid equations. One assumption in EMC3-EIRENE is that the plasma is well-described by a fluid model. However, it is an open question as to whether these assumptions are satisfied in a low-density edge (like that of HSX) that may not be sufficiently collisional to warrant the fluid approximation. It is important to keep in mind the relative strengths and weaknesses of all the numerical calculations we present.

Despite this, EMC3-EIRENE has several major advantages over DEGAS. Most importantly, DEGAS is only a neutral particle code and does not include fluid plasma physics or the ability to simulate plasma transport. EMC3 however does have these capabilities, which when coupled to EIRENE, can simulate both plasma and neutral physics. Secondly, although grid geometry limitations prevent DEGAS from simulating the complex HSX edge magnetic geometry (i.e. the 8/7 island chain), EMC3-EIRENE has no difficultly representing the edge magnetic structure, a key part of this entire body of work. Third, in DEGAS, the wall recycling location must be specified, which has been determined from both field line tracing and target-to-target connection length. In EMC3-EIRENE, no a priori assumptions are necessary about the location of strike-points; this is determined naturally from the geometry of the magnetic field and plasma transport physics. Finally, whereas in DEGAS the recycling source strengths are specified manually, in EMC3-EIRENE

the inner simulation boundary (see Fig. 3.7) plasma density is specified and the recycling flux is scaled accordingly to achieve this value at the inner boundary. For these reason, EMC3-EIRENE will be used more heavily than DEGAS in this work, including for the calculation of several important numerical quantities which will be described in the following sections. (It should be noted that for HSX, DEGAS values of neutral density are in reasonable agreement (within 20 percent) with those predicted by EMC3-EIRENE [60]).

3.5 EMC3-EIRENE fueling efficiency

As discussed in Chapter 2, a key quantity in the particle balance analysis is the fueling efficiency, f_{eff}, described in Equation 2.3. However, making this measurement is experimentally challenging. There is no direct measurement of the neutral particle profile available at either HSX nor W7-X, and hence the neutral/ion ratio across the radius has to be reconstructed using proxy quantities like the Balmer-α emission combined with plasma density and temperature profiles, which may or may not be known.

Another way to obtain the quantity f_{eff} is to use experimental measurements to inform an appropriate model which can then calculate neutral particle physics. Because it can self-consistently calculate these edge quantities in a complex 3-D geometry, EMC3-EIRENE is an appropriate tool for this calculation. It was applied for both HSX and W7-X configurations to obtain a plasma solution matching the available Thomson profile data as closely as possible. These solutions were then used to determine f_{eff}.

For HSX simulations, only wall-sourced neutral particles were included in the EMC3-EIRENE simulation (i.e. no gas injection was simulated) and for the W7-X simulations, only limiter-sourced particles were included in the EMC3-EIRENE simulation (i.e. no wall-sourced particles were simulated), because these were expected to be the dominant particle source in each respective device. The fueling efficiency was then determined by separating the grid into regions of open and closed

field lines [65] based on a user-supplied value of threshold L_c. In general only the value of f_{eff} for the plasma confinement region was considered because this quantity was being used for a single-reservoir particle balance, as described in Chapter 2.

The uncertainty in the threshold connection length choice was calculated by examining a range of physically reasonable L_c thresholds for both HSX and W7-X to divide the grid into regions of open and closed field lines. The resulting value of f_{eff} was calculated for a constant, experimentally relevant simulation value where all parameters except the choice of threshold L_c were kept constant. The results are shown in Figs. 3.8 and 3.9. In HSX, the change in f_{eff} between the range of 100-1000 m was ~ 4.5 percent in the Edge-Islands configuration and 6.6 percent in the No-Edge-Islands configuration. In W7-X, the change in f_{eff} between the range of 100-1000 m in the Standard configuration was ~ 2 percent and between the range of 100-10000 m in the Increased Iota configuration was ~ 3 percent. These values of uncertainty are carried through in the final determination of the error in $\tau_{p,H}$. These error bars will be displayed on the fueling efficiency calculations displayed in Chapters 4 and 5.

These values of f_{eff} extracted from EMC3-EIRENE modeling results were used to close the particle balance and obtain τ_p values, the final piece necessary to compute the particle balance. Details of these procedures for both HSX and W7-X will be described in Chapters 4 and 5.

3.6 Summary

In this chapter we have discussed two important numerical models which will play a key role in this work, DEGAS and EMC3-EIRENE. DEGAS will be used to help develop an HSX particle balance and EMC3-EIRENE will be used to calculate fueling efficiency for both HSX and W7-X. It is hard to overstate the importance of these tools: without them the analysis presented in the following chapters would not be possible.
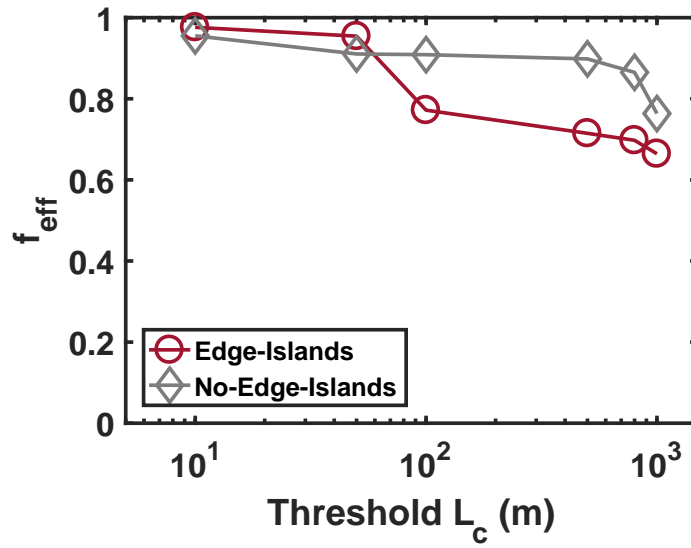
Figure 3.8 Plot demonstrating how the error in the HSX fueling efficiency coefficients were determined. The fueling efficiency calculated for a range of threshold connection lengths is plotted. The range between 100-1000 m is considered reasonable for HSX. EMC3-EIRENE calculations courtesy of A. Bader.
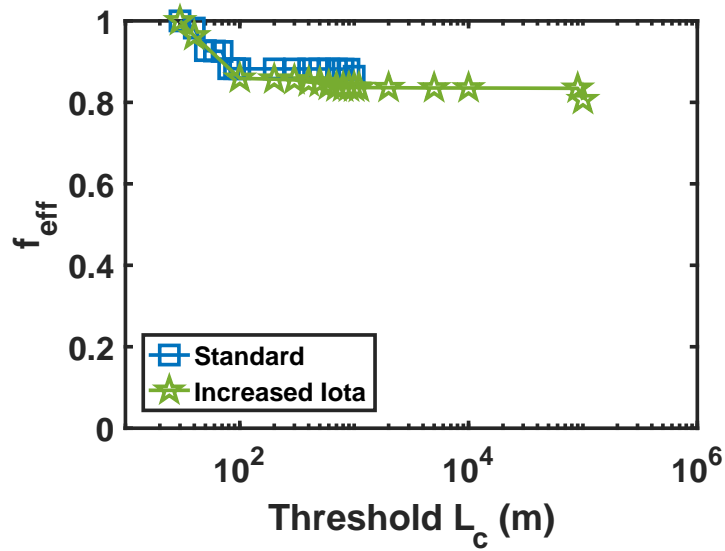
Figure 3.9 Plot demonstrating how the error in the W7-X fueling efficiency coefficients were determined. The fueling efficiency calculated for a range of threshold connection lengths is plotted. The range between 100-1000 m is considered reasonable for the W7-X standard configuration, and the range between 100-10000 m is considered reasonable for the Increased Iota configuration (the longer L_c values stem from the 5/5 edge islands). EMC3-EIRENE calculations courtesy of F. Effenberg.

References

29. Briesemeister, A. R. *Measurement and modeling of the flows and radial electric field in the HSX stellarator* bibtex: Briesemeister. PhD thesis (University of Wisconsin-Madison, 2013).

56. Canik, J. M., Anderson, D. T., Anderson, F. S. B., Likin, K. M., Talmadge, J. N. & Zhai, K. Experimental Demonstration of Improved Neoclassical Transport with Quasihelical Symmetry. *Physical Review Letters* **98.** ISSN: 0031-9007, 1079-7114. http://link.aps.org/doi/10.1103/PhysRevLett.98.085002 (2016) (23rd Feb. 2007).

57. Canik, J. M. *Experimental verification of reduced particle and electron heat transport with Quasisymmetry in the HSX stellarator* PhD thesis (Univeristy of Wisconsin - Madison, 2007).

58. Heifetz, D., Post, D., Petravic, M., Weisheit, J. & Bateman, G. A Monte-Carlo model of neutral-particle transport in diverted plasmas. *Journal of Computational Physics* **46,** 309–327 (1982).

59. Frerichs, H., Reiter, D., Schmitz, O., Evans, T. & Feng, Y. Three-dimensional edge transport simulations for DIII-D plasmas with resonant magnetic perturbations. *Nuclear Fusion* **50,** 034004. ISSN: 0029-5515, 1741-4326 (Mar. 2010).

60. Stephey, L. *Neutral source and particle balance in the stellarator edge* Preliminary Exam. 2015.

61. Feng, Y., Sardei, F., Kisslinger, J., Grigull, P., McCormick, K. & Reiter, D. 3D edge modeling and island divertor physics. *Contributions to Plasma Physics* **44,** 57–69. ISSN: 1521-3986 (2004).

62. Frerichs, H. *Three-dimensional plasma transport in open chaotic magnetic fields: A computational assessment for tokamak edge layers* PhD thesis (RWTH Aachen University, 2010).

63. Bader, A., Anderson, D., Hegna, C., Feng, Y., Lore, J. & Talmadge, J. Simulations of edge configurations in quasi-helically symmetric geometry using EMC3–EIRENE. *Nuclear Fusion* **53,** 113036. ISSN: 0029-5515, 1741-4326 (1st Nov. 2013).

64. Frerichs, H., Clever, M., Feng, Y., Lehnen, M., Reiter, D. & Schmitz, O. Numerical analysis of particle recycling in the TEXTOR helical divertor. *Nuclear Fusion* **52,** 023001. ISSN: 0029-5515 (2012).

65. Waters, I., Frerichs, H., Akers, R., Feng, Y., Flesch, K., Kirk, A., Ryan, D., Schmitz, O. & Thornton, A. *Plasma Response, Density Control, and Neutral Fueling: EMC3-EIRENE Analysis of the Edge Plasmas at MAST* in. 19th International Spherical Tokamak Workshop, Contributed Oral (2017).

Chapter 4

Particle penetration and confinement in HSX

4.1   Introduction

In this chapter, we will describe in detail the experimental measurements and techniques used to study particle behavior in HSX. In general we will follow the same format in Chapter 5. We will first describe our measurements of τ_p^*, followed by our measurements necessary for a full particle balance in HSX to determine $\tau_{p,H}$, followed by our calculation of the global recycling coefficient R. Finally we will discuss the EMC3-EIRENE modeling that has been completed for both the Edge-Islands and No-Edge-Islands configurations.

A brief summary of the results in this chapter are as follows: in the Edge-Islands configuration, longer values of $\tau_{p,H}^*$ and $\tau_{p,\text{He-II}}^*$ were measured by a factor of 1.5 and 1.6, respectively, compared to the No-Edge-Islands configuration. These results indicate that to some degree, helium transport was impacted by the change in edge configuration, although a full helium particle balance would be required to say definitively how much. After performing a full hydrogen particle balance, the value of $\tau_{p,H}$ was found to be a factor of 1.3 longer in Edge-Islands configuration. Furthermore, it was discovered that different scalings of $\tau_{p,H}$ with plasma density were present in the Edge-Islands (positive scaling) and No-Edge-Islands (negative scaling) configurations. Using our measurements of $\tau_{p,H}^*$ and $\tau_{p,H}$, we obtained a global hydrogen recycling coefficient value of approximately 0.8 in both configurations. The EMC3-EIRENE calculated fueling efficiency in the Edge-Islands configuration was 0.70 and in the No-Edge-Islands configuration was 0.87, a factor of 1.2 increase. We
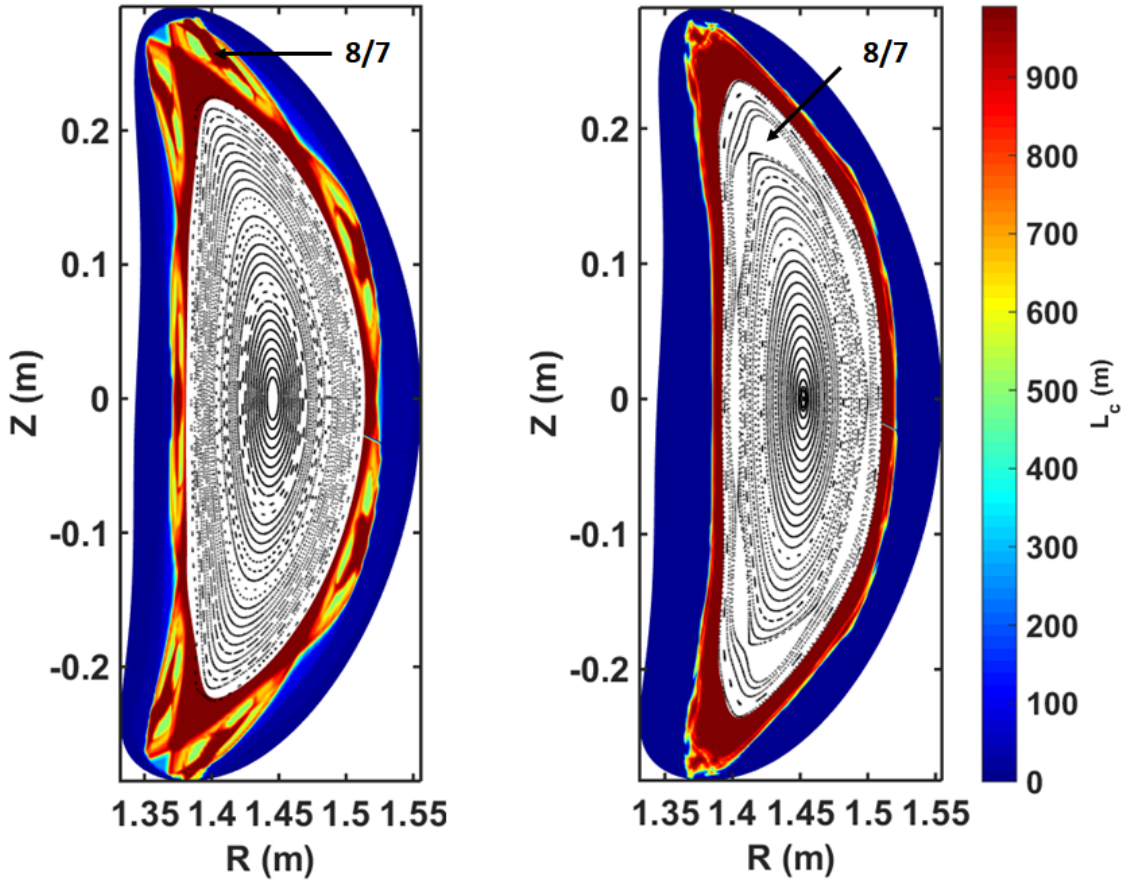
Figure 4.1 Figure representing the two magnetic configurations studied at HSX in this work. Colored regions denote the edge magnetic L_c of each configuration (scale shown on the colorbar of both plots). Black dots show the Poincaré plot of the surfaces inside the LCFS of each configuration. (L) The QHS configuration, referred to as the Edge-Islands configuration in this work. (R) The 5.5% Well configuration, referred to as the No-Edge-Islands configuration in this work. One can see that by raising the iota profile in the No-Edge-Islands configuration, the 8/7 island chain has been pushed several cm inside the LCFS. Results for these plots courtesy of A. Bader.

hypothesize that because these magnetic topology changes were made in the ionization source region, they were able to impact both particle penetration and particle confinement. The implications of these results will be discussed in more detail in Chapter 6.
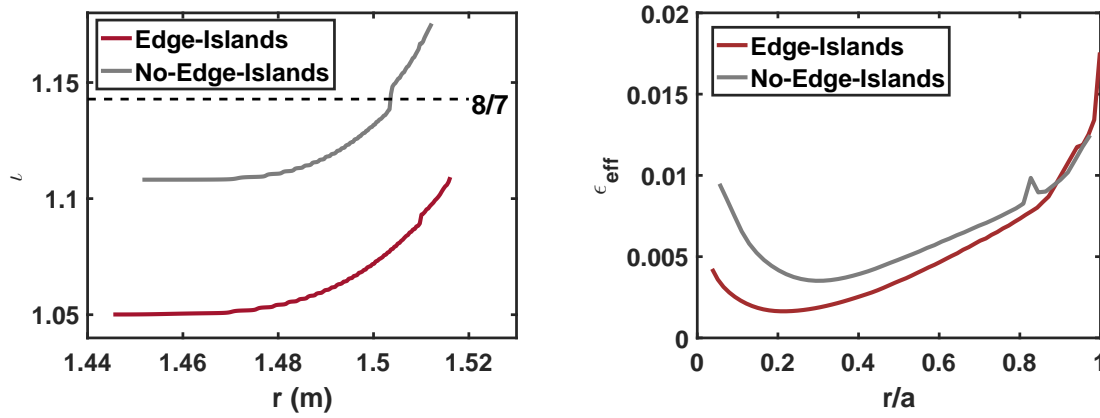
Figure 4.2 (L) Iota profile in both the Edge-Islands configuration (crimson line) and the No-Edge-Islands configuration (gray line), generated from calculations courtesy J. Schmitt. The 8/7 resonance is shown (black dotted line) to illustrate how raising the iota profile shifted the island chain radially inward. (R) Effective ripple, ϵ_{eff}, in both the Edge-Islands configuration (crimson line) and the No-Edge-Islands (gray line) configuration, generated from calculations courtesy R. Wilcox.

4.2 Magnetic configurations examined at HSX

The two configurations studied at HSX are shown in Fig. 4.1. The Edge-Islands configuration is shown on the left and the No-Edge-Islands configuration is shown on the right. In both plots, the Poincaré plot for each configuration is shown with black dots, and the colored regions show the edge connection length structure computed by EMC3-EIRENE with the longest connection lengths shown in red. Note that at HSX no limiters were present. To create the No-Edge-Islands configuration, the iota profile was raised to move the 8/7 chain inside the LCFS. The No-Edge-Islands configuration has an effective ripple, ϵ_{eff}, approximately a factor of two greater than that in the Edge-Islands configuration. The iota profiles and ϵ_{eff} profiles for both configurations are shown in Fig. 4.2. This very modest change in effective ripple was intended to minimize any changes in core transport.

Fig. 4.3 shows Thomson scattering data from both magnetic configurations in HSX. Data from the Edge-Islands configuration are shown in red and data from the No-Edge-Islands configuration
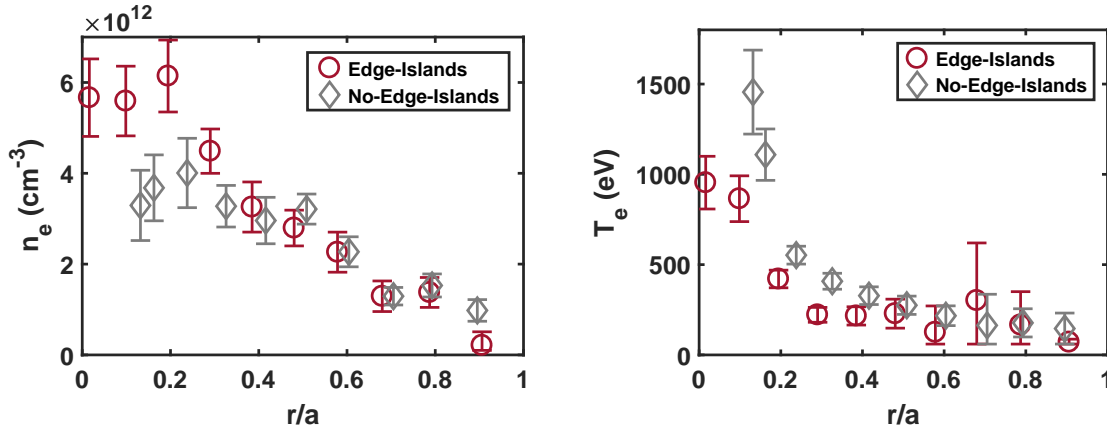
Figure 4.3 HSX Thomson scattering profiles from both the Edge-Islands (red circles) and the No-Edge-Islands (gray diamonds) configurations. (Left) Thomson n_e profiles and (Right) Thomson T_e profiles. These profiles were generated from data at two time points (t=0.83 and t=0.84 ms) and the error bars represent the sum in quadrature of the error from each individual measurement. Where appropriate, the error bars were constrained to lie within physically realistic values. The shift of the magnetic axis in the No-Edge-Islands configuration results in decreased core resolution.

are shown in gray. These Thomson data are determined from the mean of two time-points and the error bars represent the combined error of both individual time-points. The most marked difference between the two configurations appears inside of r/a=0. 2.

In addition to the Thomson measurements, we also examined the HSX inteferometer [38, 39] density inversion. This asymmetric Abel-inversion process uses the method outlined in [40]. Unfortunately due to a recent diagnostic issue, the interferometer inversion data collected for this work in the No-Edge-Islands configuration could not be used. However, older data for this configuration were available for a general comparison. These data are shown in Fig. 4.4. The Edge-Islands configuration data are shown in red. The No-Edge-Islands configuration data, collected in 2013, are shown in gray. These interferometer inversion data indicate that the density profiles are very similar between these two configurations. At this time the reason for the disagreement between the interferometer inversion and the Thomson scattering data is not known.
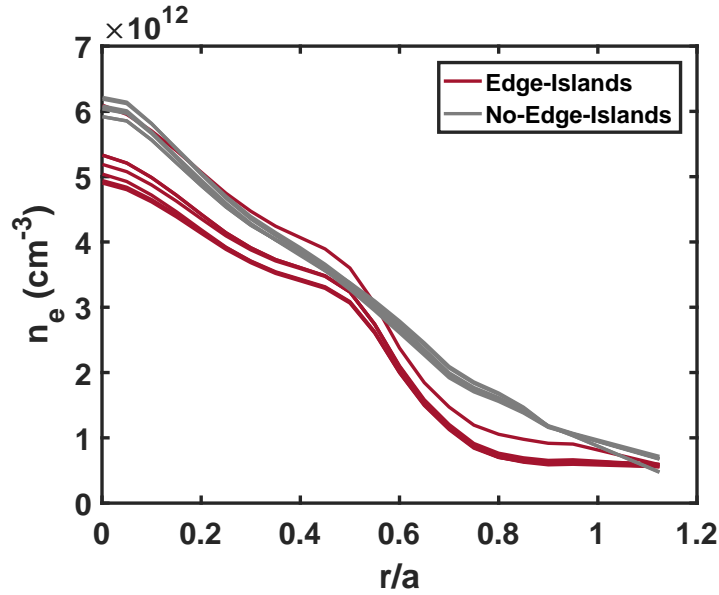
Figure 4.4 Density profile as a function of normalized minor radius determined from the HSX interferometer measurements using an Abel-inversion technique. Data in plotted in red are from the Edge-Islands configuration shots analyzed in this work. Data plotted in gray are from No-Edge-Islands configuration data taken in 2013 (more recent data were unavailable). Data courtesy C. Deng.

The overall message from both the Thomson scattering data and the interferometer inversion data is that the density profiles appear largely similar in the region outside the core which constitutes the large majority of the HSX plasma volume.

4.3 Effective confinement time in HSX

Measurements of $\tau_{p,H}^*$ and also of $\tau_{p,He}^*$, discussed below, were obtained by perturbative gas injection experiments. A short injection of the test gas species (H and He) was launched into an equilibrated hydrogen plasma. The reaction of the previously mentioned plasma parameters to these short injections were monitored. In particular, the exponential decay of the line-averaged density and the He-II emission after the termination of the gas injection was measured, fit to an
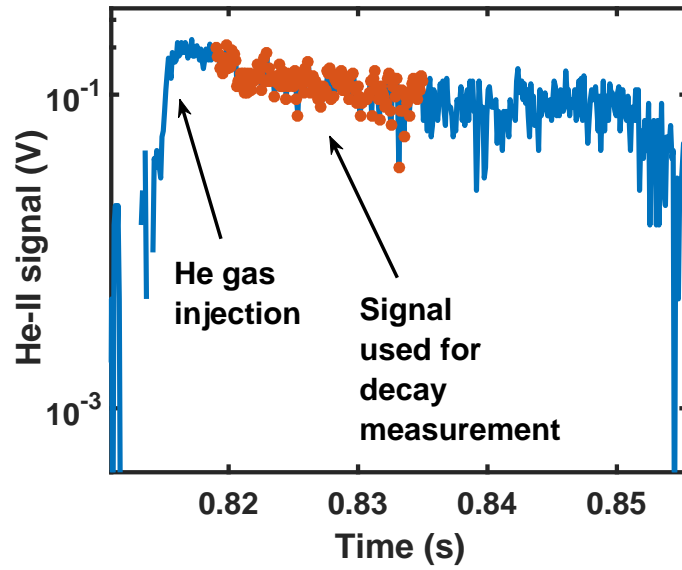
Figure 4.5 A representative He-II emission trace from HSX showing the helium gas injection into a hydrogen plasma at 0.81 s and the portion of the signal that was used to determine the exponential decay (highlighted in orange). Note that this trace was produced by subtracting a reference trace from a shot with no helium injection to remove the contribution of the residual HSX helium source.

exponential function, and the characteristic decay time was used to determine the effective confinement time τ_p^*.

At HSX, a fast valve was used to make a single 6 ms helium or hydrogen injection of $\sim 1 \times 10^{18}$ particles into a hydrogen plasma. A filtered photodiode array was used to measure decay in He-II emission (468.6 nm), and the HSX interferometer [39] was used to measure the decay in the line-averaged density for hydrogen injection. The H_α line emission was not used as the decay time was too fast for the photodiodes to resolve any meaningful differences. For both H and He injections, the signal from an immediately preceding or following reference discharge was subtracted from the signal obtained during the gas injection discharge. This allowed the contribution from the plasma or He-II background to be removed when determining the decay time. This subtraction was not possible with W7-X data, as will be discussed in Chapter 5 because no intermediate reference
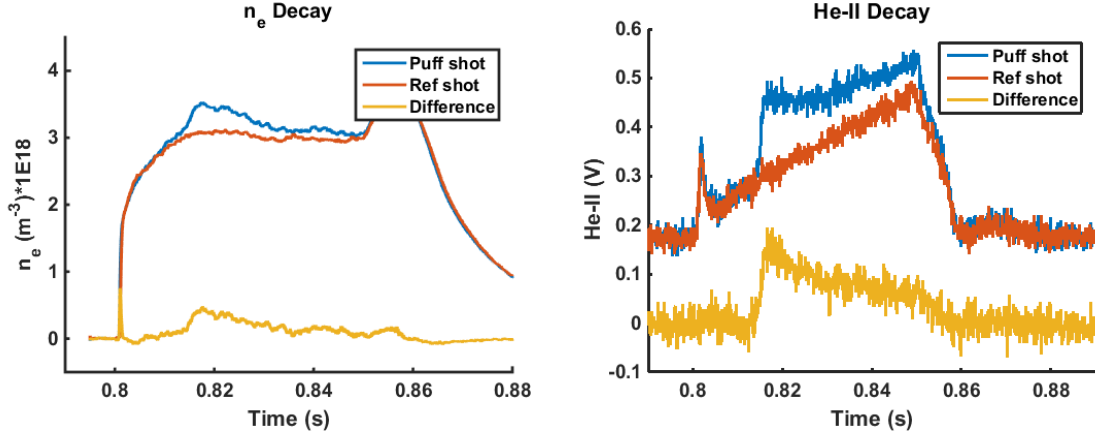
Figure 4.6 Figure demonstrating the process by which the effective confinement time for hydrogen (left) and helium (right) in HSX. The data shown for both hydrogen and helium are representative. Shown in blue, a perturbative gas puff of hydrogen or helium was injected into the HSX hydrogen background plasma. A steady-state reference shot, shown in red, was then subtracted from the perturbative puff shot. This subtraction process produced the yellow curves, which were ultimately used to fit an exponential function to determine the effective particle confinement time.

discharges were obtained. The subtraction procedure for a representative hydrogen and helium shot are shown in Fig. 4.6. Thus, for every measurement of τ_p^*, two plasma shots were required.

Measurements of $\tau_{p,\mathrm{H}}^*$ and $\tau_{p,\mathrm{He\text{-}II}}^*$ are shown in Fig. 4.7. The decay time is longer in the Edge-Islands configuration for both hydrogen and helium injections. In general, $\tau_{p,\mathrm{He\text{-}II}}^*$ is a factor of approximately 2 longer than $\tau_{p,\mathrm{H}}^*$, most likely due the fact that some fraction of hydrogen is absorbed by the wall for the short duration of HSX discharges while helium is fully recycling and hence re-fuels the plasma at a higher rate [9]. It should be noted that the error bars shown in Fig. 4.7 are the uncertainties in the 95 percent confidence exponential fit for each individual data point. The shaded region indicates the mean standard deviation of all the data points from the fit line. A single term power series fitting of the form $y = ax^b$ was used the generate a fit line, also plotted. This functional form was chosen so that it would be clear how the values of τ_p^* and ultimately τ_p depend on the mean line-averaged density.
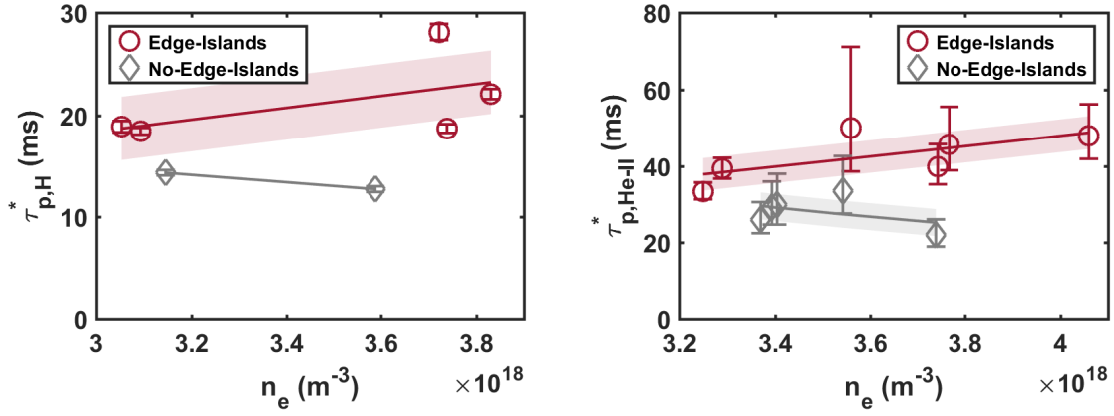
Figure 4.7 Figure showing τ_p^* measured in HSX in both the Edge-Island (red circles) and No-Edge-Island (gray diamonds) configurations. (Left) $\tau_{p,\mathrm{H}}^*$ as a function of n_e (Right) $\tau_{p,\mathrm{He\text{-}II}}^*$ as a function of n_e. Data are plotted as function of mean n_e determined from the central chord of the HSX interferometer. A single term power series fitting was used the generate a fit line, also plotted. The shaded region indicates the mean standard deviation of the measured data points from the fit line.

These measurements indicate that τ_p^* is longest in the Edge-Islands configuration for both hydrogen and helium injection. For clarity, we will discuss the results at a value of $n_e = 3.5 \times 10^{18}$ m^{-3}. At this density, the value of $\tau_{p,\mathrm{He\text{-}II}}^*$ is approximately a factor of 1.6 longer in the Edge-Islands configuration. Similarly, the value of $\tau_{p,H}^*$ is approximately a factor of 1.5 longer in the Edge-Islands configuration.

4.4 Particle balance in HSX

Now we turn our attention to the particle confinement time, τ_p. To determine this quantity, we will rely on many of the tools and measurements we have described thus far. All of these pieces will be used together to generate a particle accounting, also known as a particle balance. This single-reservoir balance is essentially a particles-in, particles-out model, which in turn allows us to calculate the particle system dwell time, τ_p. Despite the relative simplicity of the single

reservoir model, it has been shown to be a reasonable representation of particle behavior in several experiments including DIII-D [37], NSTX [36], JET [66], TEXTOR [35], and RFX [67]. A more detailed multi-reservoir model [68] could resolve differences in core and edge fueling and confinement properties, but this was beyond the scope of this work.

As discussed in Section 2.3, we will use experimental data to infer the particle balance in order to determine the global particle confinement time τ_p. Equation 4.1 shows a generic version of this balance.

$$\frac{dN_{\text{tot}}}{dt} =$$

$$-\frac{N_{\text{tot}}}{\tau_p} + f_{\text{gas}}\Phi_{\text{gas}} + f_{\text{wall}}\Phi_{\text{wall}} + f_{\text{lim}}\Phi_{\text{lim}} = \tag{4.1}$$

$$\Phi_{\text{ext}} - \Phi_{\text{exhaust}}$$

where N_{tot} is the total number of plasma particles, τ_p is the particle confinement time, f_{gas}, f_{wall}, and f_{lim} are fueling efficiency coefficients, and Φ_{gas}, Φ_{wall}, Φ_{lim} are particle fluxes from the gas valve, recycling from the main wall, recycling from the limiter and Φ_{ext} is the total external fueling, and Φ_{exhaust} is the exhaust rate.

For the case of HSX, several terms can be neglected. First, because no limiters are inserted for the experiments under consideration, the recycling term at the limiters is not included (i.e. $\Phi_{\text{lim}} = 0$). Second, it is important to note that measurements of the pumping capabilities of HSX indicate that the pumping speed is small relative to the plasma duration. As a consequence, the particle balance becomes a closed system without an external loss term. The only particle removal mechanism on the time scale of HSX discharges is if the recycling coefficient R is smaller than one, as then particles will be removed from the particle balance and are not available anymore to replenish the particles contained in the plasma reservoir. The recycling coefficient can be obtained using the effective particle confinement time and the true particle confinement time, which will be discussed at the end of this section. Based on these assumptions, the following formulation

for the HSX particle balance is used for the analysis presented:

$$\tau_p = \frac{N_{\text{tot}}}{-\frac{dN_{\text{tot}}}{dt} + f_{\text{gas}}\Phi_{\text{gas}} + f_{\text{wall}}\Phi_{\text{wall}}} \tag{4.2}$$

4.4.1 Total number of particles, N_{tot}

The total number of particles in the HSX confinement region is the most straightforward term of the particle balance to calculate. Using the chord of the HSX interferometer that intersects the magnetic axis of each configuration, the mean value line-averaged density is multiplied by the volume of the confinement region in each case. The analysis window during which the mean is determined is from 0.81 to 0.84 seconds. For more information about how this term is calculated, please see the discussion in 2.4.1.

We use the line-averaged density for several reasons. The first is that the Thomson scattering data are only available for an ensemble of shots and therefore cannot be used to analyze each individual shot as we will do. As mentioned previously, the interferometer inversion data were not available for all of the No-Edge-Islands shots analyzed in this work, so density inversion profiles were also not an option. This leaves the line-averaged density, which because it samples the entire cross-section of the plasma, provides information about the global number of plasma particles. (We will use the same method at W7-X).

The configuration volumes V_{conf} were taken from S. Gerhardt's thesis [28] and are 0.378 m^3 in the Edge-Islands configuration and 0.356 m^3 in the No-Edge-Islands configuration. The errors given for these calculations are very small ($\sim$ 1 percent), so we assume that the largest source of error in this term is the standard deviation of the interferometer signal during the analysis window ($\sim$ 2-5 percent). Therefore we have:

$$N_{tot} = \bar{n}_e V_{conf} \tag{4.3}$$

and

$$\Delta N_{tot} = \Delta \bar{n}_e V_{conf} \tag{4.4}$$

4.4.2 Gas puff particle flux, Φ_{gas}

The HSX gas puff flux was determined through a calibration matrix (see Chapter 2). Given the voltage signal sent to the piezo electric gas valve and the backing pressure of the gas plenum, the total throughput in a 60 ms pulse could be calculated. (Fueling in HSX typically starts approximately 10 ms before ECRH initiation and continues through the 50 ms discharge.) Additionally, changes in the line-averaged density signal typically lag several ms behind changes in the gas puff input.

The principal source of error in this calibration is thought to come from the uncertainty of the HSX vacuum vessel volume, including boxports, pump ducts, and other internal components. To determine this total volume, as well as to quantify the error in this volume estimation, we employed the following procedure. Two volumes were considered: a gas plenum of known volume (V_1), and the HSX vacuum vessel of unknown volume (V_{HSX}). By first measuring the pressure in the plenum (P_1) and then quickly releasing the gas into the HSX vacuum vessel system and measuring the pressure of the two combined volumes (P_2), the volume of the unknown region could be determined using the ideal gas law [69], which was used to determine Equation 4.5.

$$V_{HSX} = \frac{P_1 V_1}{P_2} - V_1 \tag{4.5}$$

The total HSX vacuum vessel volume calculated with this method is 1.56 m^{-3}. The total estimated error from this method (which was performed several times) is approximately 4 percent. Therefore Φ_{gas} is calculated directly using the calibration table, and $\Delta\Phi_{gas}$ is 4 percent error. The program and data that were used to develop this calibration can be found in `Y:/Puff_calibration/find_hsx_volume.mat`.

4.4.3   Wall particle flux, Φ_{wall}

The HSX wall particle flux, Φ_{wall}, was by far the most complex term to obtain for the HSX particle balance. It was determined through a combination of experimental spectroscopic measurements and neutral particle modeling using the DEGAS code [58]. The process was as follows: an array of absolutely calibrated H_α detectors [55] was used to view the HSX plasma at a location toroidally far away from the gas puff to measure the intensity signal I_{H_α}. This signal was obtained as a voltage signal V_{H_α} from the photodiode and converted into an intensity signal I_{H_α} with units [photons s^{-1} cm^{-2}] using an absolute calibration factor c_{H_α}. Please see Chapter 3 for more detailed information about how Φ_{wall} is determined.

The DEGAS code, a 3-D Monte-Carlo neutral particle code, was used to simulate the wall-sourced neutral particles in HSX. Only the wall-sourced particles were simulated in an effort to isolate the contribution of the Φ_{wall} term to the particle balance. (For reference the gas puff flux Φ_{gas} is of the same order as Φ_{wall}.) The locations of the plasma sources were determined through field line following; the location at which the field line intersected the vessel wall was treated like a source. In addition, a linear relationship between the source rate and the field line connection length was assumed based on previous work [59]. The total source rate from the wall surface area is Φ_{wall}.

Given a static plasma background determined from the Thomson profiles shown in Fig. 4.3, the DEGAS code calculates the neutral particle density and the estimated H_α emission rate I_{H_α} in each volumetric grid cell. This calculated emission can then be directly compared to the measured H_α emission in a manner similar to that described in [26]. The scale factor, discussed in 3.3.2, required to match the DEGAS emission to the measured emission is then used to scale the wall particle source rate, which provides the final value of Φ_{wall} required for Equation 4.2. The advantage to using DEGAS for this portion of the study is that it includes a package which automatically
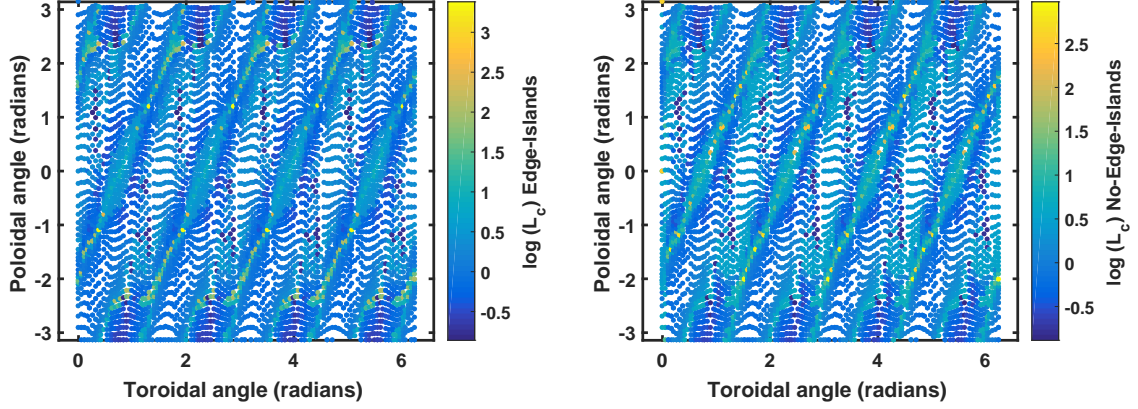
Figure 4.8 Plots showing the DEGAS wall source, on a log scale, as determined by assuming the source strength is linearly proportional to the connection length. (L) DEGAS wall-source for the Edge-Islands configuration. (R) DEGAS wall-source for the No-Edge-Islands configuration. Connection length calculations courtesy of A. Bader.

calculates the expected H_α emission given the neutral density and background plasma parameters, therefore facilitating comparisons with the absolutely calibrated H_α measurements obtained experimentally. With these quantities, the wall particle flux (and its associated standard deviation) was calculated as follows:

$$\Phi_{wall} = c_{H_\alpha} \alpha_{DEGAS} I_{H_\alpha} \tag{4.6}$$

$$\Delta\Phi_{wall} = \sqrt{(\Delta c_{H_\alpha})^2 + (\Delta\alpha_{DEGAS})^2 + (\Delta I_{H_\alpha})^2} \tag{4.7}$$

The uncertainty in Φ_{wall} consists of the uncertainty of the measured intensity signal ΔI_{H_α} and the uncertainty of the calibration quantities $\Delta c_{H\alpha}$ and $\Delta\alpha_{DEGAS}$. ΔI_{H_α} is obtained as the standard deviation $\sigma(I_{H_\alpha})$ of the I_{H_α} during the analysis window (a real measurement uncertainty), the calibration error of the H_α photon flux measurement (a systematic uncertainty), and the estimated uncertainty in the DEGAS calculation and scaling procedure $\Delta\alpha_{DEGAS}$, which is a systematic uncertainty assuming the variation in n_e and T_e is moderate during the analysis time window and
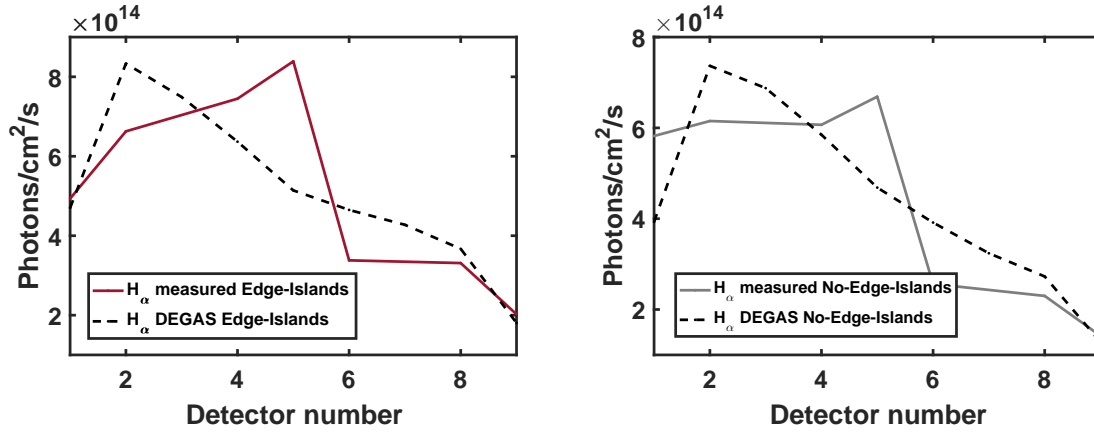
Figure 4.9 Figure showing both experimental H_α measurements in the Edge-Islands (L) and No-Edge-Islands (R) configurations (in crimson and gray, respectively), along with their scaled DEGAS H_α counterparts (black dotted lines). The H_α photon flux is plotted as a function of channel number.

in the discharges compared. This is expressed in Equation 4.7. The total error in the wall source term, determined from linear error propagation, is $\sim$ 20-25 percent, but of this total, only about 5% stems from real measurement uncertainties which do not cancel in relative comparisons.

The uncertainty $\Delta\alpha_{DEGAS}$ in the DEGAS scaling procedure is determined by running the DEGAS calculations three times for each magnetic configuration: the first was run using the background temperature and density shown in Fig. 4.3, the second was run using the values of temperature and density at the lower error bar, and the third was run using the temperature and density at the upper error bar for each configuration. These calculations can be seen in Fig. 4.10. The deviation in the final scale factor between these upper and lower limits of the background plasma is used to determine the uncertainty in the DEGAS calculation and the subsequent scale factor. This uncertainty is on the order of 16 percent. This uncertainty, however, again is a systematic uncertainty borne from the neutral model, and hence it will cancel out for relative comparisons.

Because the density and temperature profiles are similar in both shape and magnitude in the Edge-Islands configuration and the No-Edge-Islands configuration (see Fig. 4.3), the DEGAS simulation profiles, which were based on these measured Thomson profiles, are also similar. As a
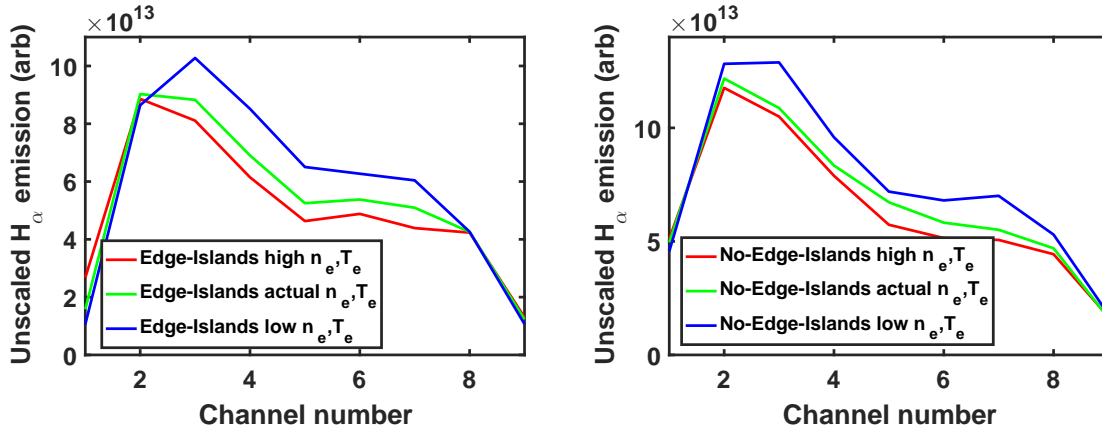
Figure 4.10 Suite of DEGAS calculations of predicted H_α emission to determine the estimated error in the DEGAS wall term. These data are plotted as function of channel number. All background temperature and density profiles in the DEGAS calculations were based on the Thomson profiles shown in Fig. 4.3. These DEGAS calculations were used to determine the H_α emission profiles for the upper error bar and lower error bar cases. Three cases were run for each configuration: the high density, high temperature case (shown in red), the low density, low temperature case (shown in blue), and the case based on the measured Thomson data points (shown in green). The relative difference between the high and low cases as a fraction of the measured case was the calculated error in the DEGAS simulation and scaling process (~ 16 percent).

result, the wall-source term Φ_{wall} does not strongly depend on the magnetic configuration, as can be seen in Fig. 4.11.

4.4.4   Particle confinement time, $\tau_{p,H}$

The final particle balance is analyzed with the aforementioned terms (i.e. N_{tot}, $\frac{dN_{tot}}{dt}$, Φ_{gas}, and Φ_{wall}) on a shot-by-shot basis. The terms that vary in Equation 4.2 (i.e. everything except the fueling efficiency coefficients) are all shown in Fig. 4.11 as a function of mean line-averaged density (calculated from the central channel during the analysis window). Data from the Edge-Islands configuration are shown with red circles and data from the No-Edge-Islands configuration are shown with gray diamonds. A single term power scaling was fit to the data and is shown with a solid line for each configuration. The mean standard deviation of the data from the fit line is shown

as a shaded region above and below the power law fit line. This overview of the particle balance shows that all terms are comparable, but the time rate change of the density evolution (Fig. 4.11(b)) as well as the gas fueling flux (Fig. 4.11(c)) are somewhat different for the no-edge islands case. However, the $\frac{dN_{tot}}{dt}$ term is roughly one order of magnitude smaller than the Φ_{gas} and Φ_{wall} terms, and therefore makes only a small contribution to the overall particle balance.

One important element of the analysis is only implicitly visible in Fig. 4.11: the fueling efficiency f_{wall} for the recycling and gas flux terms f_{gas}. They are inferred using comparative EMC3-EIRENE modeling as will be discussed in Section 4.6. This analysis of f_{eff} aided by EMC3-EIRENE shows a difference in the fueling efficiency of 20%. This difference in the fueling eventually leads to the significant difference in τ_p between both configurations shown in Fig. 4.11(e). The global particle confinement time τ_p is reduced by up to $25-30\%$ when the $m/n = 8/7$ island chain is moved into the plasma. The meaning of this reduction as well as the physics reason for the reduced fueling efficiency which defines this reduction is discussed in Section 4.6 in conjunction with the numerical analysis of the experiments with EMC3-EIRENE.

The uncertainty of all the component terms in Equation 4.2 are then added using linear error propagation to determine the total error for all individual measurements of τ_p. This uncertainty is $\sim$ 14-20 percent in the Edge-Islands configuration and $\sim$ 15-18 percent in the No-Edge-Islands configuration. These quantities can be seen in Fig. 4.11(e) calculated for each individual measurement. A single term power scale fitting was determined as a function of the plasma density. This fit and its parameters can be seen in Fig. 4.11(e).

The uncertainty in the particle confinement time is calculated according to Equation 4.8.

$$\Delta\tau_p = \sqrt{\begin{aligned}&(\frac{\partial\tau_p}{\partial N_{tot}})^2(\Delta N_{tot})^2 + (\frac{\partial\tau_p}{\partial dN_{tot}/dt})^2(\Delta dN_{tot}/dt)^2 + (\frac{\partial\tau_p}{\partial f_{gas}})^2(\Delta f_{gas})^2 \\ &+(\frac{\partial\tau_p}{\partial\Phi_{gas}})^2(\Delta\Phi_{gas})^2 + (\frac{\partial\tau_p}{\partial f_{wall}})^2(\Delta f_{wall})^2 + (\frac{\partial\tau_p}{\partial\Phi_{wall}})^2(\Delta\Phi_{wall})^2\end{aligned}} \tag{4.8}$$
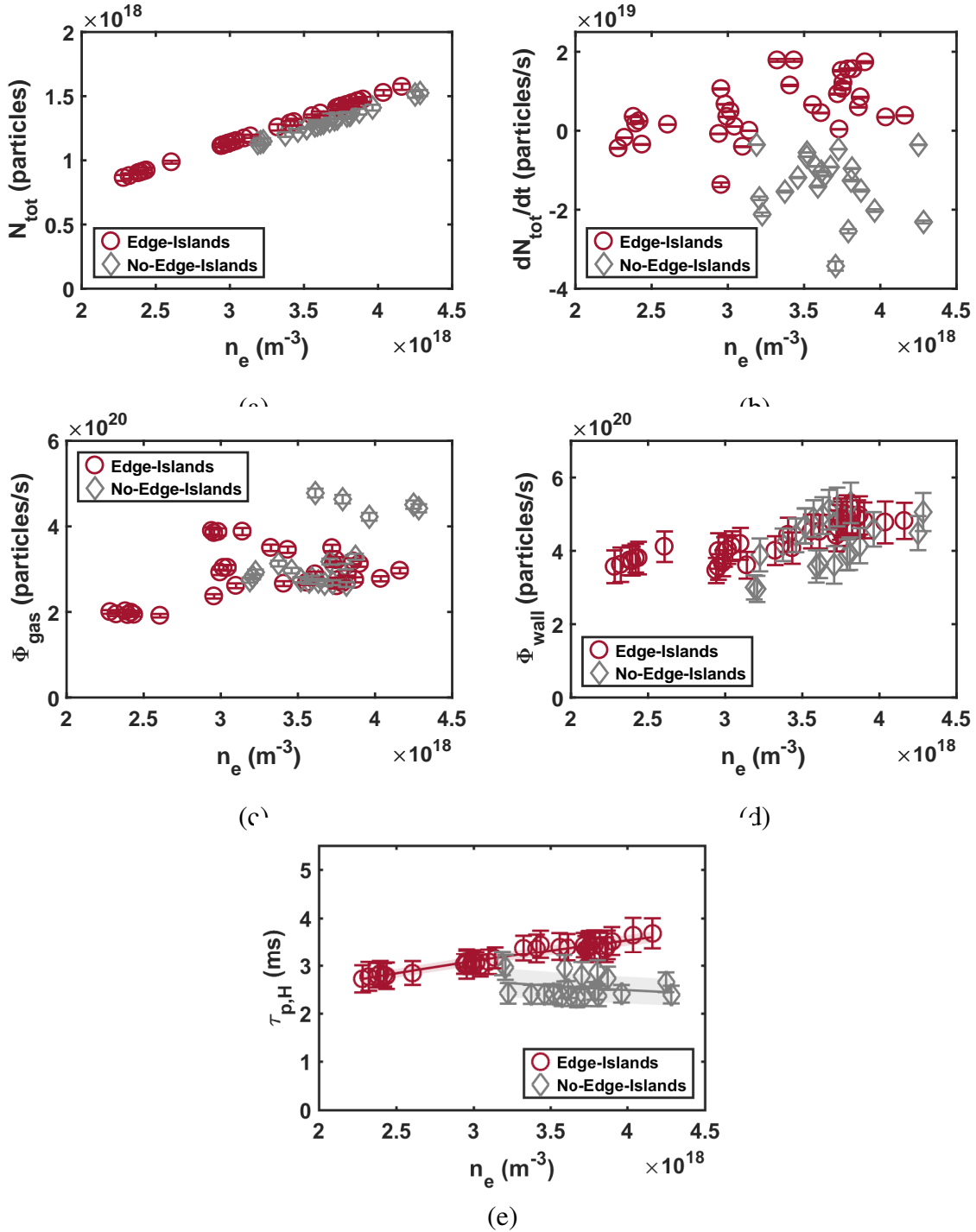
Figure 4.11 Terms in the particle balance analysis plotted as a function of mean line-averaged density measured by the HSX interferometer. Data from the Edge-Islands configuration are shown with red circles and data from the No-Edge-Islands configuration are shown with gray diamonds and gray squares. (a) Values of N_{tot}, (b) values of $\frac{dN_{tot}}{dt}$, (c) values of Φ_{gas}, (d) values of Φ_{wall}, (e) values of $\tau_{p,H}$. The lines in (e) are single term power function fit lines. The error bars represent the total individual error for each data point, and the shaded regions represent the mean standard deviation between the data points and the fit line.

There are several important pieces of information contained in Fig. 4.11(e). First, the values of $\tau_{p,H}$ in the Edge-Islands configuration are generally larger than those in the No-Edge-Islands configuration. At a value of $n_e = 3.6 \times 10^{18}$ m^{-3}, $\tau_{p,H}$ is a factor of 1.32 larger in the Edge-Islands configuration. Additionally, as we observed in the τ_p^* measurements, we find a similar trend in the behavior of $\tau_{p,H}$ as a function of the mean n_e: an increasing value of $\tau_{p,H}$ in the Edge-Islands configuration and a decreasing value of $\tau_{p,H}$ in the No-Edge-Islands configuration.

As mentioned above in the discussion of the τ_p^* results, these differing trends as a function of plasma density may imply different confinement physics in the Edge-Islands configuration and No-Edge-Islands configuration. We hypothesize that these differing trends are related to the relative ability of undesirable wall-sourced particles to penetrate into the confinement region, as we will discuss in greater detail in Chapter 6.

4.5   Global recycling coefficient in HSX

Now that we have determined both τ_p^* and τ_p for HSX, we can use the following relationship to determine R, the global recycling coefficient as prescribed in Equation 4.9[6]:

$$R = 1 - \frac{\tau_p}{\tau_p^*} \tag{4.9}$$

and the error in R through linear error propagation as prescribed in Equation 4.10

$$\Delta R = \sqrt{(\frac{\partial R}{\partial \tau_p^*})^2 (\Delta \tau_p^*)^2 + (\frac{\partial R}{\partial \tau_p})^2 (\Delta \tau_p)^2} \tag{4.10}$$

If we take the density scaling fits for $\tau_{p,H}$ and $\tau_{p,H}^*$ as a function of n_e, we can compute R over this same density range. These values, and their respective confidence regions (shown as shaded regions), are plotted in Fig. 4.12. The confidence regions shown are calculated according to Equation 4.10 and the partial derivative weighting factors contribute strongly to the small total standard deviation. The calculated values of R for the Edge-Islands configuration range from approximately 0.83-0.87, and the calculated values of R for the No-Edge-Islands configuration
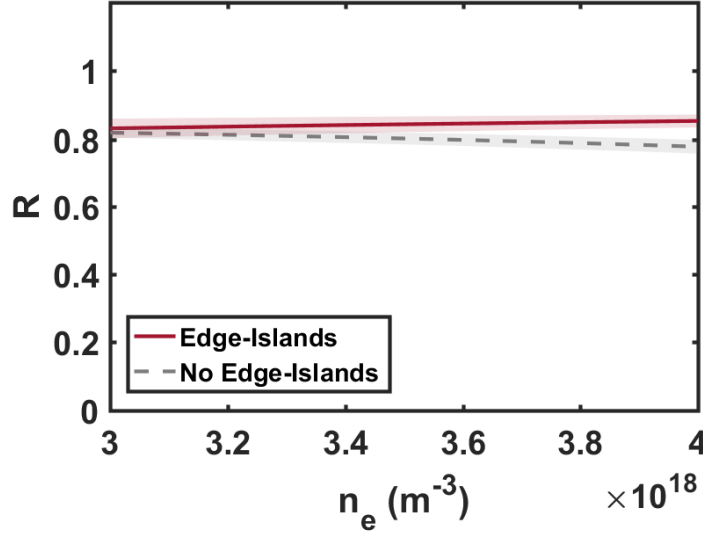
Figure 4.12 The global recycling coefficient R for HSX plotted as a function of plasma density. This value is calculated using Equation 2.1. The shaded regions show the confidence region determined through linear error propagation. Data from the Edge-Islands configuration are shown with a solid red line and data from the No-Edge-Islands configuration are shown with a dotted gray line.

range from approximately 0.82-0.78. However, these values lie close to the overlapping range of the error bars, and it can be argued that R is very similar between the two configurations. The value of R is below 1, which means that there is an effective removal of $\approx 15\%$ of the recycling flux by the wall during each confinement time $\tau_{p,H}$, which represents the particle removal term discussed previously. However, as it is unchanged between both configurations, we do not have to consider it when comparing the relative confinement time scales. Our assumption that there is no impact of the island position on particle removal from the system (i.e. through the global recycling coefficient) considered in the particle balance was confirmed.

4.6 EMC3-EIRENE fueling efficiency coefficients in HSX

As we have discussed, a key quantity in the particle balance analysis is the fueling efficiency, f_{eff}, which is defined as the fraction of edge-sourced neutral particles that are ultimately ionized

within the confinement region. It is experimentally very difficult to make this measurement because it requires pinpointing both the starting location and the ionization location of all particles in the device. However, simulation lends itself extremely well to keeping track of the ionization location of all particles in the simulation domain and for this reason we will use EMC3-EIRENE [61], the current state-of-the-art physics tool, to determine f_{eff} for HSX.

EMC3-EIRENE was used to simulate both the Edge-Islands configuration and the No-Edge-Islands configuration in this work [63]. The simulation parameters between the two pairs of configurations were kept as similar as possible to facilitate comparison between the cases. These simulation parameters were based on information provided by Thomson profile measurements of plasma density and temperature like those shown in Fig. 4.3. It should be noted for the HSX simulations, only wall-sourced particles were included in the simulation. Using combined wall sourcing and a gas puff is left for future work. Below, we will discuss how the values of fueling efficiency calculated for these wall-sourced particles will be adapted to more physically represent the penetration of puff-sourced particles in what follows.

Calculations of the fueling efficiency in HSX are shown in Fig. 4.13 as a function of number of plasma particles. (The value of N_{tot} may appear small since the EMC3-EIRENE grid does not include the whole HSX volume. See Chapter 3 for more information about the EMC3-EIRENE computational grid.) The currently-attainable density is circled on this plot; the rest of the points are projections to higher densities that cannot be experimentally tested at HSX. At this realistic density value, the fueling efficiency in the Edge-Islands configuration is 0.70 and the fueling efficiency in the No-Edge-Islands configuration is 0.87, a factor of 1.24 increase. This increase is well outside of the estimated errors in the f_{eff} calculations (5-7 percent), as discussed in Chapter 3.

The particle source distribution showing the penetration of the ionized particle source in the HSX Edge-Islands and No-Edge-Islands configurations is shown in Fig. 4.14. In this figure, the two top plots show the plasma temperature profiles modeled by EMC3-EIRENE and they highlight

the edge island geometry (or lack thereof) in both configurations. In the two bottom plots, the ionization source rate S_p (in A, or particles/s) in each configuration is shown.

In Fig. 4.14, the effect of the edge magnetic structure becomes clear: in the Edge-Islands configuration, the ionization region is substantially more localized in the upper part of the bean shaped cross-section and the particle penetration length is shorter as compared to the No-Edge-Islands configuration. The scale of the S_p plots is adjusted (i.e. auto-scaled) to show this difference more clearly between both configurations. The region in which more of the neutral source rate is produced is the X-point region in between the island tips at the upper part of this bean shaped cross-section. Because of this reduced neutral penetration length into the plasma, the overall fueling efficiency is reduced in the Edge-Islands configuration. This reduction can be seen in Fig. 4.13 for both realistic HSX plasma parameters and also in the characteristic projected for higher plasma densities by EMC3-EIRENE modeling.

We postulate that the 8/7 island structure, because it is located within the ionization source region, is able to decouple the source location from the confinement region. This decoupling is primarily due to the locally increased temperatures at the 8/7 island X-point which result in a larger ionization percentage outside the LCFS. Note that in the Edge-Islands configuration, the ionization region is smaller and peaks near the 8/7 island X-point. This is in contrast to the plasma source rate in the No-Edge-Islands case which is more diffuse and penetrates deeper into the confinement region. In Chapter 6, we will discuss this idea in much greater detail.

The values of f_{eff} determined through this analysis represent the ability of wall-sourced particles to penetrate in HSX. However, for the fueling efficiency for Φ_{gas}, because these quantities were not directly simulated, the values of f_{eff} were adjusted by a constant factor to bring these penetration fractions closer to expected values. A scaling of the EMC3-EIRENE f_{eff} prediction was used, rather than a slab calculation, for example, because EMC3-EIRENE could still account for penetration differences stemming from magnetic topology in a way that no simple calculation could.
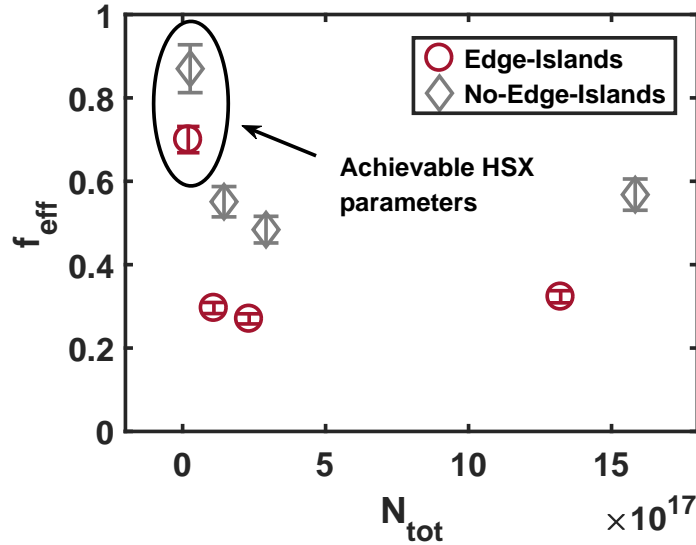
Figure 4.13 Figure showing EMC3-EIRENE calculated numerical fueling efficiency, f_{num} for both the Edge-Islands (red circles) and No-Edge-Islands (gray diamonds) configurations for a density scan. Values of f_{num} determined for realistic HSX parameters are noted on the plot (and may seem small due to the fact that the EMC3-EIRENE grid does not encompass the entire HSX volume, see Fig. 3.7). f_{num} is plotted as a function of N_{tot}, the total number of particles in the simulation. The error bars on this plot are determined from the method outlined in Chapter 3. EMC3-EIRENE calculations courtesy of A. Bader.

For the HSX value of f_{gas}, the EMC3-EIRENE prediction of f_{eff} was reduced by a factor of two in each configuration to yield values of 0.35 and 0.44 for the Edge-Islands and No-Edge-Islands configuration, respectively. This factor of 2 was used to reduce the values of f_{eff} calculated for puff-fueling to values closer to that found by a previous study at HSX with the DEGAS code [70] where the gas puff geometry was modeled and f_{gas} was shown to be ~ 43 percent (keeping in mind the caveats to DEGAS modeling, see discussion in Chapter 3). This reduction makes sense in terms of edge geometry and the position of the gas puff relative to the confinement region. Since gas-sourced particles must, on average, travel a longer distance to the confinement region than those borne at the strike points, it is reasonable that f_{gas} is smaller than f_{wall}.
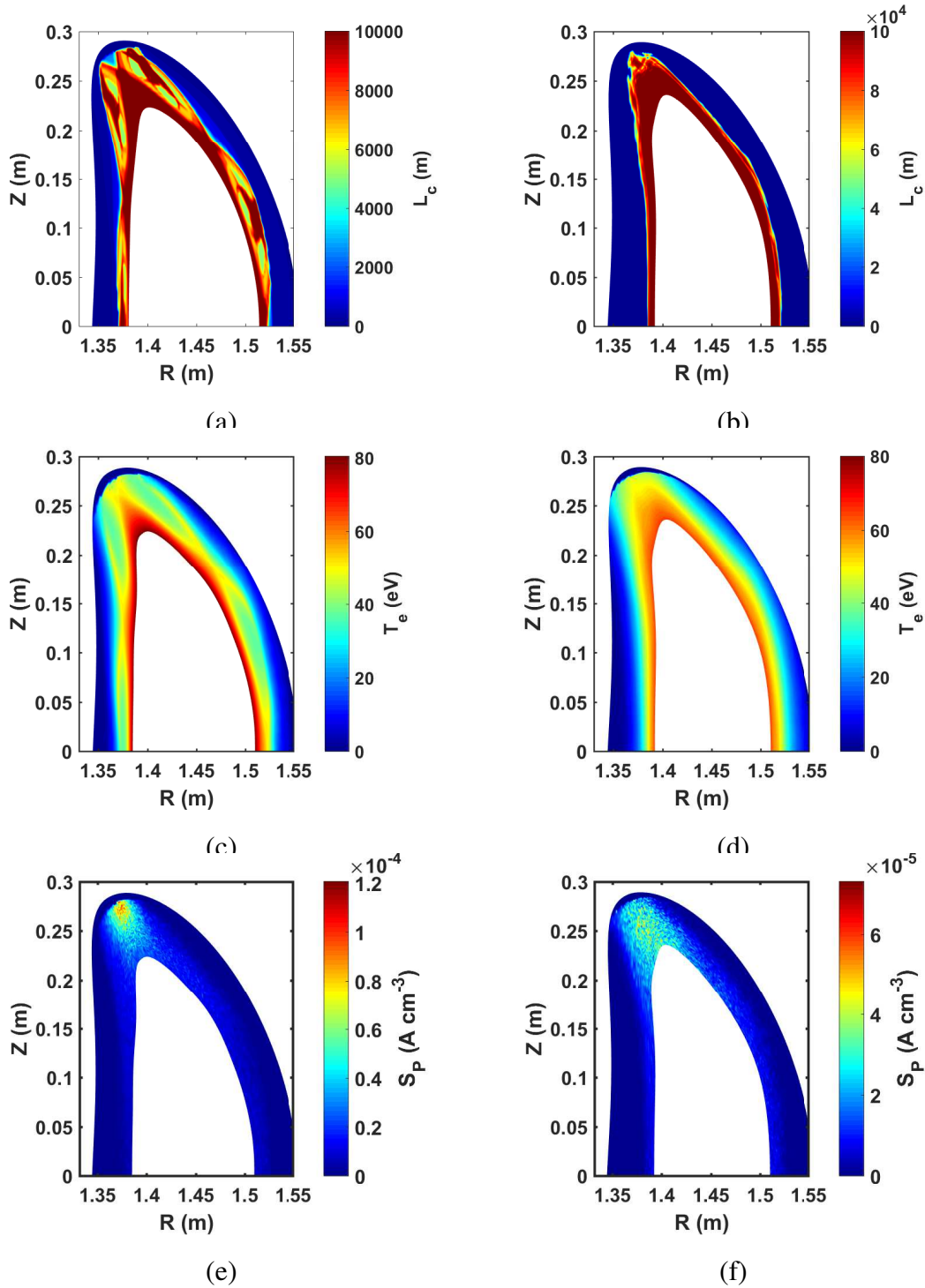
Figure 4.14 EMC3-EIRENE calculations for the Edge-Islands configuration (left column) and the No-Edge-Islands configuration (right column). (a) and (b) Plots of the magnetic connection length and Poincaré plots. (c) and (d) Plots of the self-consistently calculated plasma temperature, which highlights the island structure in (c). (e) and (f) Plots of the ionization source rate of hydrogen particles. In (e), the majority of the ionizations take place near the magnetic X-point. In (f), the ionization front is more diffuse and extends further into the confinement region. EMC3-EIRENE calculations courtesy A. Bader.

Therefore the final formulation of the HSX particle balance shown in Equation 4.2 can be expressed as:

$$\tau_p = \frac{N_{\text{tot}}}{-\frac{dN_{\text{tot}}}{dt} + \frac{1}{2}f_{\text{wall}}\Phi_{\text{gas}} + f_{\text{wall}}\Phi_{\text{wall}}} \tag{4.11}$$

4.7 Summary

In summary, we have used a variety of techniques, both experimental and numerical, to study particle behavior in HSX. We examined particle penetration and confinement in the Edge-Islands configuration (also called QHS) and the No-Edge-Islands configuration (also called 5 percent Well). Measurements of the decay of the interferometer line-averaged density in response to a perturbative hydrogen puff yielded values of $\tau_{p,H}^*$ a factor of 1.5 longer in the Edge-Islands configuration. Measurements of the decay of a the He-II signal in response to a perturbative helium puff yielded values of $\tau_{p,He-II}^*$ a factor of 1.6 longer in the Edge-Islands configuration.

A complete hydrogen particle balance yielded particle confinement times a factor of 1.32 longer in the Edge-Islands configuration, a value outside the error bars of both measurements. Furthermore, a positive trend of $\tau_{p,H}$ with density was observed in the Edge-Islands configuration, and a negative trend of $\tau_{p,H}$ with density was observed in the No-Edge-Islands configuration. These results, along with measurements of $\tau_{p,H}^*$, yield a global hydrogen recycling coefficient R of approximately 0.8 in both configurations.

Finally, EMC3-EIRENE calculations of particle penetration indicated that the fueling efficiency coefficient was 0.70 in the Edge-Islands configuration and 0.87 in the No-Edge-Islands configuration, a difference of a factor of 1.24, a value outside the error bars of both calculations.

Together, these results indicate that the change in edge configuration in HSX was able to impact the global particle behavior. We postulate that this difference in both penetration and particle confinement times stem from the fact that the edge topology changes were made in the plasma

source region (i.e. the 8/7 island chain was inserted in the peak ionization region). In Chapter 6, we will provide a much more in-depth analysis of these results.

References

6. Stangeby, P. C. *The plasma boundary of magnetic fusion devices* 717 pp. ISBN: 978-0-7503-0559-4 (Institute of Physics Pub, Bristol ; Philadelphia, 2000).

9. Winter, J. Wall conditioning in fusion devices and its influence on plasma performance. *Plasma Physics and Controlled Fusion* **38,** 1503. ISSN: 0741-3335 (1996).

26. Canik, J. M., Anderson, D. T., Anderson, F. S. B., Clark, C., Likin, K. M., Talmadge, J. N. & Zhai, K. Reduced particle and heat transport with quasisymmetry in the Helically Symmetric Experiment. *Physics of Plasmas* **14,** 056107. ISSN: 1070664X (2007).

28. Gerhardt, S. P. *Measurements and modeling of the plasma response to electrode biasing in the hsx stellarator* PhD thesis (Univeristy of Wisconsin - Madison, 2004).

35. Schmitz, O., Coenen, J., Frerichs, H., Kantor, M., Lehnen, M., Unterberg, B., Brezinsek, S., Clever, M., Evans, T., Finken, K., Jakubowski, M., Kraemer-Flecken, A., Phillips, V., Reiter, D., Samm, U., Spakman, G. & Telesca, G. Particle confinement control with resonant magnetic perturbations at TEXTOR. *Journal of Nuclear Materials* **390-391,** 330–334. ISSN: 00223115 (2009).

36. Soukhanovskii, V., Maingi, R., Raman, R., Kugel, H., LeBlanc, B., Roquemore, A., Skinner, C. & NSTX Research Team. Core fueling and edge particle flux analysis in ohmically and auxiliary heated NSTX plasmas. *Journal of nuclear materials* **313,** 573–578. ISSN: 0022-3115 (2003).

37. Maingi, R., Jackson, G. L., Wade, M. R., Mahdavi, M. A., Mioduszewski, P. K., Haas, G., Schaffer, M. J., Hogan, J. T. & Klepper, C. C. Control of wall particle inventory with divertor pumping on DIII-D. *Nuclear fusion* **36,** 245 (1996).

38. Brower, D. L., Deng, C., Ding, W. X., Anderson, D. T. & Mason, W. Multichannel interferometer system for the helically symmetric experiment. *Review of Scientific Instruments* **72,** 1081. ISSN: 00346748 (2001).

39. Deng, C., Brower, D. L., Ding, W., Almagri, A. F., Anderson, D. T., Anderson, F. S. B., Gerhardt, S. P., Probert, P. & Talmadge, J. N. First results from the multichannel interferometer system on HSX. *Review of scientific instruments* **74,** 1625–1628. ISSN: 0034-6748 (2003).

40. Park, H. K. A new asymmetric Abel-inversion method for plasma interferometry in tokamaks. *Plasma physics and controlled fusion* **31,** 2035 (1989).

55. Gerhardt, S., Canik, J., Anderson, D. & Owen, L. Ha detector system for the Helically Symmetric Experiment. *Review of scientific instruments* **75,** 2981–2984. ISSN: 0034-6748 (2004).

58. Heifetz, D., Post, D., Petravic, M., Weisheit, J. & Bateman, G. A Monte-Carlo model of neutral-particle transport in diverted plasmas. *Journal of Computational Physics* **46,** 309–327 (1982).

59. Frerichs, H., Reiter, D., Schmitz, O., Evans, T. & Feng, Y. Three-dimensional edge transport simulations for DIII-D plasmas with resonant magnetic perturbations. *Nuclear Fusion* **50,** 034004. ISSN: 0029-5515, 1741-4326 (Mar. 2010).

61. Feng, Y., Sardei, F., Kisslinger, J., Grigull, P., McCormick, K. & Reiter, D. 3D edge modeling and island divertor physics. *Contributions to Plasma Physics* **44,** 57–69. ISSN: 1521-3986 (2004).

63. Bader, A., Anderson, D., Hegna, C., Feng, Y., Lore, J. & Talmadge, J. Simulations of edge configurations in quasi-helically symmetric geometry using EMC3–EIRENE. *Nuclear Fusion* **53,** 113036. ISSN: 0029-5515, 1741-4326 (1st Nov. 2013).

66. Philipps, V. Analysis of outgassing after Joint European Torus discharges under beryllium first wall conditions. *Journal of Vacuum Science & Technology A: Vacuum, Surfaces, and Films* **11,** 437. ISSN: 07342101 (Mar. 1993).

67. Tramontin, L., Garzotti, L., Antoni, V., Carraro, L., Desideri, D., Innocente, P., Martines, E., Serianni, G., Spolaore, M. & Vianello, N. Particle balance during edge biasing experiments in the reversed field pinch RFX. *Plasma physics and controlled fusion* **44,** 195 (2002).

68. Hirooka, Y. & Sakamoto, M. Modeling of global particle balance in steady-state magnetic fusion devices–Analysis of the recent data from the TRIAM-1M tokamak. *Journal of nuclear materials* **313,** 588–594. ISSN: 0022-3115 (2003).

69. Kotz, J. C., Treichel, P. M. & Weaver, G. C. *Chemistry and chemical reactivity* Sixth. bibtex: Chembook (Thomson Brooks/Cole, 2006).

70. Stephey, L., Bader, A., Anderson, D., Talmadge, J., Hegna, C. & Anderson, F. *Modeling Neutral Hydrogen in the HSX Stellarator* in *APS Division of Plasma Physics Meeting* (2012).

Chapter 5

Particle penetration and confinement in W7-X

5.1 Introduction

In this chapter, results from a similar assessment of the particle fueling and exhaust balance of both the Increased Iota and Standard configurations at W7-X are shown. This study was performed during the initial operational phase of W7-X, in which the plasma boundary was defined by five poloidal limiters [71]. The device performance exceeded expectations for this initial startup campaign [72], but diagnostic access and availability was still limited [46]. The main measurements used in this study are the line integrated density $\bar{n}_e(t)$ from the single-channel interferometer[43], Thomson scattering profiles for electron density $n_e(r)$ and electron temperature $T_e(r)$ and an absolutely calibrated filterscope system [54], which allowed flexible acquisition of line integrated atomic line emission signals for hydrogen, helium and carbon. The analysis approach was the same as explained before. Effective particle confinement times for helium were measured by perturbative gas injection experiments and the global particle confinement time τ_p was inferred using the same single reservoir particle balance as used for HSX.

A brief summary of the results in this chapter are as follows: in the Increased Iota configuration (the inward-shifted 5/6, and edge 5/5 island configuration), longer values of $\tau_{p,\text{He-I}}^*$ and $\tau_{p,\text{He-II}}^*$ were measured by a factor of 1.5 and 1.2, respectively. These results indicate that to some degree, helium transport was impacted by the change in edge configuration, although a full helium particle balance would be required to say definitively how much. (This information would also be required to
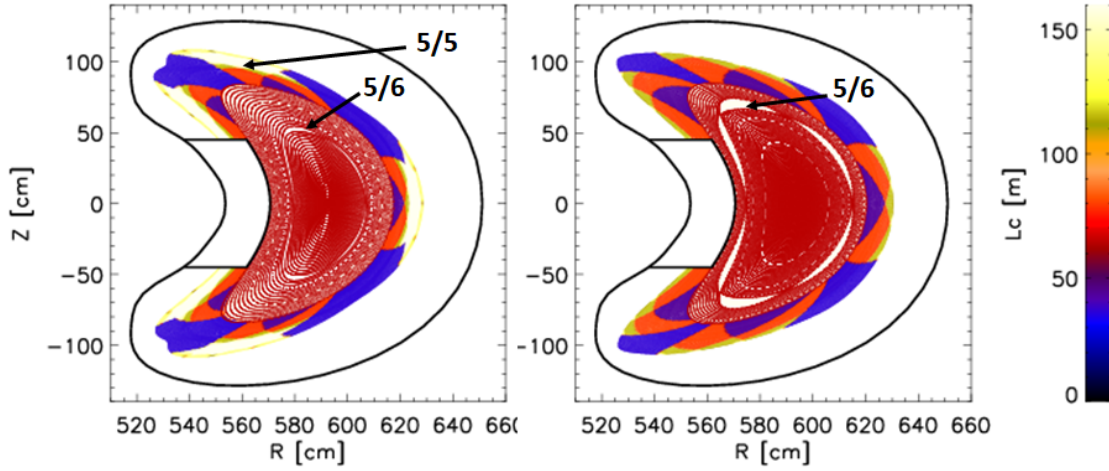
Figure 5.1 Overlay of EMC3-EIRENE connection length calculations (colored regions) with Poincaré plots (red dots) for the W7-X configurations investigated in this study: the Increased Iota configuration (left) and the Standard configuration (right). The 5/5 island is located outside the LCFS in the Increased Iota configuration and in the Standard configuration, both the 5/5 and the 5/6 islands have been shifted radially outward, moving the 5/5 outside the edge region. Plots courtesy of F. Effenberg.

understand why He-I and He-II had different decay times.) Almost no differences were found in the particle confinement time ($\sim$ 150-200 ms) between configurations. Likewise, almost no differences were found in the EMC3-EIRENE calculated limiter fueling efficiency between configurations ($\sim$ 0.85). We hypothesize this lack of difference could be the result of changing the topology in the far SOL where it is generally too cold to affect the ionization source rate. This will be discussed in more detail in Chapter 6. Finally, using measurements of $\tau_{p,H}^*$ and $\tau_{p,H}$ we obtain a hydrogen recycling coefficient of approximately 1.1 in both configurations.

5.2 Magnetic configurations examined at W7-X

The two configurations studied at W7-X are shown in Fig. 5.1. The Increased Iota configuration is shown on the left and the Standard configuration is shown on the right. In both plots, the Poincaré plot for each configuration is shown with red dots, and the colored regions show the edge connection length structure computed by EMC3-EIRENE with the longest connection lengths
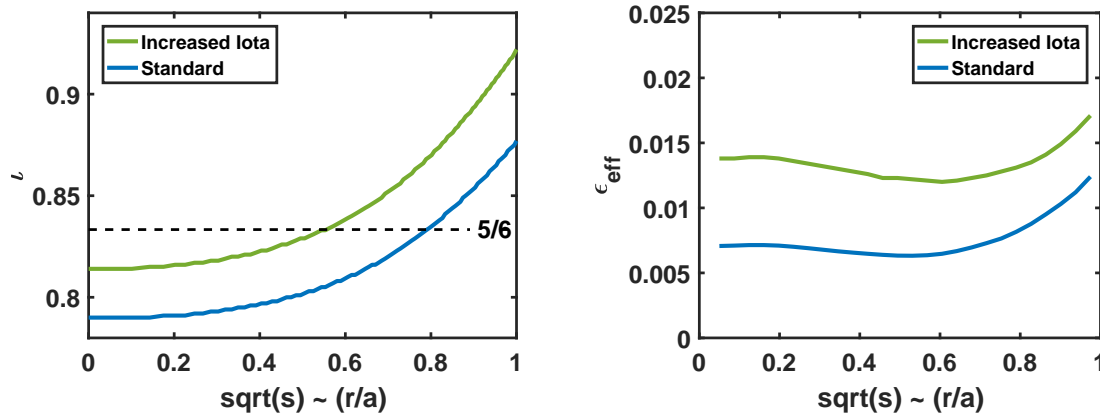
Figure 5.2 (Left) The iota profile in the Standard configuration (purple), the Increased Iota configuration (yellow), and several intermediate configurations. (Right) The effective ripple in the Standard configuration (purple), the Increased Iota configuration (yellow), and several intermediate configurations. Data courtesy of J. Geiger.

shown in white. Note that at W7-X, 5 stellarator-symmetric inboard limiters were present, indicated by the rectangular structure outlined in black. In the Standard configuration, a 5/6 island was present just inside the LCFS, relatively close to the limiters. To create the Increased Iota configuration, the iota profile was raised to move the 5/6 chain further inside the LCFS, and to introduce the 5/5 island chain into the edge. The Increased Iota configuration has an effective ripple, ϵ_{eff}, approximately a factor of two greater than that in the Standard configuration. The iota profiles and ϵ_{eff} profiles for both configurations are shown in Fig. 5.2. This very modest change in effective ripple was intended to minimize any changes in core transport.

Thomson profile data from the two W7-X magnetic configurations are shown in Fig. 5.3. Data in the Increased Iota configuration are shown in green and data in the Standard configuration are shown in blue. These profiles are fits generated from the measurement points. The shaded regions above and below the fit lines indicate the 95 percent confidence region. Unlike at HSX, these measurements suggest that the density and temperature profiles appear to be very similar between the two configurations despite the increase in ϵ_{eff} of approximately a factor of two. Perhaps as
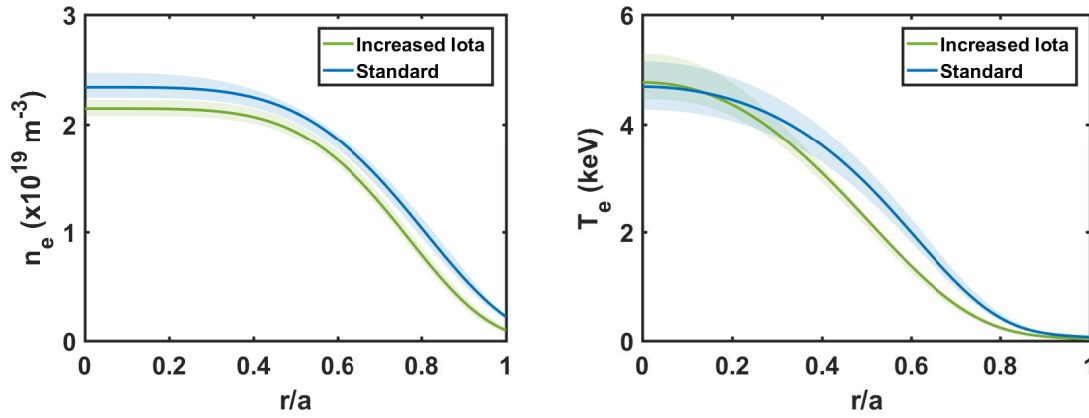
Figure 5.3 Thomson scattering measurements in the W7-X Increased Iota configuration (green) and in the Standard configuration (blue). The density profile is shown on the left and the temperature profile is shown on the right. The solid lines are fit lines to the measured data points. The shaded regions represent the 95 percent confidence error bars for each fit.

a "spoiler alert", this lack of difference in temperature and density profiles is in agreement with the very modest changes in the overall particle balance and confinement times between the two configurations, as will be discussed in detail in what follows.

We will perform a similar analysis for the W7-X data as was performed for the HSX data. For safety reasons, only a perturbative helium puff was allowed at W7-X. (Hydrogen, along with hydrocarbons, were considered unsafe due to a small leak in the fast gas injection system.) In addition, we will perform a full particle balance analysis to determine the particle confinement time. We have only enough information to perform this balance for hydrogen, not for helium. Therefore the helium measurements will provide only measurements of impurity τ_p^*. For this same reason, we can only measure the recycling coefficient of hydrogen particles since this calculation requires both τ_p and τ_p^* to be known. Note that at W7-X, a power scan was performed instead of a density scan. However, due to lack of active density control, the density did not remain constant in the shots analyzed in this work, which results in some spread in the data in the figures that follow.
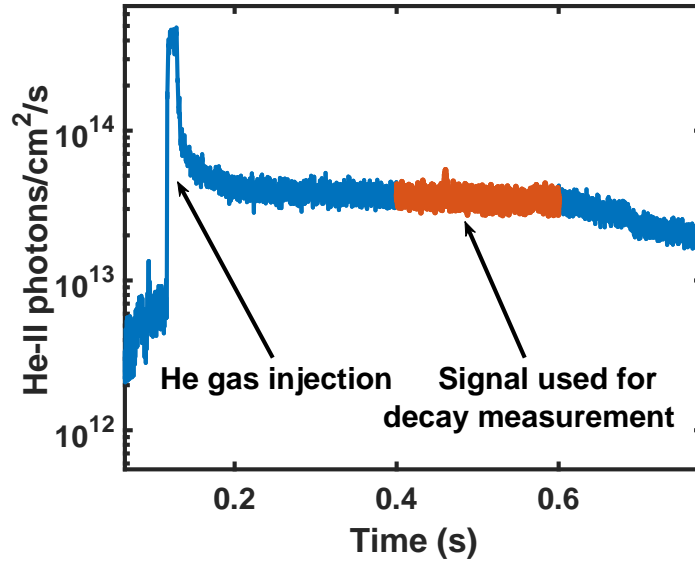
Figure 5.4 A representative He-II emission time trace from W7-X showing the helium gas injection at 250 ms and the signal used to determine $\tau^*_{p,\text{He-II}}$ which is highlighted in orange (400-600 ms). An exponential curve was fit to this section of data and the resulting decay constant yields the value of $\tau^*_{p,\text{He-II}}$.

5.3 Effective particle confinement time in W7-X

A fast piezo valve was used to make a single 20 ms helium injection of $1\text{x}10^{19}$ particles into a hydrogen plasma. The number of injected helium particles was kept constant in each discharge. A filter-scope diagnostic [50, 51, 52] was used to measure the emission decay of both He-I at λ=667.8 nm and He-II at λ=468.6 nm in two separate poloidal positions at the toroidal location of the gas injection in module 5. An additional He-I channel observing the limiter in module three was used to determine He-I decay at this position as well. The details of the particular experimental setup are described in [54].

In Fig. 5.4, an example of He-II line emission time trace is shown, which was used to determine $\tau^*_{p,\text{He-II}}$. Here the He-II line emission is shown and the time of the helium injection is indicated. Shortly after the gas injection, a fast peaking of the helium emission is seen with a rapid immediate
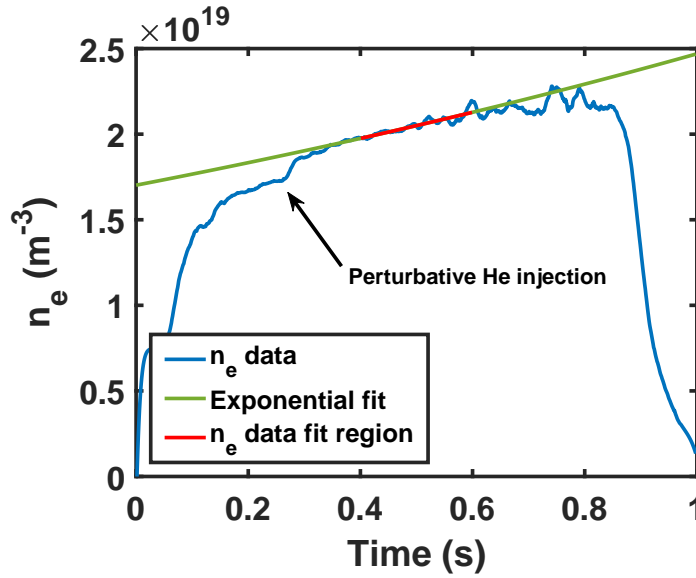
Figure 5.5 Representative plot of the W7-X interferometer n_e time trace in the Standard configuration. The n_e signal is shown by the blue line, the analysis region between 400-600 ms is shown by the red line, and the resulting exponential fit is shown by the green line. Note that the rising density profile results in a value of $\tau_{p,H}^*$ that is negative.

decay from direct ionization ($\sim$ several ms). Measuring this rapid decay would therefore provide information regarding helium ionization, but would not provide information regarding the system confinement and recycling properties. For this reason the longer timescale is used (between 400 and 600 ms), marked as orange in Fig. 5.4, to determine $\tau_{p,\mathrm{He}}$. Note that in both cases, the signal used for the decay measurement appears linear on this log scale plot and is therefore suitable for exponential fitting.

The decay of helium impurity emission was measured to determine $\tau_{p,\mathrm{He\text{-}I}}^*$ and $\tau_{p,\mathrm{He\text{-}II}}^*$. These helium impurity injections were performed in both magnetic configurations and also at two levels of heating power: low power (2 MW) and high power (2.7 MW). The characteristic decay time determined from both He-I (viewing limiter 3) and He-II (at the same toroidal angle as the gas injection) measurements are shown in Fig. 5.6. The value of $\tau_{p,\mathrm{He\text{-}I}}^*$ and $\tau_{p,\mathrm{He\text{-}II}}^*$ is always longest in the Increased Iota configuration.

Given that a measurement of $\tau_{p,H}^*$ is necessary to compute the global recycling coefficient R, we perform an additional exponential fit on the monotonically rising interferometer density signal. Because the helium injection is relatively small compared to the wall and limiter hydrogen source rates (roughly a factor of 10 smaller, as will be shown in what follows), the interferometer density can be assumed to represent predominately hydrogen. This analysis yields $\tau_{p,H}^*$ which is shown in Fig. 5.6. Because the density profile is monotonically rising, the fit coefficient of the exponential is negative, which in turn gives a negative value of $\tau_p^* H$, showing that in this single reservoir balance the fuleing term overcomes the outflow $-N/\tau_p$. This over-fueled situation will be discussed again in Section 5.5, where the recycling coefficient is extracted.

It should be noted that the error bars in all plots shown in Fig. 5.6 are the uncertainties in the 95 percent confidence exponential fit for each individual data point. The shaded regions above and below the fit line indicate the mean standard deviation from the fit line for data in each configuration.

5.4   Particle balance in W7-X

To infer the particle confinement time, τ_p, the same particle balance as discussed in Chapter 2. The particle balance described in Equation 2.2 was adapted for W7-X as follows. Because there is no external gas fueling (i.e. no main gas fueling nor perturbative fueling) during our analysis window, this term can be neglected. Similar to HSX, the pumping rates will also be neglected due to their slow throughput relative to the shot duration. When these terms are removed, we are left with the following formulation for W7-X:

$$\tau_p = \frac{N_{tot}}{-\frac{dN_{tot}}{dt} + f_{\text{lim}}\Phi_{lim} + f_{\text{wall}}\Phi_{wall}} \tag{5.1}$$
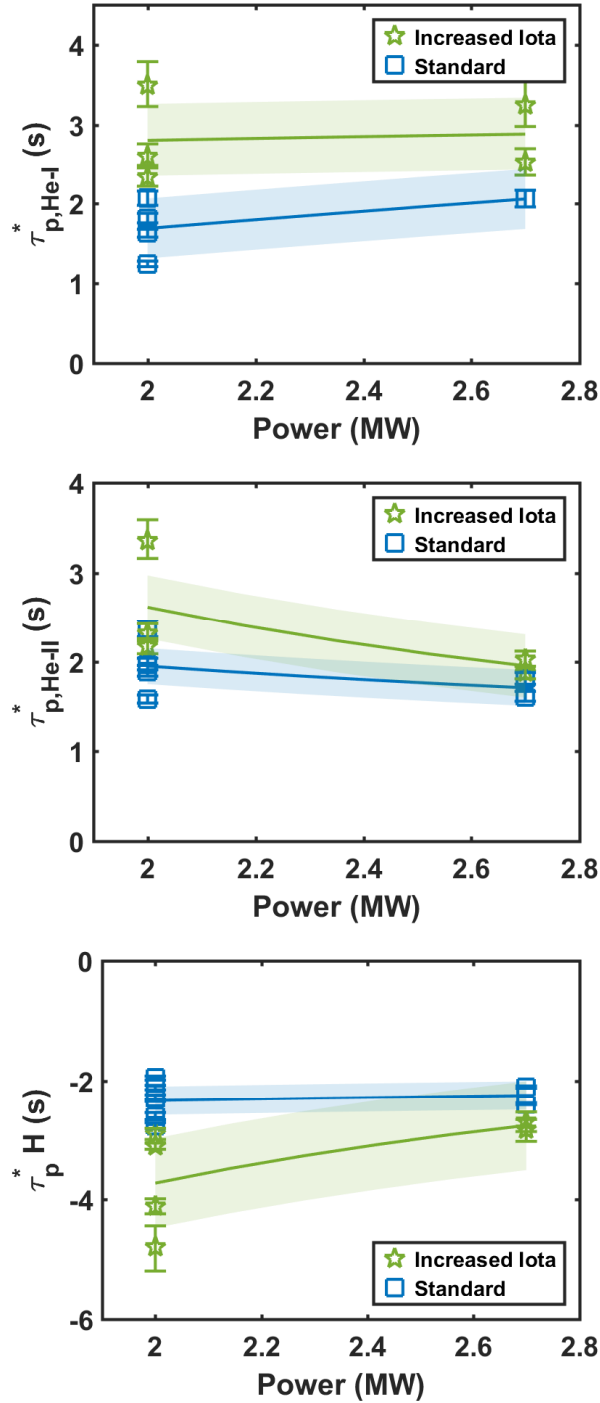
Figure 5.6 (Top) $\tau^*_{p,\text{He-I}}$ as a function of heating power measured from the decay of a perturbative helium puff using the 468.6 nm line. The solid lines indicate a power function fit for each configuration. (Middle) $\tau^*_{p,\text{He-II}}$ as a function of heating power measured from the decay of a perturbative helium puff using the 667.8 nm line. The solid lines indicate a power function fit for each configuration. (Bottom) $\tau^*_{p,H}$ as a function of heating power measured from the decay of the interferometer line-averaged density. The values of $\tau^*_{p,H}$ are negative because the plasma density is rising rather than falling. The solid lines indicate a power function fit for each configuration.

In the sections that follow we will describe how we determined each term necessary to complete the balance outlined in Equation (5.1). Because the fueling efficiency coefficients were determined using EMC-EIRENE modeling, the details of these quantities will be discussed in Section 5.6.

5.4.1 Total number of particles, N_{tot}

Similar to HSX, the N_{tot} term was determined by multiplying the line averaged density from the W7-X interferometer by the confinement volume for each configuration computed with EMC3-EIRENE [73]. This process has been described in detail in Section 2.4.1. The calculated volume of the W7-X Standard configuration is 27.14 m^3 and the volume of the Increased Iota configuration is 26.06 m^3. To find $\frac{dN_{tot}}{dt}$, the change in N_{tot} during the analysis window from 400-600 ms was determined. The values of the N_{tot} and $\frac{dN_{tot}}{dt}$ terms for each shot used in the analysis are shown in Fig. 5.8(a) and (b), respectively. Data in the Increased Iota configuration are shown as green stars and data in the Standard configuration are shown as blue squares.

The uncertainty in the value of N_{tot} was determined by first removing the constant rise (since this rise is already accounted for in the $\frac{dN_{tot}}{dt}$ term) by fitting a line to the data and subsequently subtracting this quantity. Then we find the standard deviation in the interferometer signal during our analysis window. This uncertainty is applied to both the N_{tot} and the $\frac{dN_{tot}}{dt}$ terms and is approximately 1-3 percent. These uncertainties, $\Delta_{N_{tot}}$ and $\Delta_{\Delta N_{tot}}$ are displayed as error bars for each data point in Fig. 5.8(a) and (b). Therefore we have:

$$N_{tot} = \bar{n}_e V_{conf} \tag{5.2}$$

and

$$\Delta N_{tot} = \Delta \bar{n}_e V_{conf} \tag{5.3}$$

5.4.2 Limiter particle flux, Φ_{lim}

The Φ_{lim} and Φ_{wall} terms for W7-X were both determined through absolutely calibrated filter-scope measurements [54]. The filter-scope channel spot size covered approximately the width of limiter 3 (approximately 15 cm in diameter) and covered approximately 20 percent of the total surface area, so it is therefore assumed that this spot is large enough to be representative of the general limiter particle flux. This assumption is not ideal, but necessary to complete this analysis. Additionally, it is assumed that all five limiters had identical particle fluxes. This assumption was necessary to complete the particle balance analysis, because the limiter observation in this module was the only limiter with calibrated H_α photon flux measurements. The H_α photon flux in from this limiter spot was then multiplied by the total limiter area of 0.86 m^2 for all five limiters, determined from design drawings for the limiters. This total photon flux was multiplied by the S/XB coefficient 13.36 based on limiter Langmuir probe temperature and density data, and this value was multiplied by 2 to include the contribution from molecular particles [74]. This yields the total value of Φ_{lim}.

The uncertainty in the limiter particle flux, $\Delta\Phi_{\text{lim}}$ is determined through linear error propagation of several terms: 1) the estimated error in the H_α signals due to calibration error ΔC_{H_α} (~ 11 percent), 2) the standard deviation of the H_α signals during the analysis window ΔI_{H_α} (~ 15-30 percent), 3) the estimated error in the limiter surface area estimation (~ 5 percent), and 4) the estimated error in the S/XB coefficient between 30-60 eV (~ 13 percent). This error is plotted for each data point in Fig. 5.8(d). The total value of $\Delta\Phi_{\text{lim}}$ is ~ 20-40 percent.

$$\Phi_{lim} = c_{H_\alpha} I_{H_\alpha} A_{lim} \beta_{SXB} \tag{5.4}$$

$$\Delta\Phi_{lim} = \sqrt{(\Delta c_{H_\alpha})^2 + (\Delta I_{H_\alpha})^2 + (\Delta A_{lim})^2 + (\Delta\beta_{SXB})^2} \tag{5.5}$$

5.4.3   Wall particle flux, Φ_{wall}

The wall sourced particle flux was also determined using measured values of H_α photon flux, this time from a line of sight intersecting the W7-X wall. Like the Φ_{lim} measurement, the Φ_{wall} measurement is based purely on experimental measurements. The surface area of the W7-X wall was estimated by assuming a cylindrical geometry. Using a major radius of 5.5 m and a minor radius of 0.53 m, this yielded a wall area of 110 m^2. Based on camera images captured by the visible fast camera diagnostic [75], in general only the inboard half of the W7-X wall appeared to radiate. Based on these images, we therefore divide the total wall area in half to yield an effective wall source area of 55 m^2 with an estimated 20 percent uncertainty to account for both geometrical and plasma source estimation uncertainties. We multiply the filterscope measured H_α photon flux by the effective wall source area, and then multiply this product by the S/XB coefficient 11.38 based on edge measurements of temperature and density [76]. Finally we multiply this quantity by 2 to include the contribution from molecular particles in the same manner as the limiter flux measurements. This yields the total value of Φ_{wall}.

The uncertainty in the wall particle flux $\Delta\Phi_{\text{wall}}$ is determined in a similar manner to the limiter particle flux. It is determined through linear error propagation of the following terms: 1) the estimated error in the H_α signals due to calibration error ΔC_{H_α} (~ 11 percent), 2) the standard deviation of the H_α signals during the analysis window ΔI_{H_α} ($\sim 10\text{-}15$ percent), 3) the estimated error in the wall surface area estimation (~ 20 percent), and the estimated error in the S/XB coefficient between 30-40 eV (~ 7 percent). This error is plotted for each data point in Fig. 5.8(c). The total value of $\Delta\Phi_{\text{wall}}$ is $\sim 20\text{-}30$ percent.

$$\Phi_{wall} = c_{H_\alpha} I_{H_\alpha} A_{wall} \beta_{SXB} \tag{5.6}$$
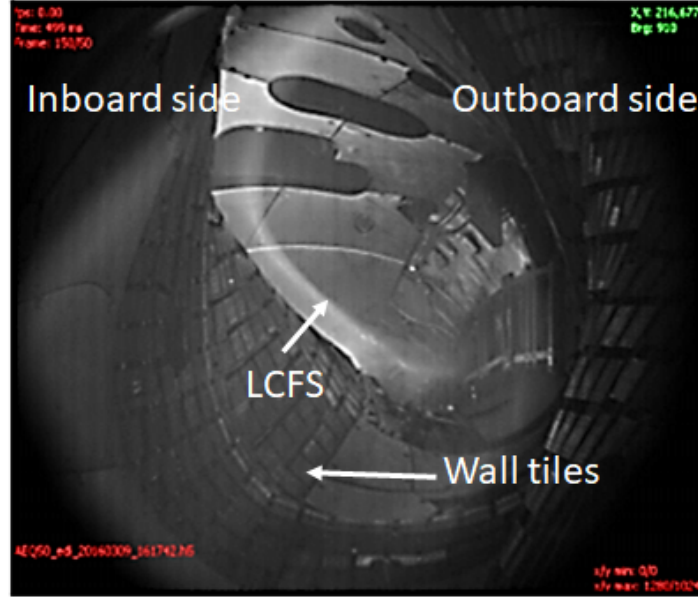
Figure 5.7 Image captured with the visible fast camera diagnostic viewing part of module 5. The image is unfiltered and likely comprised of a combination of hydrogen and impurity emission. This image is representative of general wall emission behavior and shows that most emission appears to come from the inboard side of W7-X. Image courtesy T. Szepesi.

$$\Delta\Phi_{wall} = \sqrt{(\Delta c_{H_\alpha})^2 + (\Delta I_{H_\alpha})^2 + (\Delta A_{wall})^2 + (\Delta\beta_{SXB})^2} \qquad (5.7)$$

5.4.4 Particle confinement time, $\tau_{p,H}$

Now that we have determined all values necessary for the particle balance (with the exception of the fueling efficiency coefficients, which will be discussed in the following section), the final value of $\tau_{p,H}$ can be determined. This value is plotted as function of input heating power in Fig. 5.8(e). Over the range of heating power, the values of $\tau_{p,H}$ are approximately between 150 ms and 200 ms, with τ_p decreasing with increasing heating power. Similar to HSX, a single-term power series fitting was used to fit the data. This choice was made in order to express changes in τ_p^* and τ_p as a function of heating power. This fit is shown as a solid line in green and blue for the

Increased Iota and Standard configurations, respectively. At a heating power of 2.35 MW, the value of $\tau_{p,H}$ from the fit lines is approximately a factor of 1.05 larger in the Increased Iota configuration relative to the Standard configuration.

The uncertainty of all the component terms in Equation 5.1 are then determined through linear error propagation to determine the total error for all individual measurements of τ_p. This formulation is shown in Equation 5.8. This uncertainty is ~ 21 percent in the Increased Iota configuration and ~ 22 percent in the Standard configuration. These quantities can be seen in Fig. 5.8(e) calculated for each individual measurement. Similar to HSX, a power scaling fitting was determined, now as a function of heating power rather than density. This fit can be seen in Fig. 5.8(e). The shaded region indicates the mean standard deviation of the data points from the fit line. This is meant to give a confidence region for the power scale fit.

$$\Delta \tau_p = \sqrt{\begin{array}{l} (\frac{\partial \tau_p}{\partial N_{tot}})^2 (\Delta N_{tot})^2 + (\frac{\partial \tau_p}{\partial dN_{tot}/dt})^2 (\Delta dN_{tot}/dt)^2 + (\frac{\partial \tau_p}{\partial f_{lim}})^2 (\Delta f_{lim})^2 \\ + (\frac{\partial \tau_p}{\partial \Phi_{lim}})^2 (\Delta \Phi_{lim})^2 + (\frac{\partial \tau_p}{\partial f_{wall}})^2 (\Delta f_{wall})^2 + (\frac{\partial \tau_p}{\partial \Phi_{wall}})^2 (\Delta \Phi_{wall})^2 \end{array}} \tag{5.8}$$

5.4.5 Bremsstrahlung contributions

To address any concerns about the contributions of Bremsstrahlung emission contaminating the H_α filters and artificially inflating our photon flux measurements, we can examine spectra from a W7-X spectrometer. Unfortunately this spectrometer was usually not operating in the wavelength range that included the H_α line, so we will have to assume that this measurement is representative. It is shown in Fig. 5.9.

It is clear from these data that the H_α line is very strong relative to the continuous emission background, despite the fact that the H_α line was generally transmitted by the filters at 20-30 percent (see Fig. 2.5) of its peak. Any corrections or subtractions to the H_α photon flux would be
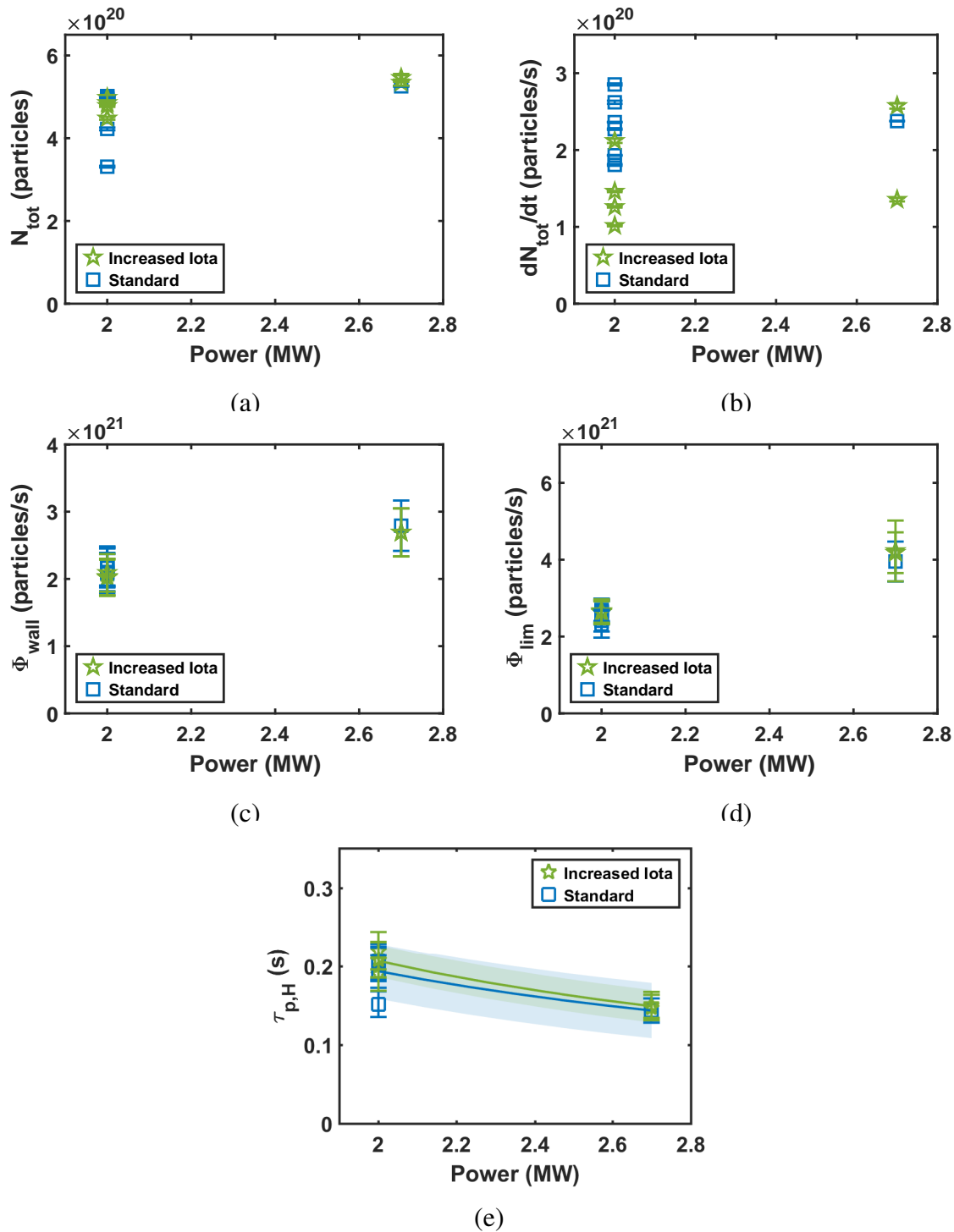
Figure 5.8 Important terms in the W7-X particle balance analysis for each individual plasma shot as a function of input power. Data from the Increased Iota configuration are shown with green stars and data from the Standard configuration are shown with blue squares. (a) Values of N_{tot}, (b) values of $\frac{dN_{tot}}{dt}$, (c) values of Φ_{wall}, (d) values of Φ_{lim}, (c) values of $\tau_{p,H}$. A power series fit to $\tau_{p,H}$ for each configuration is shown with a corresponding green and blue solid line. The shaded region indicates the mean standard deviation of the data points from the fit line.
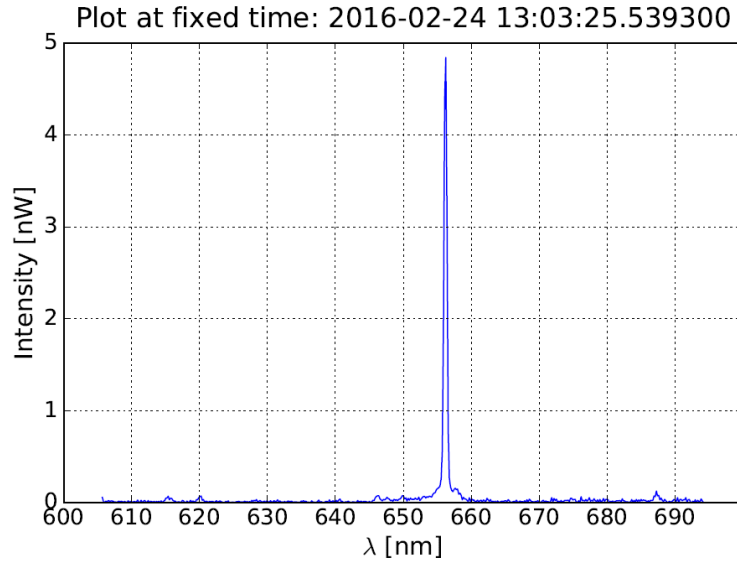
Figure 5.9 Spectra from a W7-X Standard configuration hydrogen discharge. The tall emission line is the $\text{H}_{\alpha line}$ at 656.38 nm which dominates any background emission contributions. Plot courtesy of V. Perseo.

arbitrary because these data were not available for the vast majority of shots analyzed in this work. Furthermore, this would be a very small correction (on the order of a few percent) which is dwarfed by the uncertainty that stems from other factors. For this reason we ignore the Bremsstrahlung contributions in this work.

5.4.6 Comparing filterscope particle flux to limiter Langmuir probe particle flux

It is perhaps natural to ask how the spectroscopically determined limiter particle fluxes compare to those measured by other diagnostics. The limiter Langmuir probes embedded in limiter 5 are the most obvious measurements for such a comparison. We will briefly describe how we use the measured temperatures and densities to determine a limiter particle flux.

The limiter Langmuir pins were mounted in stellarator symmetric positions above and below the midplane in tiles 2 and 7 on limiter 5. There were approximately 34 total pins, most of which were able to provide n_e and T_e data. Fig. 5.10 shows the placement and pin numbering of the
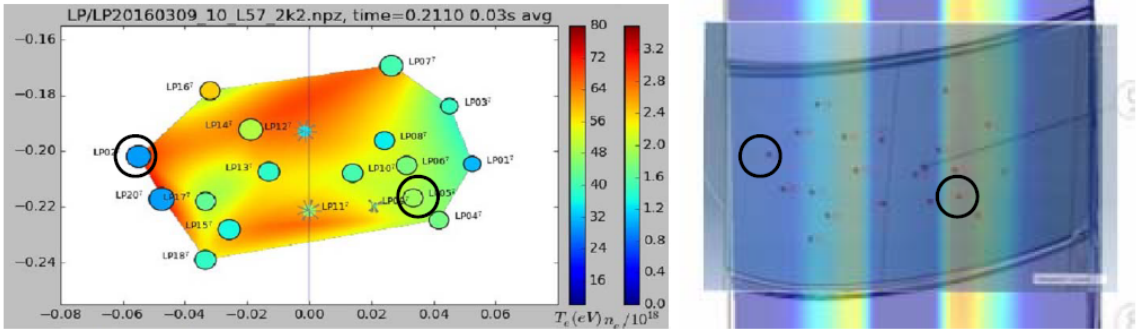
Figure 5.10 (Left) Map of limiter 5 langmuir probe locations on tile 7. Pins 2 (circled on left) and 5 (circled on right) were chosen at max/min locations of temperature and density in the Standard configuration. Plot courtesy of B. Blackwell. (Right) EMC3-EIRENE heat flux prediction for tile 7 with pins 2 and 5 circled. Plot courtesy of F. Effenberg.

W7-X Langmuir probes in tile 7 of limiter 3. Pins 2 and 5 were chosen because they lie in approximately maximum and minimum areas of heat flux and particle flux in the Standard configuration as predicted by EMC3-EIRENE simulations [73] which are also shown in Fig. 5.10.

We compare the particle flux measured by the filterscopes and the limiter langmuir probes for a single discharge, number 160308032. We keep the same analysis window, from between 400-600 ms. We will use the following formulation from Stangeby (Equation 2.56) [6]:

$$\Gamma_{se} = n_{se}v_{se} = n_{se}c_s = \frac{1}{2}n_0[k(T_e + T_i)/m_i]^{1/2} \tag{5.9}$$

where Γ_{se} is the particle flux through the sheath entrance, n_{se} is the plasma density in the sheath entrance, v_{se} is the particle velocity through the sheath entrance, c_s is the plasma sound speed, n_0 is the plasma density at the target, T_e and T_i are the electron and ion temperatures, respectively, and m_i is the mass of the ion (a proton in this case). A major weakness of using this formulation is that the ion temperature must be known. Unfortunately in OP 1.1, there were no measurements of this quantity. For this reason, we will assume that $T_e=T_i$ in our calculation based on the reasonably high collisionality in the W7-X edge.
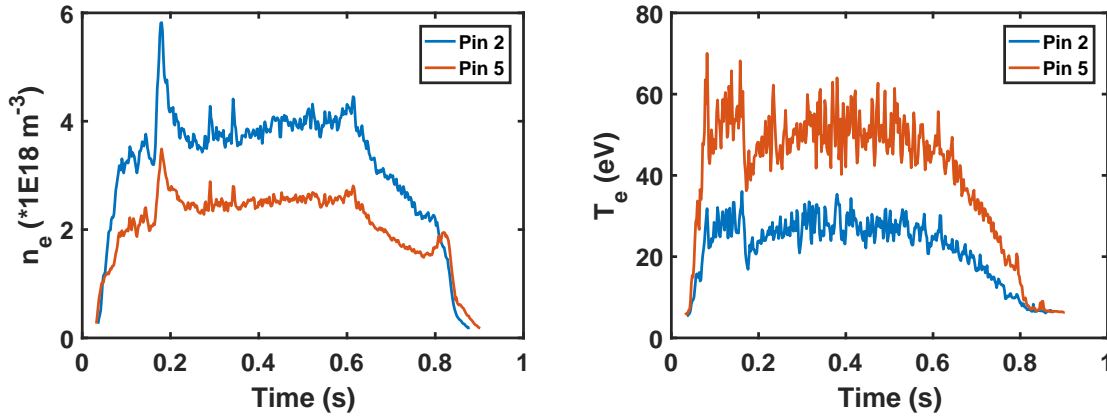
Figure 5.11 Langmuir probe data from limiter 5, tile 7, for a plasma discharge in the Standard configuration. Data from pin 2 are shown in blue and data for pin 5 are shown in orange. (Left) Time trace of n_e measured by pins 2 and 5. (Right) Time trace of T_e measured by pins 2 and 5. Data courtesy of B. Blackwell.

Analyzing data from between 400 and 600 ms in shot 160308032, pin 2 measures approximately T_e=25 eV and n_e=4x10^{18} m^{-3} and pin 5 measured approximately T_e=50 eV and n_e=2x10^{18} m^{-3}. We will treat these as our upper and lower limits of particle flux to limiter 5. Using equation 5.2, pin 2 yields a particle flux estimate of 1.38x10^{17} particles/cm^2/s and pin 5 yields a particle flux estimate of 9.79x10^{16} particles/cm^2/s.

These data can be compared to the calculated filterscope particle flux for this same discharge. The measured photon flux is approximately 1.2x10^{16} photons/cm^2/s. Using an S/XB coefficient value of 26.72 as previously described in section 5.4.2, we determine the particle flux to be 3.2x10^{17} particles/cm^2/s. This particle flux is approximately a factor of 2 larger than the high particle flux estimate from pin 2, and approximately a factor of 3 larger than the low particle flux estimate from pin 5.

If in fact the spectroscopic methods we have employed to measure the wall-sourced and limiter-sourced particle flux in W7-X are overestimating the particle flux, this would serve to underestimate the final particle confinement time. However we should again mention that we have no

measurements of the ion temperature, and the final value of the particle flux calculation depends on the square root of the ion temperature. These measurements confirm, at the very least, that the filterscope measurements and spectroscopic techniques employed are within the ballpark of other measured values of limiter particle flux, which provides some confidence in these measurements.

5.4.7 Comparing filterscope photon flux to overview video diagnostic photon flux

Another check for our calculated wall particle flux to limiter particle ratio can be made using the overview video diagnostic data. These wide-view images capture both a limiter and surrounding wall tiles within approximately 1 m. Even though these images are currently not absolutely calibrated to provide photon fluxes (and eventual particle fluxes through an S/XB coefficient), having both the limiter emission and the wall emission in a single image allows their intensities to be directly compared.

The overview video diagnostic captured images of all five limiters, but in this analysis we focus on limiter 3 since this is where the filterscope photon flux measurements were made. We chose two analysis regions: one in the center of limiter 3, and one on a dark part of the wall toroidally separated from the limiter. We use a rectangle mask to select only the pixels in our analysis regions and perform a mean over these regions. A sample limiter image from this diagnostic for Standard configuration shot 160308032 between 400-600 ms is shown in Fig. 5.12. This composite image is the mean of all frames captured within the analysis window and with the initial dark image (i.e. before the beginning of the plasma) subtracted from the mean image.

For all shots analyzed in this work, in both the Standard and Increased Iota configurations, we can compare the mean values in the limiter mask to the mean values in the wall mask. Then, we can find the overall mean ratio between the limiter mask and the wall mask. This overall mean ratio is 99, i.e. the limiter H_α photon flux is a factor of 99 greater than the wall photon flux.
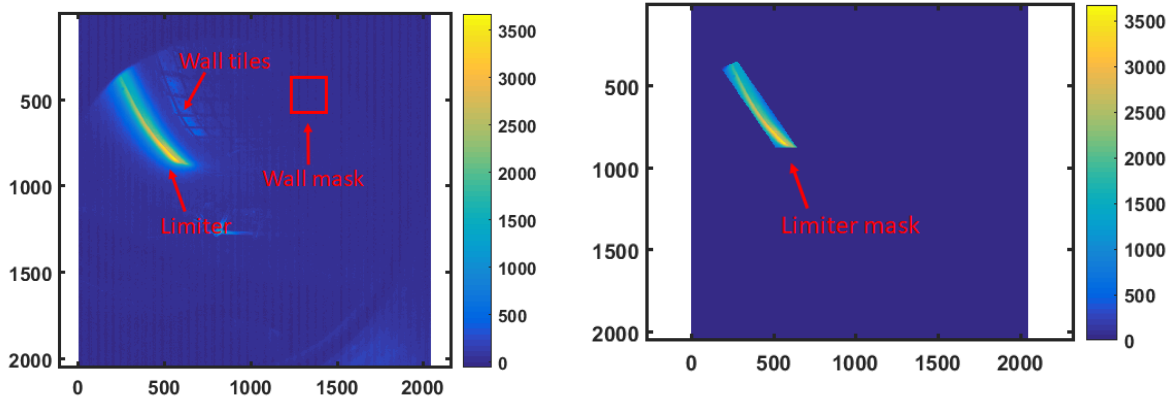
Figure 5.12 Images obtained with the overview video diagnostic system. These images were H_α filtered and are shown in units of intensity (arbitrary units). (R) Image showing the rectangular mask used to infer the mean wall particle source rate. (L) Image showing the rectangular mask used to infer the mean limiter particle source rate. Data courtesy C. Biedermann.

We can compare this to the mean ratio of the limiter 3 filterscope measurements and the wall measurements. We analyze all shots used in this work in both the Standard and Increased Iota configurations. The overall mean ratio of the limiter and wall photon flux is approximately a factor of 71, i.e. the limiter H_α photon flux is a factor of 71 greater than the wall photon flux. For reference, the difference between the total limiter surface area in W7-X (~ 0.86 m^2) and the total wall area (~ 110 m^2) is of approximately this same order (a factor of 128).

Despite the very different measurement techniques used, these ratios are different by a factor of less than 2 (approximately 1.4). The reasonable agreement of these numbers again provide some confidence in the relative difference in our limiter and wall particle flux calculations. It is possible we systematically under or over predict these fluxes which would ultimately raise or lower the final value of particle confinement time, but would not affect the differences in the values between the Standard and Increased Iota configuration.

5.5 Global recycling coefficient in W7-X

With both τ_p^* and τ_p extracted from measurements at W7-X, Equation 5.10 is used to determine the global recycling coefficient R. Since the measurements of both τ_p^* and τ_p were obtained as a function of heating power, R is computed over this same range using the power scaling fit lines which were previously determined. The values we obtain are shown in Fig. 5.13. The shaded confidence regions shown are calculated according to Equation 5.11 and the partial derivative weighting factors contribute strongly to the small total standard deviation. This calculation yields a value of R approximately equal to 1.1 for both levels of heating power. It should be noted that the value of R computed in each configuration is slightly different but agree within error bars.

$$R = 1 - \frac{\tau_p}{\tau_p^*} \tag{5.10}$$

$$\Delta R = \sqrt{(\frac{\partial R}{\partial \tau_p^*})^2 (\Delta \tau_p^*)^2 + (\frac{\partial R}{\partial \tau_p})^2 (\Delta \tau_p)^2} \tag{5.11}$$

This value of R≈1.1 represents particle release from the wall, i.e. a situation of over-fueling the plasma by wall particle release. As a consequence, the line-averaged density as measured by the interferometer was seen to rise monotonically in all plasmas in this study despite no additional external gas input. This density rise is a result of particle release by the limiter and/or the main wall during the analysis window. This over-fueling situation is consistent with minimal wall conditioning performed before the startup campaign experiments were conducted (e.g. baking at 150 degrees C only, which is below the threshold to remove impurities from carbon [77]). This result provides some additional confidence in our measurements of τ_p^* and τ_p since the R they yield is consistent with plasma observations and the anticipated wall conditions during the startup campaign at W7-X.
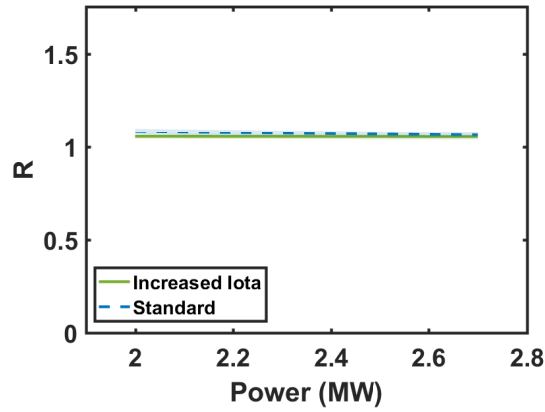
Figure 5.13 The global recycling coefficient R for W7-X plotted as a function of heating power. This value is calculated using Equation 3. The shaded regions are the sum in quadrature of the uncertainty in all of the component terms in this analysis. Data from the Standard configuration are shown with a solid blue line and data from the Increased Iota configuration are shown with a dotted green line.
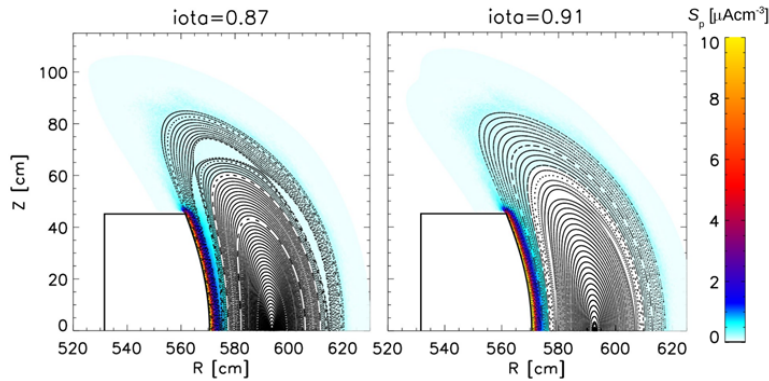
Figure 5.14 EMC3-EIRENE calculation of ionization source rate, S_p. Despite the change in edge structure, there were no substantial changes in the ionization source distribution. A flux surface averaged plot of these data are shown in Fig. 5.15 Plot courtesy F. Effenberg.

5.6   EMC3-EIRENE fueling efficiency coefficients in W7-X

EMC3-EIRENE was used to simulate both the Increased Iota configuration and the Standard configuration in this work [73]. Note that the values of T_e and n_e are self-consistently calculated based on the prescribed input power and core density of each case. The simulation parameters between the two pairs of configurations were kept as similar as possible to facilitate comparison
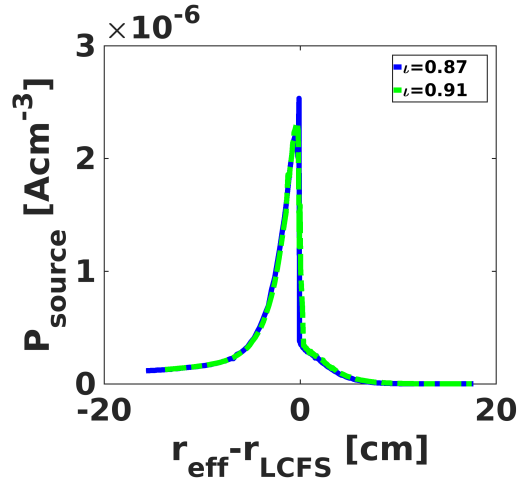
Figure 5.15 EMC3-EIRENE of ionization source rate for helium in both the Standard configuration (blue solid line) and Increased Iota configuration (green dotted line). The helium source profile is very similar to the hydrogen source profile (not pictured). Plot courtesy F. Effenberg.

between the cases. These choices were informed by Thomson profile measurements of plasma density and temperature like those shown in Fig. 5.3. It should be noted for the W7-X simulations, only limiter-sourced particles were included in the simulation (i.e. no wall-sourced particles were simulated because the limiter was expected to be the main source of recycling particles). Below, we will discuss how the values of fueling efficiency calculated for these limiter-sourced particles will be adapted to more physically represent the penetration of wall-sourced particles in what follows.

Figs. 5.14 and 5.15 show a plot of the ionization source rate S_p calculated in W7-X, the first is in real space coordinates and the latter is in flux surface averaged coordinates. The ionization source rate is key to determining the fueling efficiency, as described in detail in Section 4.6, as the quantity f_{eff} is defined as the total number of ionizations that occur inside the confinement region divided by the total number of ionizations. Data in the Increased Iota configuration are shown with a green dotted line and data in the Standard configuration are shown with a blue solid line. The x-axis of both plots have been shifted so that the location of the LCFS in each configuration overlaps at r=0. This plot shows very little difference in the limiter particle source rate profile between the

Increased Iota and the Standard configurations. This lack of difference in source rate profile results in, unsurprisingly, very little difference in the calculated fueling efficiency coefficients.

Fig. 5.16 shows the fueling efficiencies for the Increased Iota configuration and the Standard configuration in W7-X plotted as a function of total plasma particles. Data in the Increased Iota configuration are shown with green stars and data in the Standard configuration are shown with blue squares. Data in this plot are shown over the range of achievable densities for W7-X during the limiter operational phase (OP 1.1). This plot shows that in the Increased Iota configuration, the value of f_{eff} is approximately 0.81 and in the Standard configuration, the value of f_{eff} is approximately 0.87. At W7-X this ~ 7 percent difference in particle penetration between the two configurations is less substantial than that observed at HSX between the two configurations (~ 24 percent). This could be for several reasons, the most likely of which is the close proximity of the limiter to the LCFS. The second is that the higher W7-X plasma densities result in shorter particle ionization lengths, which in turn may cause the ionization region to depend less heavily on the edge topology. Future work will be required to better understand these differences. The uncertainty in the fueling efficiency in the Increased Iota configuration is ~ 3 percent and the uncertainty in the Standard configuration is ~ 2 percent, which have been included in the total error in the particle confinement time in Equation 5.8.

As was done at HSX, the W7-X calculations of fueling efficiencies for the wall need to be adjusted to better account for the difference in edge geometry between the limiter and the wall. Because the fueling efficiency coefficient calculated by EMC3-EIRENE for W7-X was for limiter-sourced particles, the fueling efficiency for these particles is substantially higher than for particles borne at the wall because it is located radially farther away. It is clear that the limiter fueling efficiencies need to be reduced to more accurately represent the wall particle penetration fraction, so we rely on a simple 1-D slab calculation to inform our decision to scale down these values. The original EMC3-EIRENE values of f_{eff} will be scaled based on this calculation as they can capture
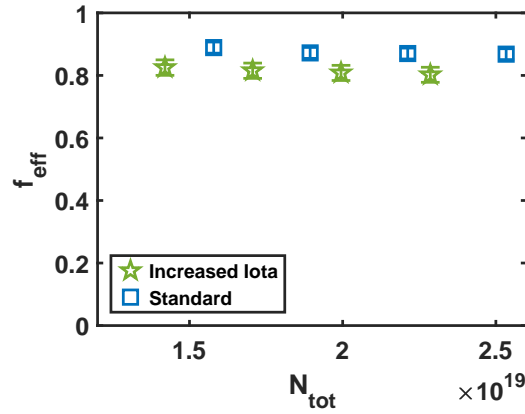
Figure 5.16 EMC3-EIRENE calculated numerical values of f_{eff} for the Standard and Increased Iota configurations in W7-X. The numerical f_{eff} is shown as a function of total number of plasma particles. Unlike the fueling efficiency study for HSX, this density range was achieved during the initial operational phase of W7-X. EMC3-EIRENE calculations courtesy of F. Effenberg.

differences in the particle penetration related to the magnetic geometry in a way that no simple calculation (like the one to follow) can.

This reduction factor was determined from the results of a 1-D slab calculation in which a Maxwell-Boltzmann distribution of 0.026 eV neutral molecular hydrogen was examined penetrating into a background plasma of 40 eV and background density of $1.3\text{x}10^{18}$ m^3 [76]. We assume the wall is a distance of 10 cm away from the confinement region. Particles must penetrate at least this distance to be ionized in the confinement region.

Using atomic data reaction rate coefficients, at a temperature of 40 eV, molecular hydrogen is 8.3 times more likely to ionize than to dissociate into two atomic hydrogen particles [78]. If we assume that all particles will either ionize or dissociate (a reasonable assumption in the W7-X edge), this means that 86 percent of particles will ionize and 14 percent will dissociate. We assume that all dissociated particles will ionize within the confinement region due to their increased Franck-Condon energy and correspondingly long mean free paths ($\sim$ 1 m). This makes the fueling efficiency at least 14 percent.
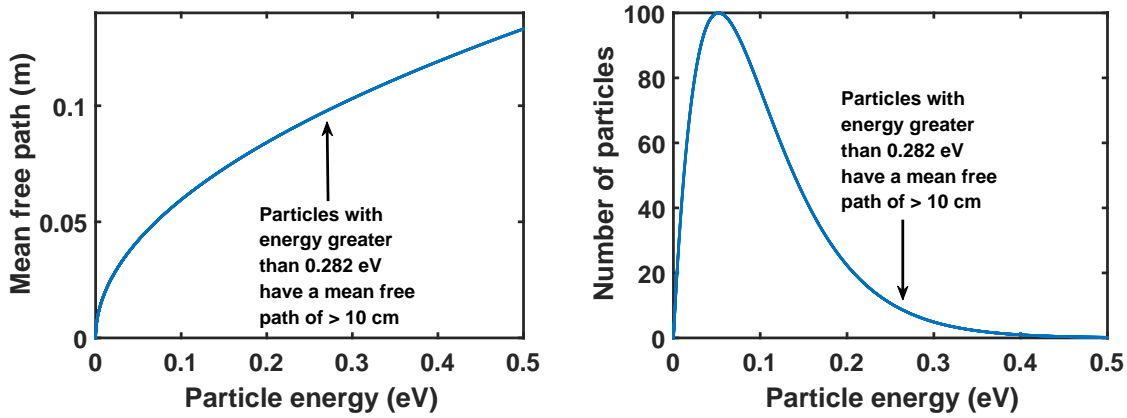
Figure 5.17 (Left) Plot of molecular hydrogen particle mean free path as a function of particle energy in eV. The energy at which particles have enough energy to penetrate 10 cm in the W7-X is noted on the plot. (Right) Plot of the Maxwell-Boltzmann energy distribution of molecular hydrogen particles in the W7-X edge. The energy at which particles have enough energy to penetrate 10 cm in the W7-X is noted on the plot (the high-energy tail of the distribution).

To determine the portion of particles that penetrate as a result of being part of the high-energy tail of the Maxwell-Boltzmann distribution, we perform a 1-D slab calculation [6] Equation 4.55. We use the following formulation:

$$\lambda_{iz} = \frac{v_n}{n_e < \sigma_{ion} v_e >} \tag{5.12}$$

where v_n is the velocity of the neutral, n_e is the plasma density, and $< \sigma_{ion} v_e >$ is the rate coefficient for the dominant ionization process (electron impact ionization).

At our given background plasma parameters in W7-X, we find that particles must have an energy greater than 0.282 eV to penetrate 10 cm into the confinement region. Given a Maxwell-Boltzmann distribution of molecular hydrogen particles with a most probable energy of 0.026 eV, approximately 3 percent of particles have an energy of 0.282 eV or larger. The results of both of these calculations can be seen in Fig. 5.17.

We therefore add the contributions of these two methods of penetration to obtain a fueling efficiency of approximately 17 percent for wall-sourced particles in the W7-X edge. This value is approximately a factor of five less than the values of f_{lim} calculated by EMC3-EIRENE, shown in

Equation 5.1. We therefore scale the values of f_{lim} down by a factor of five to determine f_{wall}. This yields values of 0.15 and 0.17 for the Increased Iota configuration and the Standard configuration, respectively. These values of f_{wall} are also in improved agreement with previous values of wall-particle penetration in the literature [35, 37, 79]. Therefore the final form of the W7-X particle balance expressed in Equation 5.1 can also be written as:

$$\tau_p = \frac{N_{tot}}{-\frac{dN_{tot}}{dt} + f_{\text{lim}}\Phi_{lim} + \frac{1}{5}f_{\text{lim}}\Phi_{wall}} \tag{5.13}$$

This reduction makes sense in terms of edge geometry and the position of the wall relative to the confinement region. Since wall-sourced particles must, on average, travel a longer distance to the confinement region than those borne at the limiters, it is reasonable that f_{wall} is smaller than f_{lim}. These adjustments do not substantially change the final τ_p that is calculated. If $f_{\text{wall}} = f_{\text{lim}}$, rather than scaled down, the τ_p results would still lie within the other's error bars, but the absolute values of τ_p would decrease by a small factor.

5.7 Summary

In summary, we have followed a similar experimental procedure to that performed at HSX to study particle behavior at W7-X. Using both experimental measurements and EMC3-EIRENE numerical modeling, we have examined the particle confinement properties of both the Increased Iota (inward shifted 5/6 islands and 5/5 edge islands) and the Standard configurations (5/6 islands present near the LCFS, no 5/5 edge islands). Measurements of the decay of a peturbative helium puff yielded values of $\tau_{p,\text{He-I}}^*$ and $\tau_{p,\text{He-II}}^*$ a factor of 1.5 and 1.2 longer, respectively, in the Increased Iota configuration as compared to the Standard configuration. This indicates that edge helium particle transport has been changed by this difference in magnetic configuration, although it cannot quantify which portion of the changes are due to true particle confinement changes and which portion of the changes are due to possible helium recycling coefficient changes.

A complete hydrogen particle balance yielded particle confinement times a factor of 1.05 longer in the Increased Iota configuration relative to the Standard configuration, which lies within the error bars of both configurations. (These factors are for a heating power of 2.35 MW.) As a result, we conclude there is no meaningful difference in hydrogen particle confinement times between the two configurations. These results, along with measurements of $\tau_{p,H}^*$, yield a global hydrogen recycling coefficient R of approximately 1.1 in both configurations.

Finally, EMC3-EIRENE calculations of particle penetration indicated a value of fueling efficiency 7 percent reduced in the Increased Iota configuration relative to the Standard configuration, which is only just slightly out of the region of uncertainty in these calculations. Similar to the particle confinement time, we also conclude there is no meaningful difference in the fueling efficiency between the two configurations.

A more in-depth discussion of these results will be discussed in Chapter 6. In particular, the important physics results here will be compared to what was observed at HSX. Finally, we will attempt to put these results into context with other similar measurements in the literature and present our ideas for future work that could build on these studies and possibly yield more concrete findings in the W7-X divertor operational phases.

References

6. Stangeby, P. C. *The plasma boundary of magnetic fusion devices* 717 pp. ISBN: 978-0-7503-0559-4 (Institute of Physics Pub, Bristol ; Philadelphia, 2000).

35. Schmitz, O., Coenen, J., Frerichs, H., Kantor, M., Lehnen, M., Unterberg, B., Brezinsek, S., Clever, M., Evans, T., Finken, K., Jakubowski, M., Kraemer-Flecken, A., Phillips, V., Reiter, D., Samm, U., Spakman, G. & Telesca, G. Particle confinement control with resonant magnetic perturbations at TEXTOR. *Journal of Nuclear Materials* **390-391,** 330–334. ISSN: 00223115 (2009).

37. Maingi, R., Jackson, G. L., Wade, M. R., Mahdavi, M. A., Mioduszewski, P. K., Haas, G., Schaffer, M. J., Hogan, J. T. & Klepper, C. C. Control of wall particle inventory with divertor pumping on DIII-D. *Nuclear fusion* **36,** 245 (1996).

43. Knauer, J., Kornejew, P., Mora, H. T., Hirsch, M., Werner, A. & Wolf, R. *A New Dispersion Interferometer for the Stellarator Wendelstein 7-X* in *EPS Conference on Plasma Physics* (European Physical Society, 2016).

46. Krychowiak, M. *et al.* Overview of diagnostic performance and results for the first operation phase in Wendelstein 7-X (invited). *Review of Scientific Instruments* **87,** 11D304 (2016).

50. Colchin, R., Hillis, D., Maingi, R., Klepper, C. & Brooks, N. The filterscope. *Review of scientific instruments* **74,** 2068–2070. ISSN: 0034-6748 (2003).

51. Brooks, N. H., Colchin, R. J., Fehling, D. T., Hillis, D. L., Mu, Y. & Unterberg, E. Filterscopes: Spectral line monitors for long-pulse plasma devices. *Review of Scientific Instruments* **79,** 10F330. ISSN: 00346748 (2008).

52. Unterberg, E. A., Schmitz, O., Fehling, D. H., Stoschus, H., Klepper, C. C., Muñoz-Burgos, J. M., Van Wassenhove, G. & Hillis, D. L. HELIOS: A helium line-ratio spectral-monitoring

diagnostic used to generate high resolution profiles near the ion cyclotron resonant heating antenna on TEXTOR. *Review of Scientific Instruments* **83,** 10D722. ISSN: 00346748 (2012).

54. Stephey, L., Wurden, G. A., Schmitz, O., Frerichs, H., Effenberg, F., Biedermann, C., Harris, J., König, R., Kornejew, P., Krychowiak, M., Unterberg, E. A. & the W7-X Team. Spectroscopic imaging of limiter heat and particle fluxes and the resulting impurity sources during Wendelstein 7-X startup plasmas. *Review of Scientific Instruments* **87,** 11D606. ISSN: 0034-6748, 1089-7623 (Nov. 2016).

71. Bozhenkov, S. A., Effenberg, F., Feng, Y., Geiger, J., Hartmann, D. A., Hölbe, H., Pederson, T. S. & Wolf, R. *Limiter for the early operation phase of W7-X* in *EPS Conference on Plasma Physics* (2014).

72. Sunn Pedersen, T., Andreeva, T., Bosch, H.-S., Bozhenkov, S., Effenberg, F., Endler, M., Feng, Y., Gates, D., Geiger, J., Hartmann, D., Hölbe, H., Jakubowski, M., König, R., Laqua, H., Lazerson, S., Otte, M., Preynas, M., Schmitz, O., Stange, T., Turkin, Y. & the W7-X Team. Plans for the first plasma operation of Wendelstein 7-X. *Nuclear Fusion* **55,** 126001. ISSN: 0029-5515, 1741-4326 (1st Nov. 2015).

73. Effenberg, F., Feng, Y., Schmitz, O., Frerichs, H., Bozhenkov, S., Hölbe, H., König, R., Krychowiak, M., Sunn Pedersen, T., Reiter, D., Stephey, L. & Team, W.-X. Numerical investigation of plasma edge transport and limiter heat fluxes in Wendelstein 7-X startup plasmas with EMC3-Eirene. *Nuclear Fusion* **57,** 036021. ISSN: 0029-5515 (2017).

74. Brezinsek, S., Greenland, P. T., Mertens, P., Pospieszczyk, A., Reiter, D., Samm, U., Schweer, B. & Sergienko, G. On the measurement of molecular particle fluxes in fusion boundary plasmas. *Journal of nuclear materials* **313,** 967–971 (2003).

75. Szepesi, T., Alonso, A., Biedermann, C., Cseh, G., Dinklage, A., Jakubowski, M., Kocsis, G., König, R., Otte, M. & Sunn Pedersen, T. *Observations with the visible overview video diagnostic system during the first operational campaign of Wendelstein 7-X* in *EPS Conference on Plasma Physics* (European Physical Society, 2016).

76. Barbui, T., Krychowiak, M., König, R., Schmitz, O., Burgos, J. M., Schweer, B. & Terra, A. Feasibility of line-ratio spectroscopy on helium and neon as edge diagnostic tool for Wendelstein 7-X. *Review of Scientific Instruments* **87,** 11E554. ISSN: 0034-6748 (2016).

77. Ehrenberg, J., Coad, P., De Kock, L., Erents, S., Gondhalekar, A., Goodall, D., Hancock, J., Harbour, P., Jones, T. & McCracken, G. Hydrogen and helium recycling in tokamaks with carbon walls. *Journal of Nuclear Materials* **162,** 63–79. ISSN: 0022-3115 (1989).

78. Freeman, R. & Jones, E. M. *Atomic collision processes in plasma physics experiments* (UKAEA Research Group, 1974).

79. Majeski, R., Doerner, R., Gray, T., Kaita, R., Maingi, R., Mansfield, D., Spaleta, J., Soukhanovskii, V., Timberlake, J. & Zakharov, L. Enhanced energy confinement and performance in a low-recycling tokamak. *Physical review letters* **97,** 075002 (2006).

Chapter 6

Discussion and future work

This chapter is the final chapter of this thesis. It summarizes the important results contained within this work (primarily described in Chapters 4 and 5), discusses the physical mechanisms that govern these findings and puts this work in context, and outlines possible future work that has become apparent through this study.

6.1   Major results

1. The ability for a change in edge magnetic geometry to affect **the ionization source distribution** was the defining factor in whether global particle confinement changes were seen (at HSX) or not seen (at W7-X).

   (a) At HSX, where the **8/7 islands were able to create a private flux region which helped direct ionized particles immediately back to the wall**, the fueling efficiency was decreased by a factor of 1.24 and particle confinement time was increased by a factor of 1.32 as compared to the No-Edge-Islands configuration.

   (b) At W7-X, where the inward shift of the 5/6 island and the introduction of the 5/5 island into the edge **did not impact the ionization source distribution**, the fueling efficiencies and particle confinement times were relatively constant in the two configurations.

2. At both HSX and W7-X, the Edge-Islands configuration and the Increased Iota configuration exhibited longer decay times of $\tau^*_{p,He}$ by a factor of 1.6 in HSX and a factor of 1.5 and 1.2 in W7-X, which could stem from several factors which will be discussed below.

Each of these major conclusions is described in more detail in the three sections that follow.

6.2 Conclusion 1 - Edge topology and the ionization source distribution in HSX and W7-X

One of the key results from this work is that in HSX, the 8/7 magnetic island geometry reduces the penetration fraction of neutral particles into the confinement region (see Fig. 4.14). The key physics mechanism behind this result is the following. Particle flux exits the LCFS predominately through regions of high curvature. The majority of plasma is then carried through parallel transport to specific localized areas of the wall [21]. When some fraction of these particles recycle, they re-emerge as neutrals in what is effectively the private flux region of the X-point geometry created by the 8/7 island and its intersection with the HSX vacuum vessel (see Fig. 6.1). As a result, if these particles are ionized within this private flux region, they will be immediately directed back to the wall by outward parallel transport, and the cycle will continue. The 8/7 island geometry therefore helps prevent the recycling particles from ionizing within the confinement region and results in a decreased fueling efficiency as shown by EMC3-EIRENE calculations.

These findings are the result of EMC3-EIRENE simulations in both the Edge-Islands and the No-Edge-Islands configurations. By examining the magnetic topology (i.e. both the connection length and the Poincaré plots) of both configurations, the background plasma temperature, and the ionization source rate S_p (all of which are shown in Fig. 6.2), it is clear that the magnetic topology plays a role in reducing the number of ionizations that take place inside the confinement region in the Edge-Islands configuration. The locally increased temperatures near the 8/7 X-point result in an increased rate of ionizations, and the X-point geometry serves to direct the flow of ions along
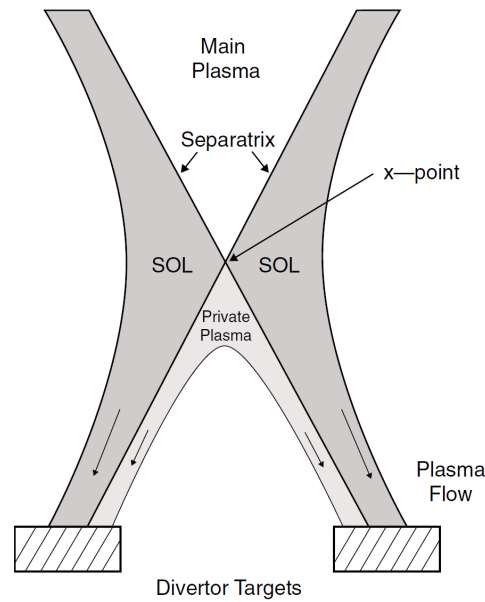
Figure 6.1 Figure demonstrating the X-point geometry in a tokamak. Note that behind the X-point is the private flux region, where particles that ionized are directed immediately back to the divertor target. Figure reproduced from [6] Figure 1.12.

the field lines back to the target. Together these phenomena reduce the penetration fraction of wall-sourced particles in the Edge-Islands configuration.

The magnetic topology, the background plasma temperature, and the ionization source rate S_p are shown in Fig. 6.2 for both HSX configurations. This figure is the same as Fig. 4.14. In Fig. 6.2(e) where islands are present, the source rate distribution can be shown peaking around the X-point of the 8/7 magnetic island. Conversely in Fig. 6.2(f), the source rate is much more diffuse and extends radially further into the confinement region. Divertors are designed to prevent this direct penetration of neutral particles [6], so perhaps it is not surprising that the more "divertor-like" Edge-Islands configuration exhibits positive neutral screening attributes and consequently improved hydrogen (and possibly helium) particle confinement times relative to its No-Edge-Islands counterpart.
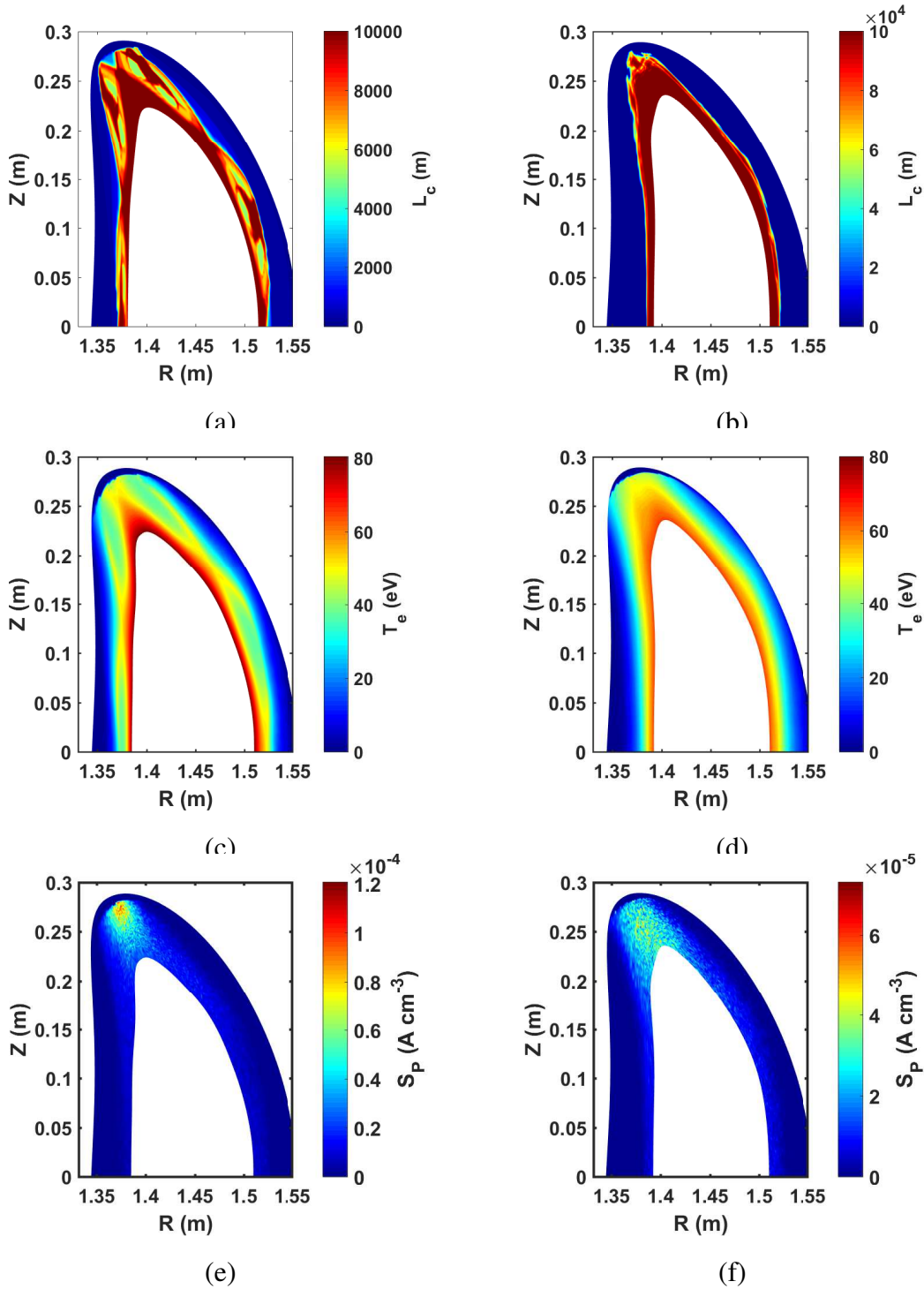
Figure 6.2 EMC3-EIRENE calculations for the Edge-Islands configuration (left column) and the No-Edge-Islands configuration (right column). (a) and (b) Plots of the magnetic connection length and Poincaré plots. (c) and (d) Plots of the self-consistently calculated plasma temperature, which highlights the island structure in (c). (e) and (f) Plots of the ionization source rate of hydrogen particles. In (e), the majority of the ionizations take place near the magnetic X-point. In (f), the ionization front is more diffuse and extends further into the confinement region. EMC3-EIRENE calculations courtesy A. Bader.

The effect of islands preventing inward flux of neutrals appears predominantly at the bean cross section and extends through some finite toroidal extent (and is most visible between a toroidal angle of 0 and 11 degrees). The EMC3-EIRENE S_p calculuations are shown in Fig. 6.3 for four toroidal cuts: 0, 11, 25, and 42 degrees. In this figure, the EMC3-EIRENE ionization source rate distribution is plotted for the Edge-Islands configuration on the left, and for the No-Edge-Islands configuration on the right. The data at different toroidal angles are plotted in order of ascending toroidal angle. The S_p data have been autoscaled and therefore differences in the peak ionization rate can be more easily observed.

This increased plasma temperature at the 8/7 island X-point is not only an EMC3-EIRENE prediction, but has also been experimentally measured by A. Akerson [27] using a 2-D movable Langmuir probe in the HSX edge. A 2-D temperature profile from the Edge-Islands configuration is shown in Fig. 6.4. Temperatures at the X-point are measured to be approximately 60 eV which is well above the minimum ionization potential for neutral hydrogen (~ 13 eV). Such profiles have not yet been measured for the No-Edge-Islands configuration and could constitute future work as will be discussed in the sections that follow.

This same argument can also offer an explanation for why we did not see substantial changes in the fueling efficiency or hydrogen particle confinement time at W7-X when the edge magnetic topology was changed (see Fig. 6.7). In the Standard configuration, the 5/6 island chain was located several cm inside the LCFS. At this location, EMC3-EIRENE modeling indicated that it would not play a major role in affecting the source distribution because a large part of the ionization took place radially outside the island location (see Fig. 6.6). In the Increased Iota configuration, the 5/6 island was moved further inward (still well away from the peak source region) and the 5/5 island was introduced to the W7-X edge in the far SOL (behind the limiter). Poincaré plots showing the magnetic topology in the two configurations are shown in Fig. 6.5. In this figure, the Standard
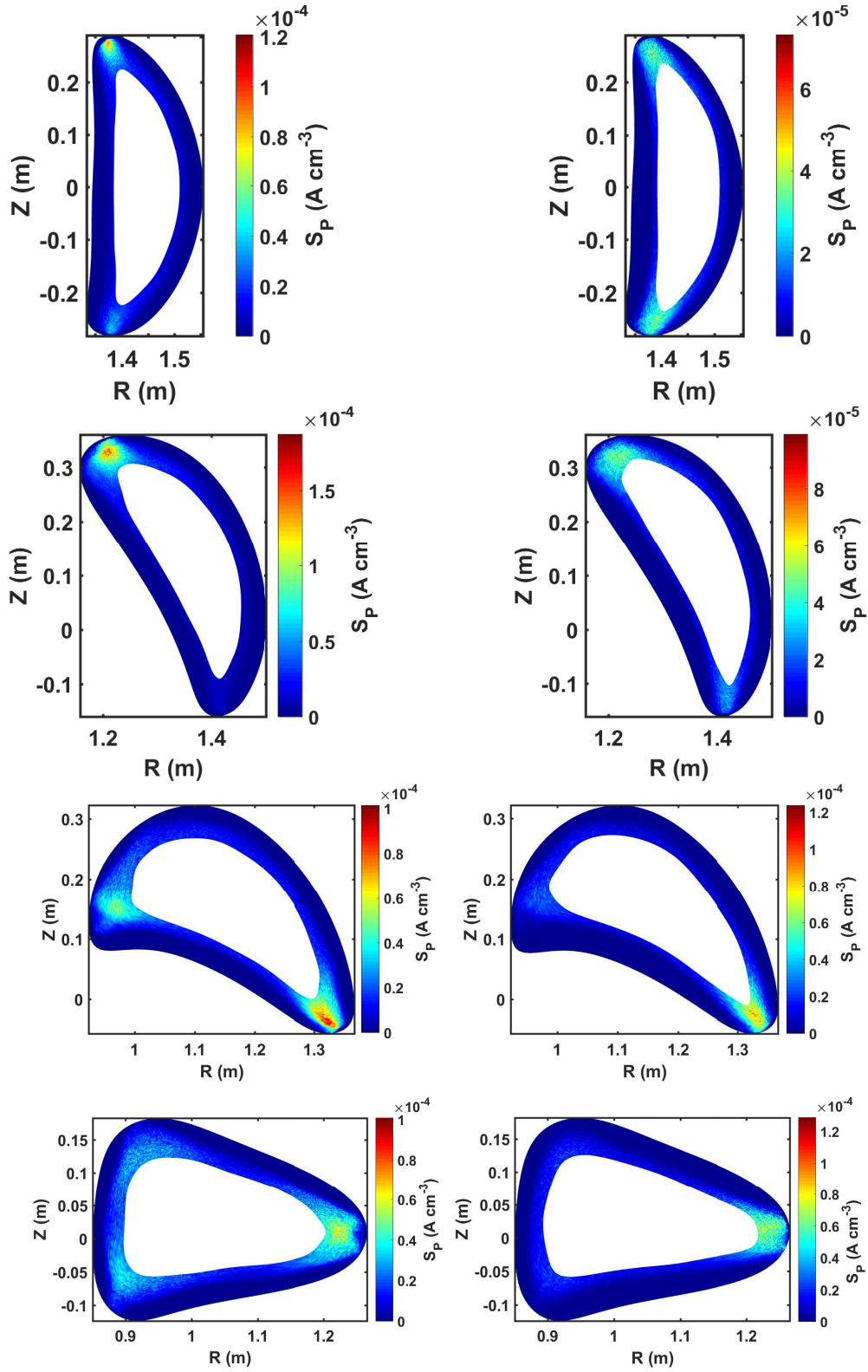
Figure 6.3 Figure demonstrating that the effect of the magnetic topology on the ionization source region exists at several toroidal angles in HSX. EMC3-EIRENE S_p data in the Edge-Islands configuration are shown on the left and data in the No-Edge-Islands configuration are shown on the right. The data at toroidal angles of 0 degrees, 11 degrees, 25 degrees, and 42 degrees are pictured in order from top to bottom. EMC3-EIRENE calculations courtesy of A. Bader.
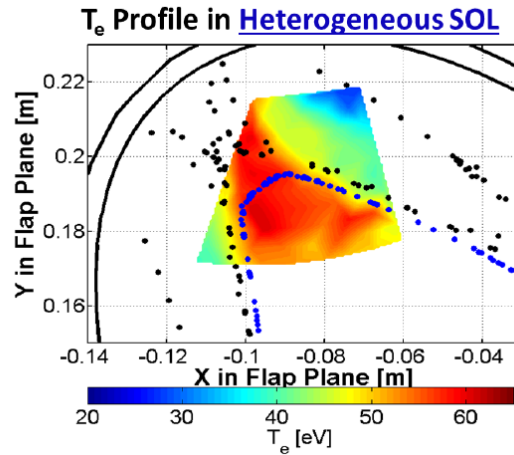
Figure 6.4 2-D measured plasma temperature in the Edge-Islands configuration. Note the peak temperatures in the confinement region and near the X-point of the 8/7 islands. Plot reproduced from A. Akerson thesis. [27]

configuration is shown on the top left and the Increased Iota configuration is shown on the top right.

This 5/5 island location in the relatively cold, far SOL is believed to be the reason why the changes in particle confinement and penetration were minor (if they were present at all). EMC3-EIRENE simulations indicate that in the Increased Iota configuration, the ionization rate peaks in close proximity to the LCFS, far away from both the 5/5 and the 5/6 island chains. This peaking can be seen in Fig. 6.7. We hypothesize that if the iota profile had been further increased to move the 5/5 islands to the near SOL and place them within a 1-2 cm of the LCFS, or if the iota profile had been decreased to move the 5/6 islands closer to the limiter, the changes in particle penetration and ionization might have been far more pronounced and more comparable to HSX. Such a "Decreased Iota" configuration is shown at the bottom right of Fig. 6.5 and was proposed for OP1.1 by O. Schmitz and F. Effenberg but was not ultimately deemed safe for W7-X in the first operational phase.
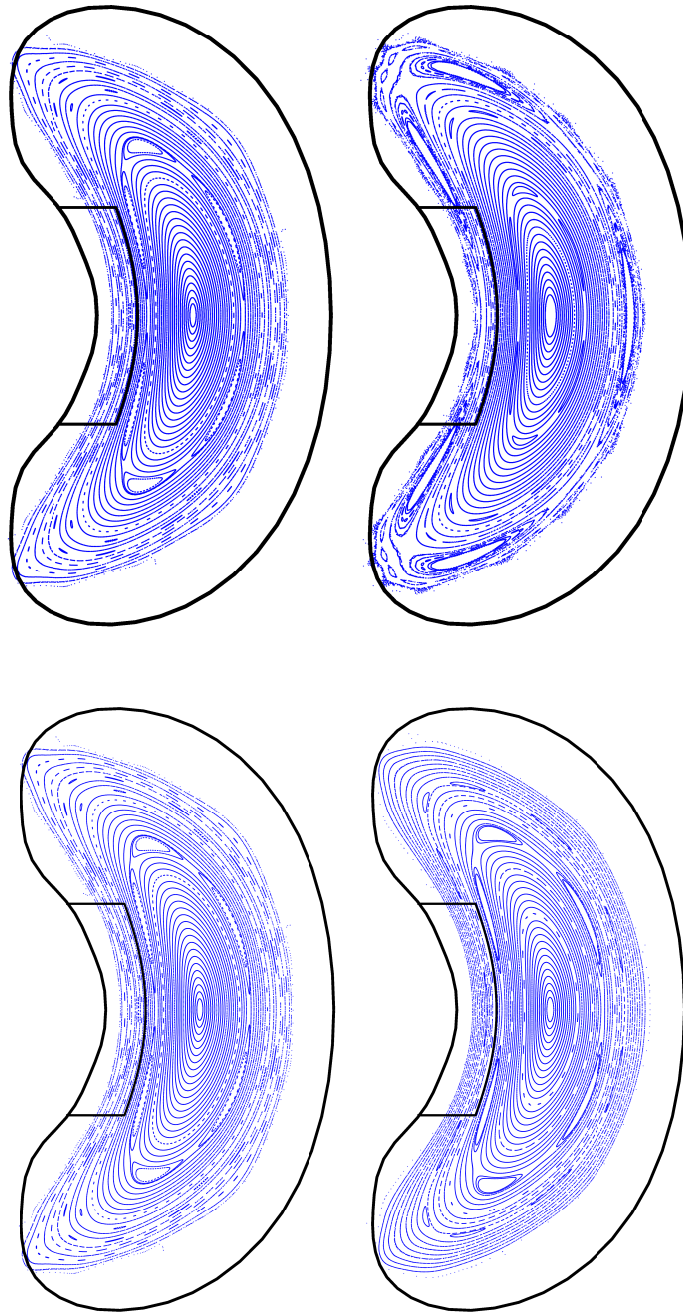
Figure 6.5 Poincaré plots for several W7-X magnetic configurations. The two top plots are the Standard configuration (left) and the Increased Iota configuration (right) examined in this work. The two bottom plots are the same Standard configuration (left) and a Decreased Iota configuration (right) which was never tested at W7-X. The Decreased Iota configuration might have resulted in reduced particle penetration and increased particle confinement as a result of the closer 5/6 island proximity to the limiter. Plots courtesy F. Effenberg.
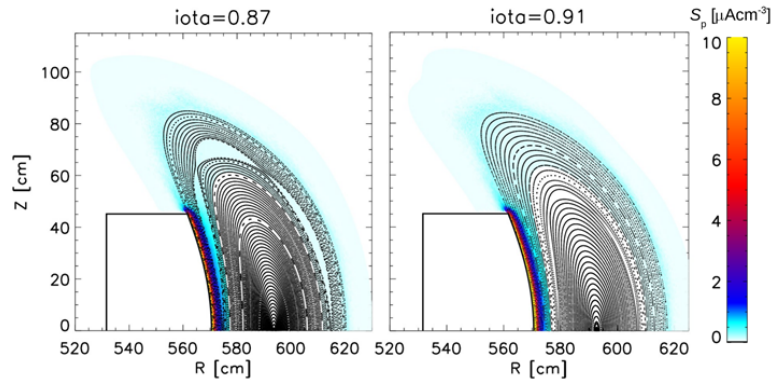
Figure 6.6 EMC3-EIRENE calculation of ionization source rate, S$_p$. Despite the change in edge structure, there were no substantial changes in the ionization source distribution. A flux surface averaged plot of these data are shown in Fig. 5.15 Plot courtesy F. Effenberg.
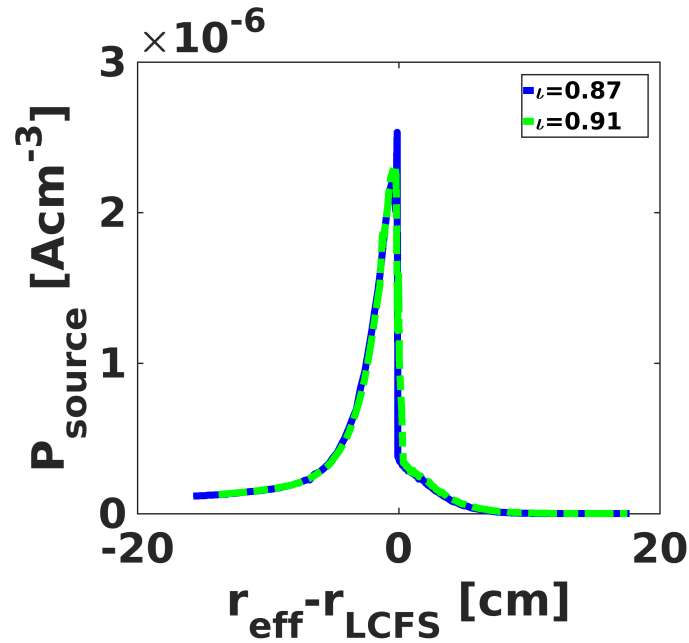
Figure 6.7 EMC3-EIRENE calculation of the flux surface averaged ionization source rate for helium in both the Standard configuration (blue solid line) and Increased Iota configuration (green dotted line). (The helium ionization profile is very similar to the hydrogen ionization profile). Plot courtesy F. Effenberg.

A summary of the four magnetic configurations explored in this work is shown in Fig. 6.8 in a general sense. This figure visualizes the relative relationship between the magnetic island chain(s) and the ionization domain in each configuration. The Edge-Islands and No-Edge-Islands configurations at HSX are pictured in (a) and (b), respectively. The Increased Iota configuration and the Standard configuration are pictured in (c) and (d), respectively. The relatively large differences in the location of the magnetic islands at HSX with respect to the ionized source distribution and the relatively minor differences observed at W7-X are consistent with the discussions of the experimental and numerical data above.

It should be noted that the cartoon in Fig. 6.8 is meant to provide only a gross overview of the type of experiments that were performed at HSX and W7-X. One should **not** take away from this figure that the ionization source rate profile was static, particularly at HSX. Rather, the location of the island itself directly influences the shape of the ionization source rate profile. These physical phenomena are all connected in a self-consistent manner.

At HSX, inserting and removing the 8/7 island chain into the main ionization region was accomplished, while at W7-X, the 5/6 island chain was not located close enough to the limiter in the Standard configuration (as seen in Fig. 5.14) and the 5/5 island chain was too far in the SOL to affect the ionization source distribution. However, the island divertor configuration at W7-X will be testing the concept explored at HSX and hence, the results from this initial study can be expanded upon in the upcoming island divertor campaign.

6.2.1 Different scalings of τ_p with $\bar{n}_e$ in the Edge-Islands and No-Edge-Islands configurations

Another result of this work was that at HSX, the hydrogen particle confinement time exhibited different scalings with density in the Edge-Islands configuration and in the No-Edge-Islands
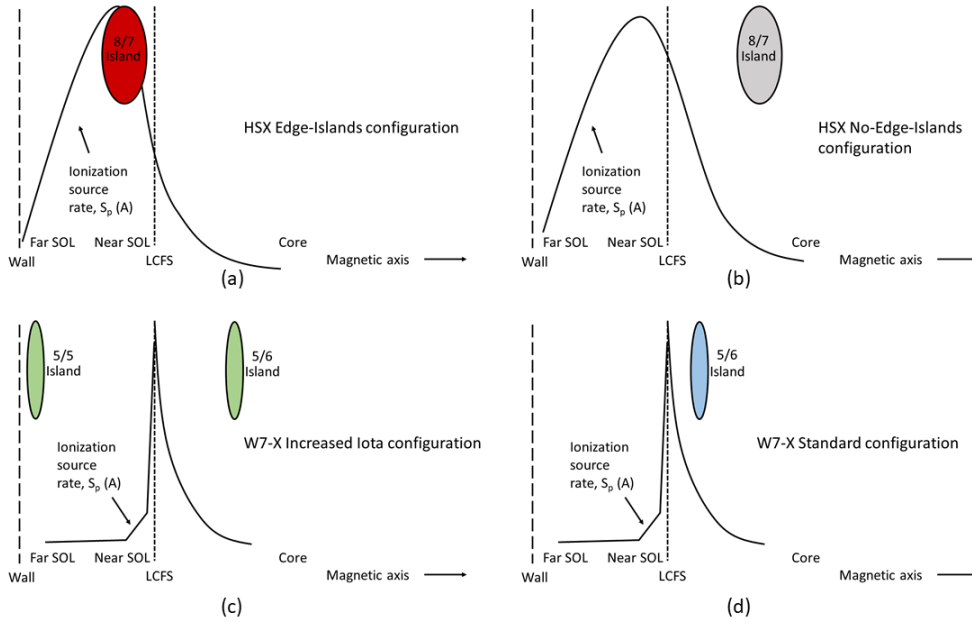
Figure 6.8 A summary of the relationship between the island position and the ionization source region for the four configurations that have been explored in this work. The magnetic island position(s) relative to the ionization domain have been noted for both the HSX configurations (a and b) and the W7-X configuration (c and d).

configuration. The trend in $\tau_{p,H}$ as a function of plasma density was positive in the Edge-Islands configuration, and the trend was negative in the No-Edge-Islands configuration.

Based on several studies in the literature, it appears as though there is a critical density at which the density trend turns over. This density is different for all three experiments which observed this phenomena (1×10^{19} m^{-3} at JET, 1.5×10^{20} m^{-3} at Alcator-A, and 4×10^{19} m^{-3} at TEXT) [80, 81, 82]. Data from all three of these experiments is shown in Fig. 6.9.

At TEXT, simultaneous measurements of the ratio of the limiter particle flux to the wall particle flux provide additional insight into the nature of this rollover. These measurements are shown in Fig. 6.10. They illustrate that when the ratio of the limiter to wall flux reaches a critical value, in this case ~ 1.5, the positive trend of particle confinement time with density transitions to a negative trend. They note that the trend of the limiter flux only (not shown in [82]) scales linearly
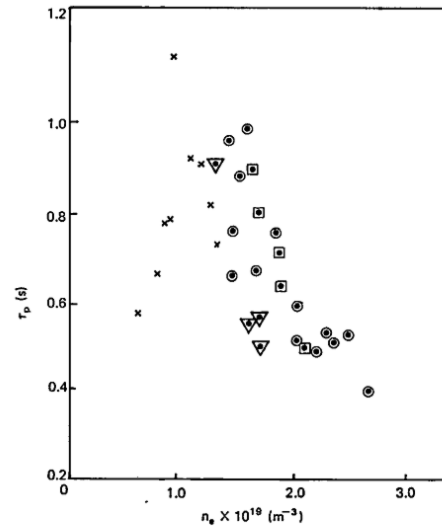
FIG.8. *Particle confinement time τ_p versus average plasma density.*

○	$B_\phi = 2.5$ T; I = 2.2 MA; b/a = 1.2
▽	$B_\phi = 1.6$ T; I = 2.2 MA; b/a = 1.6
□	$B_\phi = 2.0$ T; I = 2.7 MA; b/a = 1.6
×	$B_\phi = 2.5$ T; I = 1.5 MA; b/a = 1.3
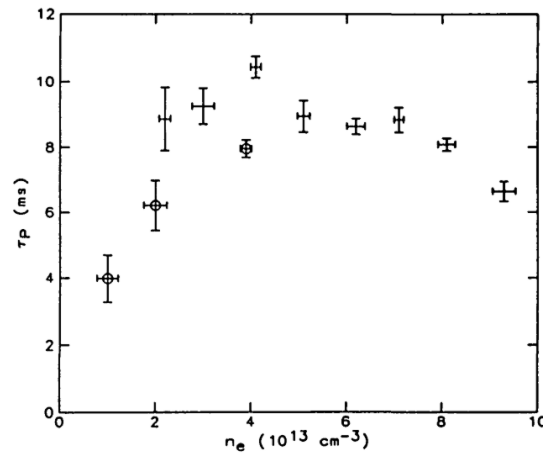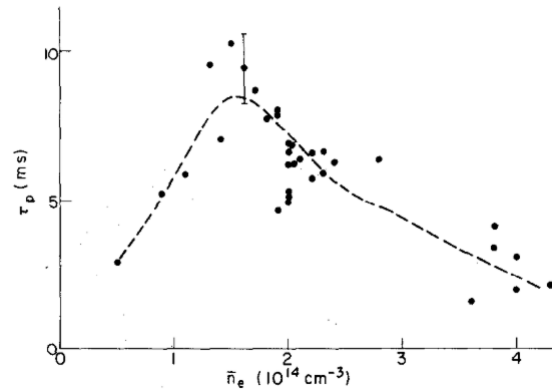
Figure 6.9 Measurements from JET (top), ALCATOR-A (middle), and TEXT (bottom) showing a rollover in the relationship between particle confinement time and plasma density. In all cases at lower density, the trend is positive. At some critical density (different at each experiment), the trend reverses and becomes negative. Plots reproduced from [80, 81, 82].

with density. It was concluded that when the undesirable wall contribution of particles becomes sizable, this favorable scaling disappears [82]. In general a positive scaling of confinement with plasma density is considered good because it means that at reactor-relevant densities (which will be high), it would be very advantageous if particle confinement increased with density, rather than decreased. This will result in a larger value of the fusion triple product, $\hat{n}\hat{T}\tau_E$ [83], where $\hat{n}$ and $\hat{T}$ are the peak densities and temperatures, respectively, which is necessary to achieve burning plasmas.

At HSX in the course of this work, no limiters were used, so we cannot compare the fraction of wall-sourced and limiter-sourced particles as was done at TEXT. (Limiters, though available, were not used because the limiter particle source rate could not be measured at the time these experiments were performed.) However, we can compare the product of the fueling efficiency and the wall-sourced particle flux for both the Edge-Islands configuration and the No-Edge-Islands configuration. The product of these two terms is plotted in Fig. 6.11. This plot can be compared to Fig. 4.11(d). Because the wall-sourced particle flux values are similar between the two configurations (as seen in Fig. 4.11(d)), the difference evident in Fig. 6.11 is largely the result of the difference in fueling efficiency. As a result, more wall-sourced particles ionize within the plasma in the No-Edge-Islands configuration. The bifurcation in the No-Edge-Islands data in Fig. 6.11 may be due to the fact that these data were obtained on two different days, but with otherwise comparable bulk plasma parameters and wall conditions. The reason for this apparent difference is not known at this time.

This reduction supports the argument that the reduced wall particle contribution in the Edge-Islands configuration contributes to the positive scaling in the value of $\tau_{p,H}$ with density, and likewise the increased wall particle contributed in the No-Edge-Islands configuration contributes to the negative scaling in the value of $\tau_{p,H}$ with density. Without a divertor or some additional magnetic
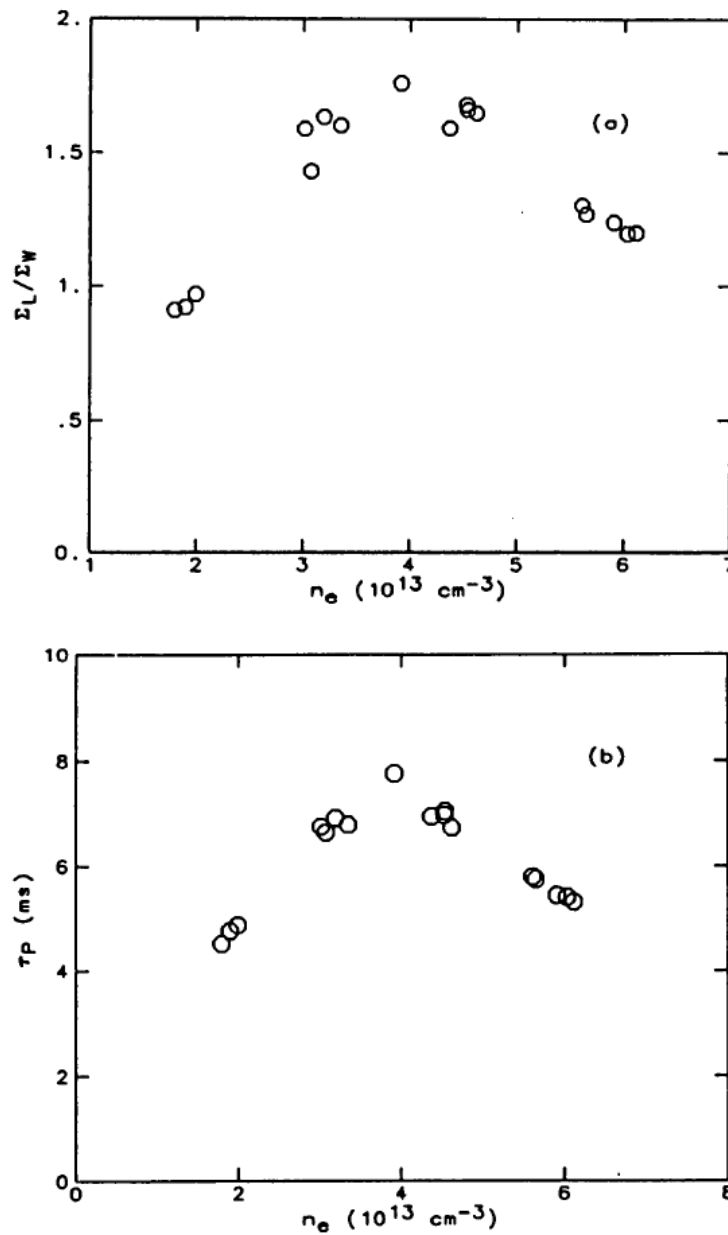
FIG. 13. Ratio of integrated particle source from recycling at limiter, Σ_L, to integrated particle source from recycling at wall, Σ_W, versus chord averaged electron density (a). For comparison, τ_p is also shown (b). For these discharges, $B_\varphi = 2.8$ T and $I_p = 300$ kA.

Figure 6.10 Measurements from the TEXT tokamak indicating the relationship betwween the ration of limiter to wall flux (top) and the trend in particle confinement as a function of plasma density (bottom) [82].
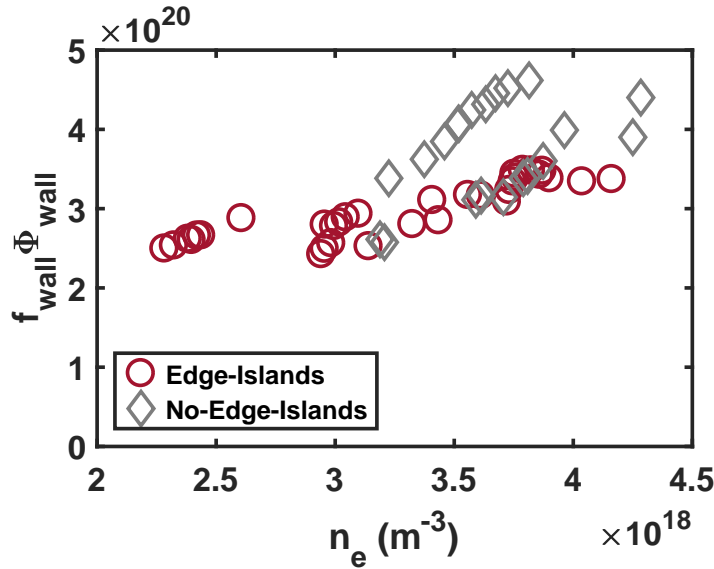
Figure 6.11 Plot of the product of the fueling efficiency f_{eff} and the wall particle flux Φ_{wall} for both the Edge-Islands (red circles) and No-Edge-Islands (gray diamonds) configurations in HSX as a function of plasma density. These data represent the total number of wall-sourced particles that are ionized within the confinement region in each configuration.

structure to prevent the wall-sourced neutrals from entering the plasma, the increased rates of un-controllable particle recycling tend to drive down the particle confinement time. Therefore in the Edge-Islands configuration, the edge "divertor-like" structure prevents the wall-recycled particles from entering the confinement region. However in the No-Edge-Islands configuration, no such magnetic structure is in place to prevent the wall-sourced particles from entering, and thus the particle confinement time degrades with increasing density.

6.3   Conclusion 2 - Increase in helium decay times at HSX and W7-X

Measurements of the decay of a perturbative helium puff at both HSX and W7-X yielded longer values of $\tau_{p,He}^*$ for the configuration with a magnetic island outside of the last closed flux surface for HSX and for W7-X in the far SOL. At HSX, the value of $\tau_{p,\text{He-II}}^*$ was increased by a factor of 1.6 in the Edge-Islands configuration relative to the No-Edge-Islands configuration. At W7-X, the

value of $\tau_{p,\text{He-II}}^*$ was increased by a factor of 1.2 in the Increased Iota configuration relative to the Standard configuration. Additionally at W7-X, the value of $\tau_{p,\text{He-I}}^*$ was increased by a factor of 1.5 in the Increased Iota configuration. These measurements indicate that the edge topology changes at both HSX and W7-X clearly resulted in a reduction of the effective helium confinement time $\tau_{p,He}^*$ when the magnetic islands were not present in the scrape-off layer region. This trend of $\tau_{p,He}^*$ agrees with the trend for $\tau_{p,H}$ at HSX. At W7-X, there was no change was measured in $\tau_{p,H}$ despite a significant increase in $\tau_{p,He}^*$ seen with the 5/5 island in the far SOL.

These seemingly contradictory results for W7-X can be understood by considering that helium has several properties which make the helium particle balance significantly different than the hydrogen balance. First, helium is not significantly absorbed by metal walls and is not co-deposited in hydro-carbon layers, unlike hydrogen. As a result, the recycling coefficient of He is close to 1 [77] and hence no He wall-pumping is possible (as at HSX, where R< 1 for hydrogen) and likewise no significant He wall-sourcing is expected (as at W7-X, where R>1 for hydrogen). It is also important to consider that the helium gas inlet at W7-X was located such that the He is **injected directly into the 5/5 island channel** for the Increased Iota configuration. The plasma parameters predicted by EMC3-EIRENE for inside of this island are $T_e \approx$ 4-6 eV and $n_e \approx 1.0\text{x}10^{18}$ m^{-3} which result in radial ionization scale length $\sim$ 5-10 cm for thermal He. This suggests that some amount of the helium injected could be trapped inside of the island. Some experimental evidence which supports this hypothesis are measurements of He-I and He-II emission (shown in Fig. 6.12) during and after ECRH turnoff, which suggest that a larger number of helium particles are confined in the Increased Iota configuration. (Helium recombination plays a dominant role below 10 eV where the helium ionization rate coefficient falls off steeply [78].) These findings suggest that the 5/5 island chain may contribute to this additional helium confinement. Future work with dedicated 2-D spectroscopy will be required to resolve island contributions to impurity ion confinement.
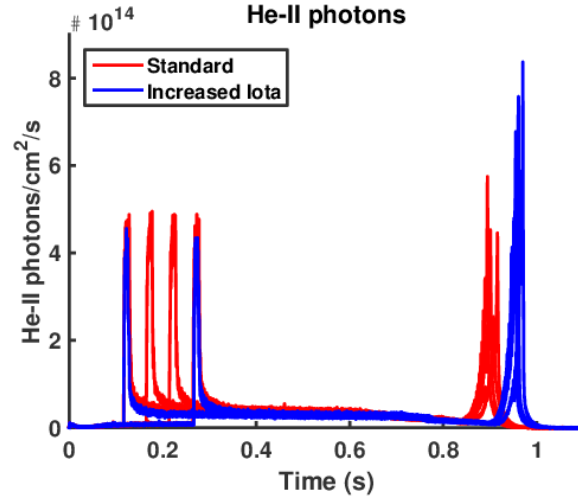
Figure 6.12 He-II signal from W7-X in the Standard (red) and Increased Iota (blue) configurations. ECRH turnoff is at 600 ms. After ECRH turnoff, the signal peaks from recombination generated emission.

Finally, in a simple impurity force balance, helium is treated as a trace impurity in terms of the friction and thermal force effects. This results in inward and outward transport coefficients which are coupled to different leading order transport mechanisms for the trace impurity as compared to the main species. The magnetic island in the plasma edge can alter parallel plasma profiles and hence change the ratio of the friction and thermal force, which might change the main ion and impurity ion transport. These profiles, however, were experimentally not accessible and modeling with EMC3-EIRENE for these helium cases is left for future work.

These helium confinement measurements can be compared to recent recent measurements at both TEXTOR and LHD [22, 23]. At these experiments, it was found that by using RMP fields, an island inserted into the edge region decreased the helium decay time (i.e. shorter values of $\tau_{p,He}^*$). It was shown that at both of these experiments, these edge manipulations enhanced the outward transport of helium particles. The driving mechanism was found to be due to an increase of the outward directed friction force relative to the inward directed thermal force due to collisionality gradients. However, it has to be noted that for these experiments the islands did not influence the

plasma wall interaction; rather, the islands were located inside of the confinement region in the helium ionized particle domain. In contrast, at W7-X and HSX in the configurations with larger $\tau^*_{p,He}$ (the Increased Iota and Edge-Islands configurations), the edge islands heavily influenced the plasma wall interaction and were present in the ionization source region (at HSX).

It should also be noted that depending on the magnitude of the RMP perturbation applied, TEX-TOR also saw operational regimes in which particle confinement could be increased as a result of "moderate" RMP fields [84]. This study concluded that the greatest confinement increases were present when the X-points of the islands were connected to the wall via magnetic flux bundles. The HSX Edge-Islands configuration also exhibits this same feature, so perhaps the particle confinement increases observed at both experiments is in fact related.

To summarize this section, islands have been shown to improve or degrade hydrogen and helium particle confinement depending on their placement and how their magnetic topology changes align with pumping geometry. Future work, including a large number of planned experiments during the W7-X divertor operational phases OP1.2 and OP2, will be necessary to better understand these relationships.

6.4 Possible contributions of core transport changes

As a final note, it is important to consider if the changes to the plasma core (i.e. through neo-classical transport) and that those changes, rather than edge structure induced changes, contributed to these measured differences τ^*_p and τ_p at both HSX and W7-X. In particular an increase of the effective ripple to adjust the edge structure (ϵ_{eff} on both W7-X and HSX was increased by a factor of 2) may have had deleterious effects on the core transport in the Increased Iota configuration and the No-Edge-Islands configuration. However, future work would be needed to resolve to what extent any possible changes in core transport affected the results in this study.

However, the HSX ions are in the Plateau regime [28] and the W7-X ions are in the Plateau/Pfirsch-Schületer regimes. In these regimes, there is no explicit transport dependence on the effective ripple. This means that the τ_p^* helium decay measurements (produced from ion emission) are unlikely to reflect any differences in core transport. With regard to the electrons, it was found that there were no major differences in core electron transport between the Standard configuration and Increased Iota configurations at W7-X due to the mitigating presence of a positive radial electric field [85, 86]. At HSX the role of the radial electric field [87, 88] in mitigating transport is still an open question.

Finally, EMC3-EIRENE simulations contain no information about potential core neoclassical transport changes that may have occurred as a result of the change in magnetic configuration (i.e. through the increased effective ripple). Despite this, EMC3-EIRENE results clearly show a difference in particle penetration as a result of changes in edge topology exclusively. These results demonstrate that the changes in the measured values of τ_p^* and τ_p stem primarily from changes in edge, rather than core, transport.

6.5   Future work motivated by this study

6.5.1   Possible future work at HSX

Our recommendations for future work at HSX are primarily focused on continuing to investigate the No-Edge-Islands configuration (i.e. 5 percent Well). To better understand this configuration, additional 2-D edge measurements like those peformed by A. Akerson [27] would provide more information about edge quantities in this configuration including temperature, density, electric field, and plasma flow. Plasma temperature is of particular interest because it governs the ionization physics which have been shown to impact overall particle confinement in the Edge-Islands configuration. These measurements would provide another opportunity for EMC3-EIRENE predictions

for the HSX edge to be validated, and for the edge of this configuration to be more thoroughly understood.

In addition to more carefully investigating the edge quantities in the No-Edge-Islands configuration, investigation of the neoclassical physics would also provide important information. Running DKES calculations for this configuration would be useful, as would making measurements of the radial electric field, to determine any possible increases in neoclassical transport as a result of increasing the effective ripple that may have contributed to differences in the values of τ_p^* and τ_p that were measured in this work. Additionally, turbulence measurements (like density and temperature fluctuations) and simulations (like GENE) could also add important information about any differences in turbulence-driven particle transport in these configurations. These studies could provide more information about the relative importance of edge physics, neoclassical physics, and turbulence physics that contribute to the global changes we observed in particle confinement between the Edge-Islands configuration and the No-Edge-Islands configuration.

The family of the Well-type configurations could also provide a fertile research area at HSX. A systematic study of configurations in the No-Edge-Islands configuration family, i.e. 0 percent, 2 percent, 6 percent, and 8 percent current in the auxiliary coils would be especially insightful as it allows the 8/7 island chain to be moved incrementally from outside the LCFS to just inside the LCFS to approximately the half-radius. This proposed series is pictured in Fig. 6.13. Such a study might yield more information about how specific island size and position affects global particle confinement properties in HSX and which edge magnetic geometry provides optimal edge and plasma performance. The effects may very well be nonlinear with island position. This series of experiments would be very relevant to island divertor operation in W7-X as they themselves seek to answer this same set of questions.
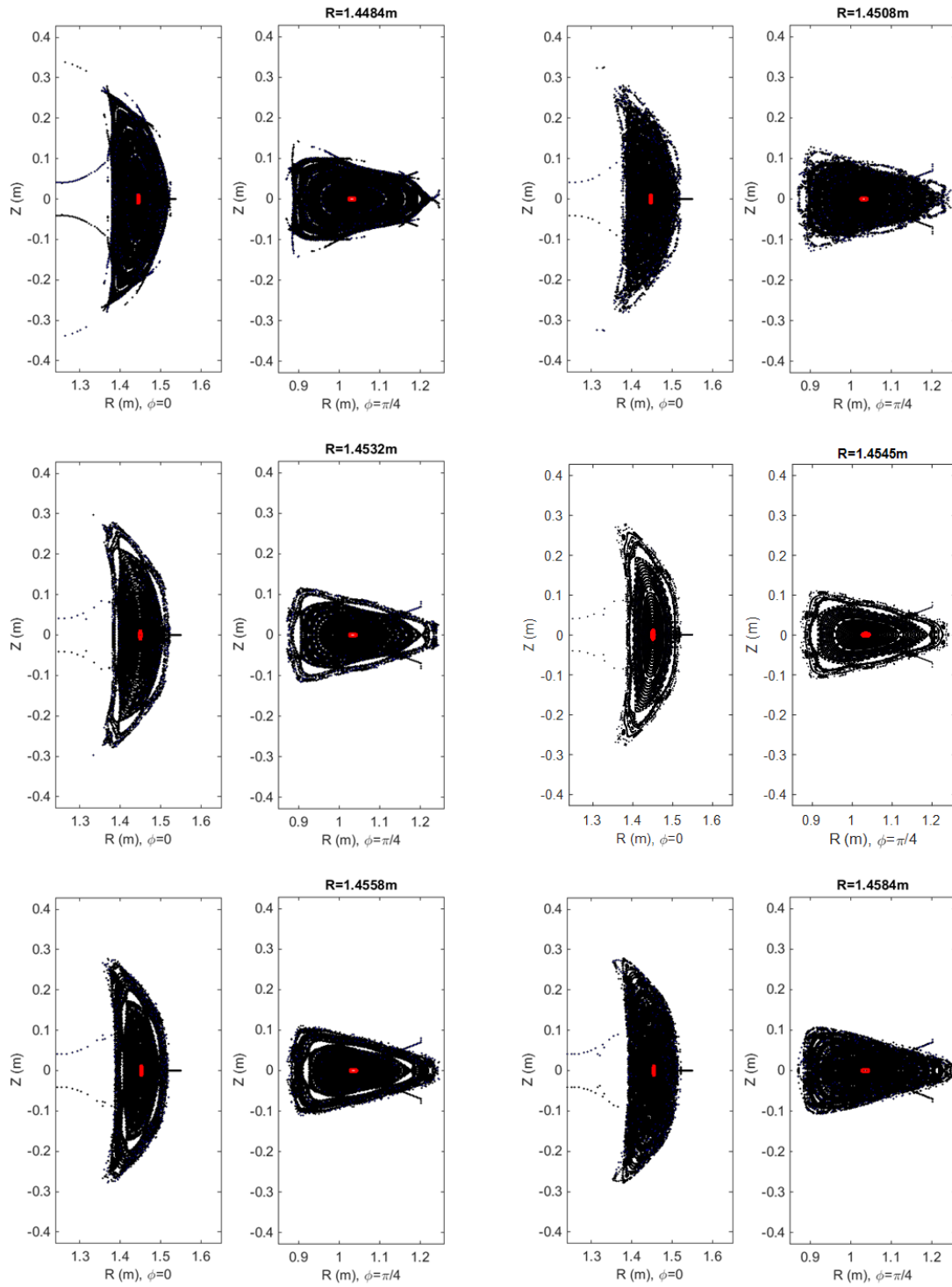
Figure 6.13 The No-Edge-Islands family of configurations in HSX (also called the Well configuration). From the top left and moving horizontally, 0 percent Well (QHS aka Edge-Islands), 2 percent Well, 4 percent Well, 5 percent Well, 6 percent well, and 8 percent Well. Poincaré plots courtesy of HSX magnetic database generated by K. Likin.

6.5.2 Possible future work at W7-X

Our recommendations for future work at W7-X during divertor operation are essentially to repeat the measurements made during the limiter phase (i.e. those in this work), perform additional measurements to provide more information about impurity species, notably helium, and perform hydrogen perturbative puff experiments in addition to helium perturbative puff experiments to provide more information about edge hydrogen transport.

To perform a full helium balance, several additional measurements will be required than were possible in the scope of this work. Using C-X or another diagnostic (possibly HEXOS or XICS), the fraction of helium ions in the core plasma could be determined. If these measurements are not available, performing a full collisional radiative model calculation to estimate the core helium fraction could also be an option. One of these techniques will be required to determine N_{tot} and perhaps $\frac{dN_{tot}}{dt}$ for helium. Additionally, EMC3-EIRENE helium penetration simulations will be necessary to determine the fueling efficiency (which may likely be different than hydrogen).

If a helium particle confinement time is obtained in addition to a measurement of $\tau_{p,\text{He-II}}^*$, then the measurements of $\tau_{p,\text{He-II}}^*$ can be disambiguated to separate the effects of the recycling coefficient and the true particle confinement information. This is a step beyond was what possible in this work. If both $\tau_{p,He}^*$ and $\tau_{p,He}$ were measured, the helium recycling coefficient R could also be calculated.

Furthermore, if a hydrogen and helium particle confinement time are both obtained, it will provide valuable information about how impurity transport is related to main ion transport in several different island topology configurations at W7-X. This would also extend well beyond what was possible in this work and would help to investigate if helium (and perhaps other impurities like carbon) can be preferentially exhausted from the plasma by a prudent choice of edge magnetic topology.

In addition to the perturbative helium puffs, we also strongly recommend perturbative hydrogen puff experiments at W7-X. This would provide a more robust way of measuring $\tau_{p,H}^*$ than fitting the interferometer density time trace. Measurements of $\tau_{p,H}^*$ made using H_α decay would provide much more information about the decay of neutral hydrogen specifically in the W7-X edge and could be compared to edge helium measurements to determine if the transport behavior is similar or different between these species.

Finally, we recommend that if density control at W7-X permits, a fine-scale density scan rather than a power scan will likely provide more meaningful results of the particle confinement behavior and its dependence on the plasma density. This would allow similar trends like those discovered at HSX to be investigated at W7-X.

6.6 Final summary

The edge magnetic structure in the HSX and W7-X stellarators is shown to have a significant impact on the particle fueling and exhaust of the plasma main species (hydrogen) as well as helium. In HSX, the 8/7 island chain located just outside the LCFS is shown to reduce particle penetration and increase global effective and true particle confinement times for both hydrogen and helium. In W7-X, the movement of the 5/6 island inwards and the introduction of the 5/6 into the edge does not result in any significant changes in hydrogen particle confinement times, likely because neither island chain was located in the ionization source region. However, an increase in the effective helium particle confinement time was observed when the 5/5 island was present in the edge, suggesting that the change in edge topology increased helium confinement to some degree. These findings suggest that for a helically optimized system like HSX, the plasma fueling from the recycling source as well as from active gas injection can be controlled by the magnetic island chain in the plasma edge - which is a basic requirement for a divertor system.

Hopefully this information will be informative to future studies at both HSX and W7-X. In particular, we hope that this information may help inform the types of experiments performed and the techniques chosen to evaluate the W7-X island divertor performance. Since the W7-X island divertor depends on the properties of the edge islands to not only guide the heat and particle flux safely to the divertor targets, but also to prevent these recycling particles from re-entering the confinement region, careful choice of island size and location will likely have a large impact on overall plasma performance.

References

6. Stangeby, P. C. *The plasma boundary of magnetic fusion devices* 717 pp. ISBN: 978-0-7503-0559-4 (Institute of Physics Pub, Bristol ; Philadelphia, 2000).

21. Akerson, A. R., Bader, A., Hegna, C. C., Schmitz, O., Stephey, L. A., Anderson, D. T., Anderson, F. S. B. & Likin, K. M. Three-dimensional scrape off layer transport in the helically symmetric experiment HSX. *Plasma Physics and Controlled Fusion* **58,** 084002. ISSN: 0741-3335, 1361-6587 (1st Aug. 2016).

22. Schmitz, O., Ida, K., Kobayashi, M., Bader, A., Brezinsek, S., Evans, T., Funaba, H., Goto, M., Mitarai, O. & Morisaki, T. Enhancement of helium exhaust by resonant magnetic perturbation fields at LHD and TEXTOR. *Nuclear Fusion* **56,** 106011. ISSN: 0029-5515 (2016).

23. Bader, A., Kobayashi, M., Schmitz, O., Akerson, A., Effenberg, F., Frerichs, H., Feng, Y., Hegna, C., Ida, K. & LHD Experimental Group. Modeling of helium transport and exhaust in the LHD edge. *Plasma Physics and Controlled Fusion* **58,** 124006. ISSN: 0741-3335 (2016).

27. Akerson, A. R. *Identification of the helical scrape-off layer structure and transport properties in the edge of HSX* ISBN: 1-369-05191-3 (The University of Wisconsin-Madison, 2016).

28. Gerhardt, S. P. *Measurements and modeling of the plasma response to electrode biasing in the hsx stellarator* PhD thesis (Univeristy of Wisconsin - Madison, 2004).

77. Ehrenberg, J., Coad, P., De Kock, L., Erents, S., Gondhalekar, A., Goodall, D., Hancock, J., Harbour, P., Jones, T. & McCracken, G. Hydrogen and helium recycling in tokamaks with carbon walls. *Journal of Nuclear Materials* **162,** 63–79. ISSN: 0022-3115 (1989).

78. Freeman, R. & Jones, E. M. *Atomic collision processes in plasma physics experiments* (UKAEA Research Group, 1974).

80. Cordey, J., Bartlett, D. & Bickerton, R. *Particle and energy confinement in Ohmically heated JET plasmas* (IAEA, International Atomic Energy Agency (IAEA), 1985).

81. Marmar, E. S. Recycling processes in tokamaks. *Journal of Nuclear Materials* **76,** 59–67 (1978).

82. Rowan, W. L., Klepper, C. C., Ritz, C. P., Bengtson, R. D., Gentle, K. W., Phillips, P. E., Rhodes, T. L., Richards, B. & Wootton, A. J. Global particle confinement in the Texas Experimental Tokamak. *Nuclear fusion* **27,** 1105 (1987).

83. Wesson, J. & Campbell, D. J. *Tokamaks* ISBN: 0-19-959223-3 (Oxford University Press, 2011).

84. Finken, K., Abdullaev, S., Jakubowski, M., de Bock, M., Bozhenkov, S., Busch, C., von Hellermann, M., Jaspers, R., Kikuchi, Y. & Krämer-Flecken, A. Improved confinement due to open ergodic field lines imposed by the dynamic ergodic divertor in TEXTOR. *Physical review letters* **98,** 065001 (2007).

85. Dinklage, A., Alonso, A., Baldzuhn, J., Beidler, C. D., Biedermann, C., Blackwell, B., Bozhenkov, S., Brakel, R., Buttenschön, B., Feng, Y., Fuchert, G., Geiger, J., Helander, P., Hirsch, M., Hoefel, U., Knauer, J., Kramer-Flecken, A., Landreman, M., Langenberg, A., Laqua, H. P., Maassberg, H., Pablant, N., Pasch, E., Rahbarnia, K., Rudischhauser, L., Smith, H., Stange, T., Stephey, L., Trimino-Mora, H., Turkin, Y., Velasco, J.-L., Wurden, G., Zhang, D., Andreeva, T., Beurskens, M., Blanco, E., Bosch, H.-S., Fornal, T., Grulke, O., Hartmann, D., Harris, J., Jakubowski, M., Klinger, T., Klose, S., Kocsis, G., Koenig, R., Kornejew, P., Krawczyk, N., Krychowiak, M., Kubkowska, M., Ksiazek, I., Lazerson, S., Liang, Y., Liu, S., Marchuk, O., Marsen, S., Marushchenko, N., Moncada, V., Moseev, D., Naujoks, D., Niemann, H., Otte, M., Pedersen, T., Pisano, F., Risse, K., Rummel, T., Schmitz, O., Satake, S., Schroeder, T., Szepesi, T., Thomsen, H., Traverso, P., Tsuchiya, H., Valson, P., Wang,

N., Wauters, T., Weir, G., Wolf, R., Yokoyama, M. & the W7-X Team. *Core confinement in Wendelstein 7-X limiter plasmas* in *EPS Conference on Plasma Physics* (2016).

86. Pablant, N., Bozhenkov, S., Dinklage, A., Fuchert, G., Landreman, M., Langenberg, A., Alonso, A., Beidler, C. D., Beurskens, M., Bitter, M., Burhenn, R., Delgado-Aparicio, L., Gates, D., Geiger, J., Hill, K. W., Hirsch, M., Hoefel, U., Knauer, J., Kramer-Flecken, A., Lazerson, S., Maassberg, H., Marchuk, O., Marushchenko, N., Mittelstaedt, J., Mikkelsen, D. R., Pasch, E., Satake, S., Smith, H., Svensson, J., Traverso, P., Turkin, Y., Valson, P., Velasco, J., Weir, G. M., Windisch, T., Wolf, R., Yokoyama, M. & Zhang, D. *Core radial electric field and transport in Wendelstein 7-X plasmas* in *APS Division of Plasma Physics Meeting* (2016).

87. Kumar, S., Talmadge, J., Dobbins, T., Anderson, F., Likin, K. & Anderson, D. Determination of radial electric field from Pfirsch-Schlueter flows in the HSX stellarator. *submitted to Nuclear Fusion, NF-101261.R1* (2016).

88. Briesemeister, A., Zhai, K., Anderson, D., Anderson, F. & Talmadge, J. Comparison of the flows and radial electric field in the HSX stellarator to neoclassical calculations. *Plasma Physics and Controlled Fusion* **55,** 014002. ISSN: 0741-3335 (2012).